UNIONE EUROPEA
Fondo Sociale Europeo

Ministero dell'Università e della Ricerca

PON RICERCA E INNOVAZIONE 2014 - 2020

REACT EU

UNIVERSITÀ DEGLI STUDI DI BRESCIA

UNIVERSITÀ
DEGLI STUDI
DI BRESCIA

DIPARTIMENTO DI INGEGNERIA DELL'INFORMAZIONE

DOTTORATO DI RICERCA IN TECHNOLOGY FOR HEALTH

CHIM-07

CICLO
XXXVII

SEQUESTRO DI CO_2 VOLTO ALLA REALIZZAZIONE DI NUOVI MATERIALI EDILI SOSTENIBILI A PARTIRE DA SOTTOPRODOTTI

GIADA BIAVA

Prof. ELZA BONTEMPI

Ing. ANTONIO PRINCIGALLO
(Direzione Tecnologie e Qualità Heidelberg Materials Italia Cementi S.p.A)

To my dad: my model, my angel
"I stumble but I don't give up"

SUMMARY

ABSTRACT

Il seguente progetto propone un nuovo metodo di valorizzazione della scoria di acciaieria come materiale sostitutivo del cemento tramite il processo di carbonatazione e l'aggiunta di additivi. Diverse scorie sono state campionate in Europa per studiare l'influenza della composizione chimica e mineralogica sulla carbonatazione e sull'idratazione del cemento. Tutti i campioni di scoria hanno mostrato elevate performance, catturando efficacemente notevoli quantità di CO_2, anche a condizioni di reazione diverse. I principali prodotti di carbonatazione identificati sono la calcite e il gel di silice. La tipologia di scoria ha giocato un ruolo fondamentale nell'influenzare il processo di carbonatazione. Tramite questo metodo il comportamento idraulico latente delle scorie si è trasformato in proprietà pozzolaniche. Tuttavia, la sola carbonatazione non è stata sufficiente per ottenere miglioramenti significativi nelle prestazioni del cemento composito. Per ottimizzare la formulazione, è stato necessario aggiungere degli acceleratori di idratazione, solfati, o entrambi, a seconda delle caratteristiche specifiche della scoria.

(English version)

This work proposed a new valorization method of steel slag as Supplementary Cementitious Material (SCM) by carbonation process and the addition of additives. Different steel slags were collected around Europe to study how the mineralogical and chemical composition influence the carbonation process and the cement hydration. All the slag samples demonstrated rapid carbonation reactions, effectively capturing significant amounts of CO_2, in different reaction conditions. The primary carbonation products identified were calcite and silica gel. The type of slag plays a key role in the studied process. The carbonation transforms the slags properties, shifting them from latent hydraulic behaviour to pozzolanic supplementary cementitious materials. However, carbonation alone was not enough to achieve notable improvements in composite cement performance. To optimize the formulation, it was necessary to add sulphate, hydration accelerators, or both, depending on the specific characteristics of the slag.

CHAPTER 1

STATE OF ART

The manuscript provides a comprehensive overview of the doctoral research, outlining the main objectives and the results of the project. It begins by introducing the research topic and clarifying the specific goals of the study. Following this, the materials and methods employed throughout the experimental work are detailed, including the laboratory procedures and techniques used to achieve the project's aims. The results section presents a thorough analysis, starting from the initial experimental setups and progressing to the application of steel slag in cement formulations, as well as its potential use in a high-performance carbonation reactor. Finally, the findings are summarized in the conclusion, highlighting both the benefits and limitations of the study, while also discussing the challenges and future directions for further research in this field.

It is important to underline that the project was cofounded by Heidelberg Materials Italia which also contributes to the pre-treatment of the samples and in structural analysis, and part of the work was developed at Heidelberg Materials, Germany. The research project co-financed by the European Union under the PON R&I 2014-2020 Programme, FSE REACT-EU resources, Action IV.5 “Doctorates on Green topics”.

1.1 Snapshot of CO_2 levels and CCUS techniques

The use of fossil fuels for industrial and home uses results in the production of huge amount of greenhouse gases (GHG) as CO_2, methane, nitrous oxide, chlorofluorocarbons and ozone, where CO_2 is the most important anthropogenic GHG because it is responsible for about two-thirds of the enhanced greenhouse effect [1]. In particular, the increasing concentration of CO_2 in atmosphere has the greatest impact on global warming, which causes more extreme weather and environmental disasters like floods, droughts and sea level rise [2]. It was estimated that global carbon dioxide concentration increases of 31.7% from 1958 to 2021 [3]. In 2023, CO_2 emissions have registered a new record about 37.4 Gigatonnes [4]. The main producers of CO_2 are refineries, coal and natural gas sources, cement and iron and steel plants and some data are collected in **Table 1**:

Table 1. Data about CO_2 emissions from industrial process [5]. The considered industries are coal, natural gas, refineries, cement and iron and steel industries

Source	Global CO_2 emissions (10^6 t CO_2/year)
Coal	14,200
Natural gas	6,320
Refineries	850
Cement industries	2,000
Iron and steel industries	1,000

The goal of Paris Agreement is to limit global warming under 2°C and after COP26 the limit is reduced to 1.5°C for year. To reach this aim, annual CO_2 emissions need to be reduced by 45% from 2010 levels by 2030 and achieve net zero emission by 2050 [5]. However, the global demand for energy is continuously increasing and estimated to be ascending by more than 28.6% by 2040. To reduce CO_2 emission, new energy sources as solar, wind and hydrogen energy can replace fossil sources but not in short time. Currently, one of more used technology is carbon capture, utilization and storage (CCUS). This technique includes ocean storage, forestation, oil and gas reservoirs, deep saline formations and mineral storage, as shown in **Figure 1** [6]. It is estimated that this technology can sequestrate more than 7 billion tons of CO_2 annually by 2050 [2].

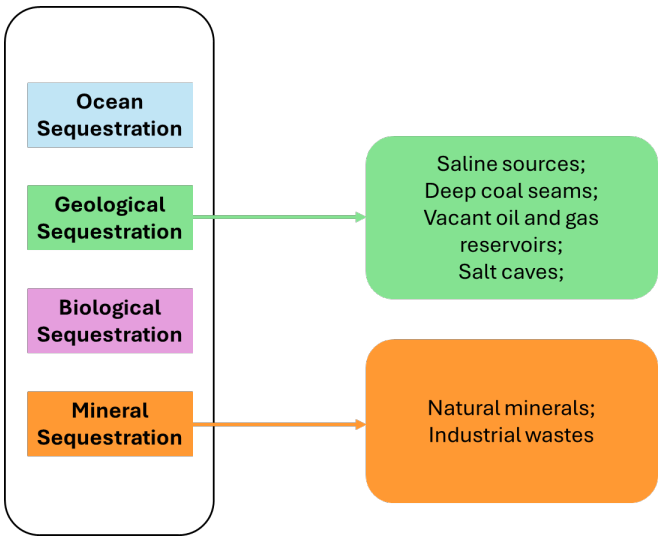

Figure 1. Classification of Carbon Capture, Utilization, and Storage (CCUS) methods based on the sequestration environment. The diagram illustrates four main types of sequestration: Ocean, Geological, Biological, and Mineral. This classification highlights the diversity of CCUS strategies for long-term carbon storage.

CO_2 mineral storage mimics the natural weathering process of rocks, in which CO_2 reacts with calcium or magnesium minerals to store the gas in stable and insoluble carbonates ($CaCO_3$/ $MgCO_3$), at a higher rate [7]. The starting materials available for the storage are natural minerals such as forsterite (Mg_2SiO_4), serpentine ($Mg_3Si_2O_5(OH)_4$), and industrial wastes as blast furnace slag, steel slag, cement waste etc. These materials are widely used in the world, so this technology has a certain potential industrial application [1]. Comparing these two classes of starting materials, industrial wastes are much more suitable for this process due to their higher reactivity, intrinsic alkalinity, richness in metal oxides (including calcium, magnesium, aluminium, iron and manganese oxide) and ready availability near industrial sites [6].

The potential advantages of accelerated carbonation of industrial alkaline solid wastes are several as:

- Great sequestration capacity due to the high availability of deposits at low material cost

- Fast reaction rate of carbonation process
- Prevention of available industrial alkaline solid waste from landfill
- Reduction of environmental impacts due to decreased leaching of heavy metal trace element (Pb, Ni, Cd)
- Reduction of energy consumption and costs because the carbonation is an exothermal reaction
- Cost-effective process because wastes don't have to be transported [8].

1.2 Steel slag characterization

The topic of this research is examined in depth in the Review "Accelerated Carbonation of Steel Slag and Their Valorisation in Cement Products: A Review", published 23rd of April 2024 in Spanish Journal of Soil Science [7]

As shown in **Table 1**, steel industries are one of the main CO_2 producers. Moreover, only in 2023 the global crude steel production is around 1.9 billion tons and, consequently, around 400 million tons of slag are produced every year in the world [9]. Steel slag possesses a complex chemical and physical makeup because they originate from the separation of impurities in the raw materials used in steelmaking, such as iron ore, coke, and other additives. Proper characterization of this material is essential to understand its potential uses and environmental impact.

The production affects the properties of this by-product and based on it, steel slags are categorized in Blast Furnace (BF), Basic Oxygen Furnace (BOF), Electric Arc Furnace (EAF), Ladle Furnace (LF) and Argon Decarburization Oxygen (AOD) slag. Blast furnace slag forms during the initial step, when iron ore is reduced in the blast furnace using coke and limestone; the non-metallic impurities combine with fluxes to form this molten slag, which is later separated from the pig iron. Moreover, a cooling process is applied, and it influences the amorphous content of this byproduct. Moving to the first refining stage, Electric Arc Furnace slag is generated in electric arc furnaces where scrap metal or direct reduced iron is melted using high-voltage electric arcs; the slag forms from fluxes added to remove impurities and protect the molten steel from oxidation. In the secondary refining stage, Argon Oxygen Decarburization slag is produced during the refining of stainless steel, where oxygen and inert gases are blown into the molten metal to reduce carbon content, resulting in the formation of slag rich in lime and other oxides. Similarly, Ladle Furnace slag arises during ladle refining, where additives like lime and dolomite are used to adjust the chemical composition and temperature of the steel; this step helps remove impurities like sulphur and phosphorus from the steel. Each of these slags plays a crucial role in refining steel and capturing unwanted elements, though they differ in composition and function depending on the specific phase of the production process [10,11]. In Lombardia, the Italian region where part of the slag comes from, 1.5 million ton of EAF slag and 460.000 ton of AOD and LF slag were produced in 2021 [12].

Steel slag is primarily composed of metallic oxides and silicates, with CaO (24-65%), also in the form of free-lime, MgO (3-20%), FeO/Fe_2O_3 (0-37%), SiO_2 (10-32%) and Al_2O_3 (3-20%) being the main components. The exact chemical composition can vary depending on the type of steel produced and the method used (e.g., basic oxygen furnace or electric arc furnace). Other elements, such as manganese, chromium and titanium, may be present in varying amounts. The high calcium oxide content makes the slag alkaline, which can affect its behaviour in various industrial and environmental applications. The chemical composition of different type of slag is

reported in the following **Table 2,** underlining the main differences due to type of the process they come from:

Table 2. Chemical composition of different steel slag, influenced by the production process [7]. The data are obtained from different works in literature by a summary of all the founded data.

Steel slag	**CaO**	**MgO**	**Al_2O_3**	**SiO_2**	**Fe_2O_3**	**TiO_2**	**MnO**	**Cr_2O_3**	**ref**
	[%wt]	[%wt]	[%wt]	[%wt]	[%wt]	[%wt]	[%wt]	[%wt]	
BF slag	28-51	4-11%	6-20	26-40	<2	<2	<1	<1	[13–21]
BOF slag	42-55	5-11	2-6	10-23	10-37	<2	0.7-5	<1	[14,21–29]
EAF slag	24-40	3-15	6-12	6-32	20-30	< 2	0.4-7	1-6	[22,23,30–33]
LF slag	38-65	3-20	2-20	12-30	0.7-7	<1	0.4-4	<1	[21,22,34–37]
AOD slag	34-60	2-10	1-12	24-32	0.5-12	<1	<1	<3	[22,38–40]

The cooling process influences the morphology of the slag and the crystallinity degree. Despite of BF slag, this by-product mainly contains Ca-phases as belite (Ca_2SiO_4), tricalcium silicate (Ca_3SiO_5), inert phases or RO phases which are a combination of Mg, Fe and Ca, and Fe-phases as wuestite (FeO) and brownmillerite (Ca_2FeAlO_5), especially for EAF slag [7]. The mineralogical composition of steel slag is reported in the following **Table 3**:

Table 3. Mineralogical composition of steel slag, influenced by the production process [7]. The data are obtained from different works in literature by a summary of all the founded data.

Steel slag	**Mineralogical phases**	**ref**
BF slag	Amorphous, SiO_2, $CaSO_4$	[13,15,20,38,40]
BOF slag	C_2S, C_3S, C_2AF, RO phase (FeO-MgO-CaO-FeO), MgO, *f*-CaO, $C_{12}A_7$, β- C_2S, FeO, γ- C_2S	[14,22,23,25,26,28,41,42]
EAF slag	γ-C_2S, β-C_2S, $Ca_7Mg(SiO_4)_4$, $Mg_2Si_2O_6$, $Ca_3Mg(SiO_4)_2$, $CaSiO_3$, MgO, $Ca_2Al_2SiO_7$, Fe_2O_3, $MgFe_2O_4$, FeO, Fe_3O_4, SiO_2, MnO-FeO	[22,23,31,41–43]
LF slag	C_2S, $CaO{\cdot}Al_2O_3{\cdot}2SiO_2$, CaS, Al_2O_3, $Ca_{12}Al_{14}O_{33}$ ($C_{12}A_7$), MgO, β-Ca_2SiO_4, γ-Ca_2SiO_4, $Ca_2Al_2SiO_7$	[22,34–37]
AOD slag	γ-C_2S, β- C_2S, $FeMg_2O_4$, $FeCr_2O_4$, C_3S, $Ca_{14}Mg_2(SiO_4)_8$, CaF_2, MgO, $Ca_3MgSi_2O_8$, $Ca_3Al_2O_6$, $MgSiO_3$, $MgCr_2O_4$, $Ca_3Fe_2(SiO_4)_3$	[22,38–41,43]

1.3 Carbonation concepts

Accelerated carbonation mimics the natural reactions of silicates weathering by contact with atmospheric conditions [44]. It is divided into 2 approaches: direct and indirect carbonation (**Figure 2**). Direct carbonation occurs in a single step, whereas indirect carbonation is composed of two phases, extraction of alkaline metals by solvent and carbonation. This work is focused on direct carbonation pathway.

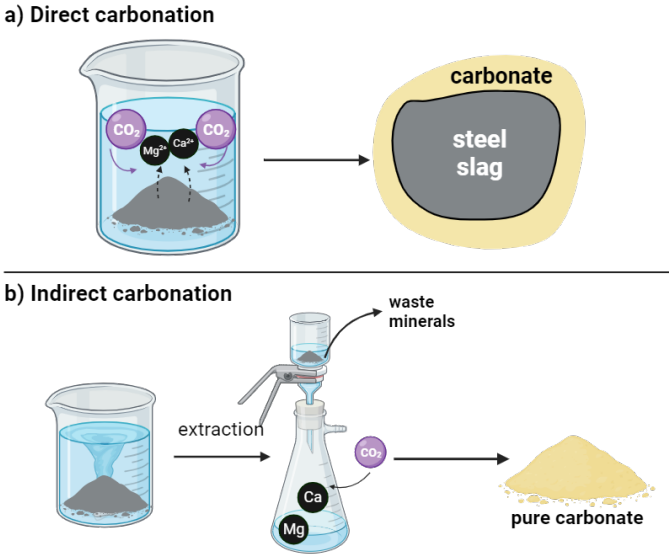

Figure 2. Schematic representation of mineral carbonation processes for CO_2 sequestration using steel slag. The upper panel illustrates the direct carbonation route, where CO_2 reacts with calcium (Ca^{2+}) and magnesium (Mg^{2+}) ions in steel slag to form stable carbonates on the slag surface. The lower panel shows the indirect carbonation approach, where Ca^{2+} and Mg^{2+} ions are first extracted into solution, then reacted with CO_2 to precipitate carbonate solids. (Image made by BioRender.com)

1.3.1 Direct gas-solid carbonation

This method was proposed by Lackner [45] and it represents the reaction between Ca and Mg oxides or hydroxides and CO_2 to form the corresponding carbonates, calcite ($CaCO_3$) and magnesite ($MgCO_3$) as shown in the **Equation 1**:

$$MO + CO_2 \rightarrow MCO_3 \quad (1)$$

where M is Mg or Ca ion. Additionally, some studies have demonstrated that other minerals as larnite (Ca_2SiO_4) or merwinite ($Ca_3Mg(SiO_4)_2$) react with CO_2 as follow [6,46] in the **Equation 2-3**:

$$Ca_2SiO_4 + 2CO_2 \rightarrow 2CaCO_3 + SiO_2 \quad (2)$$

$$Ca_3Mg(SiO_4)_2 + 4CO_2 \rightarrow 3CaCO_3 + MgCO_3 + 2SiO_2 \quad (3)$$

Under specific conditions, the direct gas solid reaction can sequestrate 10 g of CO_2/kg of slag at room temperature [47]. This result is influenced by the temperature: the sequestration enhances if the temperature reaches higher values to favour the interaction between the solid and the gas [7].

1.3.2 Direct wet carbonation

Direct carbonation pathway is more complex than gas-solid reaction because it a three phases system, gas-liquid-solid. In fact, gaseous CO_2 dissolves in the water and forms carbonic acid, which

can successively ionize into H^+, HCO_3^- and CO_3^{2-} promoting carbonation process. The general reaction is represented by **Equation 4**:

$$MO + CO_2 + H_2O \rightarrow MCO_3 + H_2O \quad (4)$$

where M is Ca and Mg ions.

At the beginning of the reaction, the pH has alkaline values, but the dissolution of the gas and the formation of carbonated products decrease the pH until neutral values (about 6.5/7) and the system reaching an equilibrium state [46]. As reported in **Section 1.2**, in steel slags Ca is not present as CaO but as C_3S and C_2S which may be hydrated forming calcium-silicate-hydrate (C-S-H) or calcium hydroxide or react directly with carbonate ion [6]. The three steps occur in a single step and are reported in **Equation 5-7:**

a) The leaching of minerals

$$Ca_2SiO_4\,(s) + 4H^+\,(aq) \rightarrow 2Ca^{2+}\,(aq) + 2H_2O\,(l) + SiO_2\,(s) \quad (5)$$

b) The dissolution of CO_2 followed by release of carbonate ions

$$CO_2\,(g) + H_2O\,(l) \rightarrow CO_3^{2-}\,(aq) + 2H^+\,(aq) \quad (6)$$

c) The nucleation and growth of mineral carbonates

$$Ca^{2+}\,(aq) + CO_3^{2-}\,(aq) \rightarrow CaCO_3\,(s) \quad (7)$$

1.3.3 Influence of reaction parameters

In direct-solid carbonation, temperature and pressure are key factors, with higher values of both enhancing the process by shifting the equilibrium toward CO_2 release. However, aqueous carbonation is influenced by multiple parameters, including temperature, particle size, reaction time, CO_2 pressure, pH, and the liquid-to-solid (L/S) ratio [46].

Reaction Temperature:

Temperature affects both the thermodynamic equilibrium and the reaction rate constants, as well as CO_2 dissolution during aqueous carbonation. An increase in temperature has a dual effect: while it enhances the solubility of cations such as Mg and Ca, it can hinder CO_2 dissolution. Identifying the "optimum temperature" is critical and depends on material properties and experimental conditions. Temperature ranges between 10°C and 40°C promotes cation release but lower CO_2 solubility, which is not a limiting factor in this case. At low temperatures, $CaCO_3$ forms on both the solid and liquid surfaces of the slag due to enhanced CO_2 dissolution, while at higher temperatures, it forms at the gas-liquid interface because of increased Ca ion dissolution in the liquid phase [7,46,48]. Some studies suggest the optimal temperature for steel slag carbonation is below 50–60°C [13,49].

Particle Size and pH:

The particle size significantly influences the carbonation process, as smaller particles provide a larger surface area, facilitating the reaction. Carbonation increases the specific surface area of steel slag, mainly due to enhanced surface porosity following calcium ion removal and the formation of irregular calcite layers. On other hand, pH plays a dynamic role in carbonation. In fact, at lower pH levels, the process promotes metal ion (cation) leaching, which are essential for the reaction. In contrast, a higher pH favours calcium carbonate precipitation [48].

CO_2 Pressure:

At a constant temperature, the amount of CO_2 dissolved in the liquid depends on the CO_2 partial pressure, in accordance with Henry's law. This applies when CO_2 dissolution is the rate-limiting step. In such cases, increasing pressure boosts both mineral dissolution and carbonate precipitation. However, when calcium extraction is the limiting factor, pressure has a less pronounced effect and may even cause negative impacts, such as unfavourably low pH or rapid calcite formation that creates a protective layer around the slag, reducing the contact area between the gas and the solid matrix [48]

Liquid to solid (L/S) ratio:

When the L/S ratio is below the optimal value, the steel slag doesn't dissolve effectively, reducing the interaction between CO_2 and calcium ions. At higher L/S ratios, CaO reacts with CO_2 to form $CaCO_3$, and CaO dissolves in water, forming $Ca(OH)_2$, which then precipitates as calcite. However, when the L/S ratio exceeds a critical value, excessive water can inhibit mass transfer or reduce calcium ion concentration [50].
From literature data [7], optimal results are generally obtained with particle sizes between 20–200 µm and carbonation times of around 1 hour, especially when the slag is ground to below 100 µm to increase reactivity. Additionally, an L/S ratio greater than 10 is recommended, though improvements level off beyond an L/S of 15. Higher CO_2 partial pressures also enhance CO_2 sequestration, particularly at lower gas concentrations due to increased solubility through pressurization.

As described in this part, the carbonation reactions are influenced by many parameters that affect in different ways. The optimization of them is required to obtain high performance in terms of CO_2 sequestration. Moreover, this process is suitable for both minerals and industrial wastes because of their alkalinity and presence of Ca and Mg as mainly ions. As described in the **Section 1.2**, steel slags have high content of Ca and Mg and different studies have demonstrated their suitability for this process [6,44,51]. Additionally steel slags present a similar mineralogical composition of cement, and they are a proper candidate as Supplementary Cementitious Material, favouring the circularity of the process.

1.4 Carbonation of steel slag: a valorization method for application in the cement industry

The cement industry is a significant contributor to both energy consumption and greenhouse gas (GHG) emissions, including carbon dioxide (CO_2) as reported in **Table 1.** This sector accounts for 7.4% of global CO_2 emissions, as the production of 1 kg of cement results in the release of 0.5 to 0.7 kg of CO_2 [19,52]. To mitigate CO_2 emissions from concrete products, the cement industry has adopted various strategies, such as incorporating Supplementary Cementitious Materials (SCMs) to partially replace clinker, the primary ingredient in Portland cement, or cement itself during the concrete production process. SCMs can include by-products like fly ash, steel slag, and cement waste [19]. Steel slags contain mineral phases like those found in Portland cement clinker, such as C_3S, C_2S, and C_2F. This makes steel slag a promising candidate for use as a Supplementary Cementitious Material (SCM) or as an additive in blended cements. Utilizing steel slag is both an environmentally friendly and efficient approach to reducing CO_2 emissions while also promoting slag recycling. However, the use of steel slag in the construction industry presents several

challenges due to various factors. One major issue is the high variability in slag composition, which limits the practical experience in this field [53]. Additionally, concerns related to durability, mechanical stability, and the potential release of heavy metals into the environment hinder the widespread and rapid adoption of these materials [54]. Consequently, numerous studies are being conducted to identify the best methods for optimizing the performance of steel slag as a by-product. In fact, the use of steel slag may affect negatively the composite cement performance. Steel slag exhibits limited reactivity due to the low percentage of C_3S, the delayed hydration of C_2S and the amorphous phase, which only becomes significant after about seven days. Furthermore, C_2F contains high levels of iron, further reducing its reactivity [54,55]. The presence of heavy metals in steel slag, such as Cu, Ni, Pb, and Cr, can inhibit the early hydration of C_3S from Portland cement clinker, and pose potential environmental risks due to metal leaching [56,57]. As demonstrated in multiple studies, steel slags contain free CaO and MgO, which can lead to volume instability in Portland clinker when used directly in cement production. One potential solution for valorising steel slag as an SCM is through carbonation. In fact, the direct wet carbonation promotes the formation not only of carbonated products but also Si-products as SiO_2 and C-S-H (calcium silicate hydrate) which enhance the pozzolanic character of this by-product, and, consequently, the compressive strength [58–60]. One of the most notable findings is the rapid reaction kinetics associated with this (alumina)-silica gel, if in slags alumina reacts as in the cement matrix. It has been demonstrated that nearly 50% of the reactive gel engages in pozzolanic reactions within just the first 24 hours of hydration, leading to early strength development and matrix densification [60]. Such behaviour is comparable to that observed in traditional SCMs like siliceous fly ash, but with potentially even faster activation. Moreover, carbonation conditions play a key role in the reactivity of the resulting materials. For example, carbonation processes conducted in sulphate-rich environments tend to produce gels with higher surface areas, thereby accelerating pozzolanic reactivity. Similarly, the presence of alkalis during carbonation can influence the morphology and hydration behaviour of the carbonation products, pointing to the need for careful control of process parameters [61]. The carbonation also improves the volumetric stability of steel slag by consuming free Mg and Ca oxide. While there are numerous studies on carbonation curing of steel slag in concrete blocks, few examples explore the use of carbonated steel slag as SCMs [58,62]. Initial findings from existing research are promising, although studies are still ongoing. Chen et al. [63] demonstrated that cement containing 10% carbonated BOF slag exhibits greater compressive strength compared to uncarbonated slag after 3 days. Additionally, carbonated BOF slag has shown a significant improvement in hydration activity, with increases of 97% at 3 days and 16% at 28 days [64]. This improvement in mechanical properties is largely attributed to the presence of limestone and hydrated products. The formation of $CaCO_3$ densifies the microstructure of steel slag, reduces pore size, and enhances hydration activity, providing a more favourable surface for the growth and nucleation of hydration products [57,65]. Research by Peng et al. [62] highlights the positive impact of carbonation on increasing compressive strength. In fact, mortar mixtures containing 15% and 30% carbonated slag demonstrate higher compressive strength compared to those containing uncarbonated slag [62]. In fact, the compressive strength of carbonated slag-based cement can be influenced by factors such as the percentage of cement replaced, the microstructure, mineral composition, and the degree of carbonation (where higher carbonation is associated with lower C_2S and C_3S content). Therefore, multiple variables must be considered to optimize the use of steel slag in cement applications.

CHAPTER 2

AIM OF THE PROJECT

The objective of this doctoral research is to investigate the potential for establishing an industrial symbiosis between the steel and cement sectors, with the dual aim of reducing CO_2 emissions and promoting circular economy strategies. The core hypothesis of the work is that steel slags, a by-product of steel manufacturing, can be effectively used both as a CO_2 sink through accelerated carbonation and once carbonated, as a supplementary cementitious material (SCM) in cement production.

The research was structured in two main phases. In the first phase, the CO_2 sequestration capacity of various steel slags was evaluated under different carbonation conditions. The goal was to understand how chemical and mineralogical composition, combined with process parameters such as liquid-to-solid ratio, stirring speed, and carbonation pressure (ambient vs. high pressure), influence the efficiency of the reaction. This phase aimed to identify the optimal conditions for maximizing CO_2 uptake while ensuring chemical stability of the resulting material.

The second phase focused on assessing the potential of the carbonated slags as SCMs. Given their composition and reactivity, these materials, if properly treated, could partially replace Portland cement in concrete formulations, thereby reducing clinker content and the overall carbon footprint of cement production. The study examined the mechanical and hydration performance of cement pastes and mortars incorporating carbonated slags, also considering the role of additional components such as calcium sulphate and hydration accelerators in improving early-age and long-term performance.

The overall ambition of the project is to propose a technically and environmentally viable pathway for integrating steel production residues into the cement industry. This approach supports broader decarbonization goals, minimizes industrial waste, and promotes more efficient resource utilization, ultimately contributing to the development of more sustainable construction materials.

The subsequent structure of the thesis is as follows:

- **Chapter 3 – Materials and Methods**: Details the origin and preparation of slag samples, the experimental carbonation setups, and the methodologies used for chemical, mineralogical, and mechanical characterization.
- **Chapter 4 – Results and Discussion**: Presents the results obtained by testing different slags under various carbonation conditions and evaluates their preliminary performance as SCMs in cement systems. This chapter also includes a discussion of the influence of mix design variables on the overall behaviour of the blended cement.

- **Chapter 5 – Conclusions**: Summarizes the key outcomes of the study, discusses the implications for industrial application, and proposes directions for future research.
- **Appendix**: Contains supporting information, data tables, and methodological details not included in the main text.

During the development of the thesis, several scientific articles were published. These are listed below, and specific paragraphs of the thesis refer to them directly to support or contextualize experimental results and interpretations.

- "Accelerated Direct Carbonation of Steel Slag and Cement Kiln Dust: An Industrial Symbiosis Strategy Applied in the Bergamo-Brescia Area", published on 29th of May 2023 in section "Materials" in the journal MDPI [66]
- "Accelerated Carbonation of Steel Slag and Their Valorisation in Cement Products: A Review", published 23rd of April 2024 in Spanish Journal of Soil Science [7]
- "Evaluation of steel slags in CO_2 sequestration and as Supplementary Cementitious Material", submitted to Construction and Building Materials on 17th of November 2024.

CHAPTER 3

MATERIALS AND METHOD

As explained in the "State of Art", this project has involved different partners, and the work was done in three different laboratories. For this reason, different instruments were used. In this Chapter, all the procedures and instruments were reported for XRD, XRF, FT-IR and SEM and for each technique it is specified the section where it was used. Despite of different approaches, the results and conclusions are not influenced. Moreover, to quantify CO_2 uptake TGA technique is used frequently because it quantifies the total amount of CO_2 sequestered by analysis of $CaCO_3$ or other carbonated product decomposition [67]. On the other hand, QXRD is employed to identify and quantify crystalline phases within a sample. By detecting the formation of calcium carbonate phases like calcite, QXRD can indirectly assess the extent of carbonation and, consequently, the amount of CO2 sequestered. This method is useful for investigating how the material changes after the carbonation process. However, it does not consider amorphous calcite content [68].

3.1 Starting Industrial By-products

This work focusing mainly on steel slags collected from different plants around Europe. The samples include Argon Oxygen Decarburization (AOD), Ladle Furnace (LF), Electric Arc Furnace (EAF) and Blast Furnace (BF) slag. Moreover, other 2 samples were collected in **Section 4.5** and they are called Slag8 and Slag9.

Furthermore, a cement waste was collected to test its suitability in direct carbonation. Cement Kiln Dust (CKD) is a fine-grained alkali-rich dust, and it comes from air pollution control devices during the cement clinker production. It is composed mainly of calcined raw feed, fuel combustion ashes, clinker dust, alkali components and other traces elements. Its chemical composition is influenced by many factors as the type of fuel used, the composition of raw material and the production process [69,70]. As reported in **Table 5**, the main mineralogical phases is calcite caused by the collection of calcite dust during the grinding process of calcite as raw material in the production of cement.

The steel slags used in this study were collected from multiple sampling campaigns conducted at different times. The first sampling provided the material for preliminary tests aimed at evaluating the feasibility of carbonation using various types of slag. These initial experiments yielded promising results, highlighting the potential of certain slags for effective CO_2 sequestration. The chemical composition, detected by X-Rays Fluorescence analysis, and mineralogical composition, quantified by QXRD analysis, are reported in **Table 4** and **Table 5**. In EAF3 and EAF2, the silica was used in the grinding process to test a different grinding approach.

Table 4. Chemical composition of various steel slags (LOQ refers to the Limit of Quantification). The Loss on Ignition (LOI) is calculated as weight loss, with the positive values attributed to the potential oxidation of iron. Data reported in [66]

	AOD1 [%wt]	**LF2** [%wt]	**EAF1** [%wt]	**EAF2** [%wt]	**EAF3 + SiO_2** [%wt]	**CKD** [%wt]
LOI	(+0.7)	5.7	(+3.3)	(+3.0)	1.1	29.9
SiO_2	23	17.4	10.9	12.4	27	12.9
Al_2O_3	10.8	10.4	6.7	7.9	2.2	2.5
Fe_2O_3	5.2	12.8	38	44	30	0.2
CaO	49	36	30	23	25	45
MgO	8.5	11.6	6.0	6.2	6.2	0.5
SO_3	0.2	1.4	0.3	0.4	0.2	4.9
K_2O	< LOQ	0.5	< LOQ	< LOQ	0.4	1.0
Na_2O	0.8	0.3	< LOQ	0.1	0.3	2.7
TiO_2	0.3	1.2	0.2	0.6	0.2	< LOQ
P_2O_5	< LOQ	< LOQ	0.3	0.3	0.3	< LOQ
Mn_2O_3	1.0	1.6	7.0	7.0	5.9	< LOQ

Table 5. Mineralogical composition of steel slag (first sampling) by XRD quantification. The quantification method used is Rietveld by internal standard. The estimated error of QXRD is less than 5% if the concentration of the phase is major than 10%; it is higher if the concentration is less than 5%. The data are reported in [66]

	AOD_1 [%wt]	**LF_2** [%wt]	**EAF_1** [%wt]	**EAF_2** [%wt]	**EAF_2 + SiO2** [%wt]	**EAF_3 + SiO2** [%wt]	**CKD** [%wt]
Albite	-	-	-	-	-	-	< 1
Amorphous	49.0	31.4	41.8	52.0	71.1	80.4	6.9
Aragonite	<1	< 1	< 1	-	-	-	-
Bredigite	2.2	-	-	-	-	-	-
Browmillerite	-	-	7.4	-	-	-	-
Brucite	-	< 1	-	-	-	< 1	-
Calcite	2.7	3.2	-	-	-	-	86.0
Dolomite	3.7	1.5	-	-	-	-	-
Garnet	3.9	-	-	-	-	-	-
Gehlenite	< 1	8.1	-	11.5	7.4	-	-
Hydrogarnet	-	8.8	-	-	-	-	-
f-Lime	-	-	-	-	-	-	1.1
Maghemite	-	-	6.9	-	-	-	-
Magnetite	-	-	2.6	2.9	3.2	12.3	-
Mayenite	12.0	-	-	-	-	-	-
Merwinite	-	4.6	-	-	-	-	-
Olivine	-	15.6	-	-	-	-	-
Periclase	5.6	9.0	-	-	-	-	-
Portlandite	1.0	-	1.1	-	-	-	-
Quartz	-	1.3	-	-	-	-	6.0
Srebrodolskite	-	-	-	4.4	2.6	-	-
Wuestite	-	2.9	11.3	18.5	9.3	-	-
Yoshiokaite	-	-	-	< 1	< 1	-	-
β-C_2S	20.7	-	28.5	10.3	6.1	7.2	-
γ-C_2S	-	13.1	-	-	-	-	-
Total	100.8	99.4	99.6	99.6	99.7	99.9	100

Based on these encouraging findings, a second sampling was carried out to both expand the range of slag types included in the study and to obtain enough material for additional experimental trials. This approach allowed for a more comprehensive investigation of slag behaviour under carbonation conditions and supported the development of a more robust and representative dataset. AOD1 was collected in two different months to study if the sampling time interferes with the reactivity. The chemical and mineralogical composition were detected by XRF and XRD analysis, respectively, and only after the process to remove magnetic components from the by product. The data are reported in **Table 6** and **Table 7**:

Table 6. Chemical composition of various steel slags after dry iron removal process (LOQ refers to the Limit of Quantification). The Loss on Ignition (LOI) is calculated as weight loss, with the positive value attributed to the potential oxidation of iron

Sample	**LF1** [% wt]	**LF2** [% wt]	**LF3** [% wt]	**AOD1(F)** [% wt]	**AOD1(M)** [% wt]	**EAF1** [% wt]	**EAF2** [% wt]	**Slag8** [% wt]	**Slag9** [% wt]	**BF5** [% wt]
LOI	3.3	2.5	(+1.5)	0.4	2.3	(+4.6)	(+4.7)	7.9	(+0.8)	(+2.4)
SiO_2	29.2	16.9	13.2	24.4	22.5	8.8	10.2	10.6	11.6	9.6
Al_2O_3	16.0	11.8	21.3	11.6	12.7	4.4	5.3	1.9	1.8	23.6
TiO_2	0.3	1.5	0.7	0.5	0.4	0.2	0.4	0.9	1.2	0.2
MnO	0.4	2.4	2.9	0.7	0.7	4.9	5.6	2.0	4.3	0.2
Fe_2O_3	3.7	9.0	5.2	0.7	1.5	48.3	50.0	23.1	30.4	1.1
CaO	25.7	43.0	44.5	47.5	43.4	19.2	18.3	45.0	40.2	54.3
MgO	19.4	8.5	9.2	8.9	11.9	4.8	4.6	3.5	7.3	8.7
K_2O	0.2	0.02	0.01	0.01	0.03	<LOQ	0.01	0.01	<LOQ	<LOQ
Na_2O	0.5	0.01	<LOQ	0.52	0.22	<LOQ	<LOQ	<LOQ	<LOQ	<LOQ
SO_3	0.5	2.3	1.0	0.2	0.2	0.2	0.3	0.2	0.1	1.6
P_2O_5	0.03	0.05	0.04	<LOQ	<LOQ	0.2	0.2	1.7	1.1	<LOQ
NiO	-	-	-	0.01	0.03	<LOQ	<LOQ	<LOQ	<LOQ	-
Cr_2O_3	-	-	-	0.9	1.2	5.0	2.8	0.2	0.3	-
V_2O_5	-	-	-	<LOQ	0.03	0.2	0.1	0.01	<LOQ	-
CuO	-	-	-	<LOQ	<LOQ	0.01	0.02	0.5	1.0	-
ZnO	-	-	-	0.00	0.01	0.02	0.02	0.03	0.01	-
Total	99.1	97.9	98.1	96.2	97.1	96.2	97.7	97.5	99.2	97.5

Table 7. Mineralogical composition of steel slag (second sampling) after iron-removal dry process by XRD quantification. The quantification method used is Rietveld by external standard. The estimated error of QXRD measurement is ± 1 % [60].

Sample	**LF1**	**LF2**	**LF3**	**AOD1 (F)**	**AOD1 (M)**	**EAF1**	**EAF2**	**Slag8**	**Slag9**	**BF5**
	[%wt]	[%wt]	[%wt]	[%wt]	[%wt]	[%wt]	[%wt]	[%wt]	[%wt]	[%wt]
Akermanite	1.2	-	2.0	1.2	1.1	-	-	1.2	-	-
Alite	-	3.9	3.8	2	2.5	-	-	-	-	0.9
Aluminate	3.9	9.2	15.2	0.8	2.6	-	-	-	-	-
Amicite	1.2	-	-	-	-	-	-	-	-	-
Amorphous	17.2	15.8	14.6	16.4	19.3	27.9	27.4	29.6	23.6	89.1
Andradite	-	-	3.9	-	2.6	-	-	-	-	-
Augite	-	-	-	0.9	-	-	-	-	-	-
α-C_2S	-	-	-	9.1	3.3	-	-	5.2	12.8	0.7
β-C_2S	7.1	21.0	4.4	9.0	13.9	19.0	15.5	13.1	18.8	-
γ-C_2S	8.7	12.0	22.4	2.0	6.3	2.6	-	-	-	-
Bredigite	1.8	3.1	0.6	20.2	12.1	4.7	7.5	-	-	-
Brownmillerite	-	-	2.5	-	0.5	-	-	5.7	-	-
Calcite	1.7	1.8	0.8	-	-	-	-	3.6	-	-
Chromite	-	-	-	-	-	5.2	3.1	-	-	-
Corundum	3.2	-	-	-	1.9	-	-	-	-	-
Cuspidine	1.8	-	-	9.5	6.7	-	-	-	-	-
Diopside	3.0	-	-	4.6	-	-	-	-	-	-
Dolomite	1.5	0.4	0.2	0.2	-	-	-	-	-	-
Enstatite	10.1	-	-	-	5.3	-	-	-	-	-
f-Lime	-	-	-	-	-	-	-	2.9	4.7	1.7
Forsterite	17.6	2.1	0.6	-	3.0	4.8	13.2	1.3	-	-
Gehlenite	1.4	4.8	2.3	0.7	-	-	-	-	-	-
Hausmannite	-	-	0.4	-	-	0.6	-	-	-	-
Hauyne	-	-	0.2	-	-	-	-	-	-	-
Hematite	-	-	-	-	-	-	-	0.6	-	-
Hercynite	-	-	0.4	-	-	-	-	-	-	-
Hornblende (MgFe)	2.7	4.6	-	-	-	-	-	-	-	-
Kaolinite	-	-	0.5	-	-	-	-	-	-	-
Katoite	1.8	8.1	3.3	-	2.5	0.3	1.3	-	-	-
Magnetite	-	-	0.9	-	-	-	-	1.8	4.6	-
Mayenite	3.9	3.8	12.5	5	6.0	0.8	3.3	-	-	-
Merwinite	-	-	-	5.7	-	4.9	-	1.8	-	2.1
Mullite-32	1.9	-	-	-	-	-	-	0.7	-	-
Periclase	5.2	6.0	4.8	5.2	6.8	1.1	-	-	-	2.6
Portlandite	0.2	-	0.9	-	0.4	-	-	19.1	2.2	2.9
Quartz	1.6	-	-	-	0.7	-	-	0.6	0.4	-
Spinel	-	-	-	6.9	2.6	-	-	-	-	-
Srebrodolskite	-	-	-	-	-	-	-	7.2	18.6	-
Wuestite	-	3.4	2.4	-	-	28.1	28.7	5.3	13.7	-
Total	98.6	99.9	99.7	99.4	100.0	100.0	100.0	99.7	99.4	100.0

All the slags are composed mainly of CaO, MgO, SiO_2 and Al_2O_3. Some of them contain metals as Cr, Fe, Mn and Ti. A strong correlation can be observed between the type of metallurgical process and the resulting slag characteristics, which are directly influenced by the operational parameters and metallurgical goals of each stage [71]. BF slags, produced during the reduction of iron ore in the blast furnace are typically high in Ca and Al species and the rapid cooling causes a high amorphous content. In contrast, EAF slags, resulting from the melting of scrap or direct reduced iron, show higher concentration of FeO and SiO_2, along with crystalline phases such as wuestite and belite, and other iron-rich oxides, consistent with their role in oxidizing impurities during the primary steelmaking process. AOD slags, associated with the decarburization of stainless steel, are enriched in MgO and SiO_2 and commonly contain phases such as periclase (MgO) and bredigite ($Ca_7Mg(SiO_4)_4$), reflecting basicity required for refining stainless grades. LF slags, produced during secondary refining, exhibit elevated levels of Ca and Al oxides, with mineralogical assemblages dominated by mayenite ($Ca_{12}Al_{14}O_{33}$) and calcium silicates, supporting their role in desulfurization and final chemistry adjustment [2,11]. The collected data are in line with the values collected from literature and reported in **Chapter 1**.

For the samples of second sampling, the physical analysis was executed (**Section 4.3, 4.4 and 4.5**). The particle size distribution of the various slag samples, expressed as Dv(90), Dv (50) and Dv(10), is reported in **Table 8**, after the process for removing the magnetic components. It provides insights into the granulometric characteristics relevant to processing, reactivity and potential applications. Overall, the data reveal a moderate variation in particles sizes among the different slag types, with Dv(90) values ranging from 55.4 to 69.4 µm, Dv(50) from 10.0 to 22.4 µm and Dv(10) from 1.16 to 2.97 µm. In summary, all the slags shown a particle diameter under 70 µm, but, LF and AOD slags maintains relatively consistent size distribution, whereas EAF and Slag8 and 9 demonstrate more variability maybe due to high iron content which negatively influence the grinding process.

Table 8. Particle size distribution of steel slag after pre-treatment process (crushing, grinding and sieving steps). The data are expressed as Dv(90), Dv (50) and Dv(10)

	Dv (90) µm	**Dv (50)** µm	**Dv (10)** µm
LF1	65.6	16.6	1.73
LF2	55.4	12.6	1.72
LF3	69.4	22.4	2.92
AOD1 (F)	65.2	15.0	1.84
AOD1 (M)	63.8	14.7	1.85
EAF1	55.7	12.9	2.50
EAF2	65.4	15.7	2.97
Slag8	56.2	10.0	1.42
Slag9	63.2	11.2	1.16
BF5	56.3	10.2	1.34

To improve understanding and simplify the mineralogical structure of steel slag, the QXRD data were categorized into four groups:

- Amorphous content
- Reactive phases: mineralogical phases that react in a specific carbonation process as belite, bredigite, portlandite, periclase, mayenite, aluminate and free-lime;

- Not reactive phases: mineralogical phases that don't react in a specific carbonation process such as andradite, brownmillerite, enstatite, forsterite, katoite, gehlenite and olivine;
- Carbonated products: calcite, aragonite and calcite-(Mg).

Each group represents the total concentration of its constituent phases as determined by QXRD refinement.

3.2 Steel slag pre-treatment

Steel slags typically have a particle distribution of 1–5 cm, but research [44,72] showed that smaller particles have a greater reactivity in the carbonation process Therefore, before use in carbonation reactions, steel slags were first dried at 105°C for 2 hours to remove any moisture and then crushed and ground using a crusher (Herzog HSM-100P) and a disc mill (Retsch BB51-WC) to obtain a fine powder till reaching a diameter value under 63 μm.

3.2.1 Iron magnetic component removal process

Steel slags may be used for carbonation and for cement industries, but they are underutilized. One of the reasons is the hardness which make the grinding process difficult and energy-consuming [73]. The hardness is due to the presence of Fe-metallic iron which interferes in the grinding process. The methods described in this section were selected based on the available laboratory equipment and after a comprehensive review of the relevant scientific literature [74–76]. Although the use of a disc mill is not specifically tailored for this application, it was chosen for its ability to efficiently reduce the material to a fine powder, which was the primary requirement of the project. Moreover, the disc mill enables partial separation of the various mineral phases, facilitating the distinction between the ferromagnetic and non-magnetic components. This technique proved advantageous as it allowed for effective processing while preserving the original mineralogical composition as much as possible. A variation in the concentration of Fe depends on the nature of the slag as shown in **Table 4**. Different approaches were tested to find the most efficient pathways in term of reduction of magnetic content. Three different approaches were tested: magnetic separation, disc mill separation and wet magnetic separation. The first two techniques were used only for slag with a low Fe_2O_3 as AOD and LF slag; whereas the wet method was used for AOD slag and EAF slag that have a different concentration of iron. Each test was executed after drying at 105°C and a quartation step to have a representative sample.

Magnetic separation

A magnet was passed above a representative sample until there aren't any ferromagnetic components and this part was unwrapped. Then, the sample was grinding by a disc mill and sieved (Ø < 90 μm).

Disc mill separation

A representative sample was grinding by disc mill for 1 minute and sieved (Ø < 90 μm). The fraction with diameter > 90 μm was separated and it is noted it has a different colour, and it is harder to grind. It is important to underline that the fraction under 90 μm is the 90% of the representative sample.

Wet magnetic separation

Wet magnetic separation is a process which takes advantages by combination between magnetic field and water through a specific instrument reported in Figure 3**.** First, the magnetic field turns on and the intensity can be changed based on the use. In this case, the conditions are high magnetic field, and intensity equals to 2 Ampere. A representative sample (m = 20 g) is put inside the box with iron balls which entraps the material (**Figure 3A**) Then, the box is washed with water to separate the not magnetic parts by magnetic ones. When the first components are separated, the magnetic field turns off and the box is washed again to entrap the magnetic components. All the samples are filtered and dried at 105 °C for 10 hours.

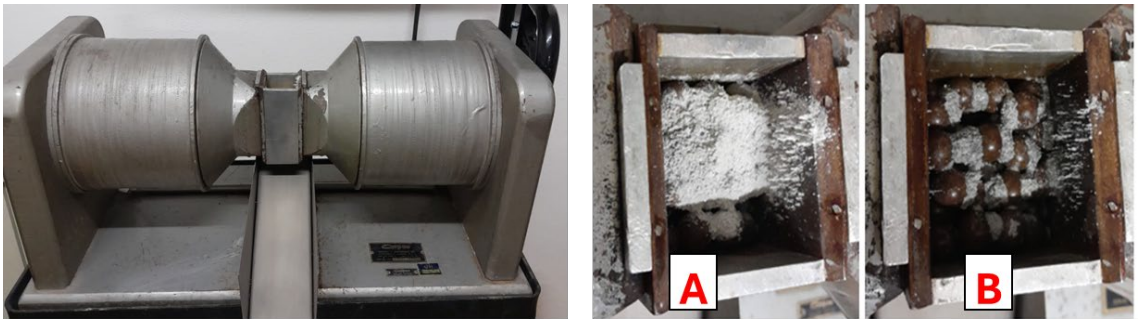

Figure 3. Wet magnetic separation process: (A) material before activation of the magnetic field; (B) material after separation and the wash with water, where only the magnetically susceptible fraction remains.

Dry magnetic separation

After different attempts for the metallic separation, a new method was tested (**Figure 4**). It combines different instrument: disc mill, crusher, magnet and sieve. The slag was dried at 105°C overnight to remove the moisture; then the sample was crushed by a crusher to reduce the particles size from 20 mm to 1-4 mm. By a magnet, the first removal was conducted, and "big" pieces of steel were collected. Then, the powder was ground in a mill and sieved under 90 µm. The process from magnet to sieve was repeated one time more and then the fraction over 90 µm was ground in a disc mill.

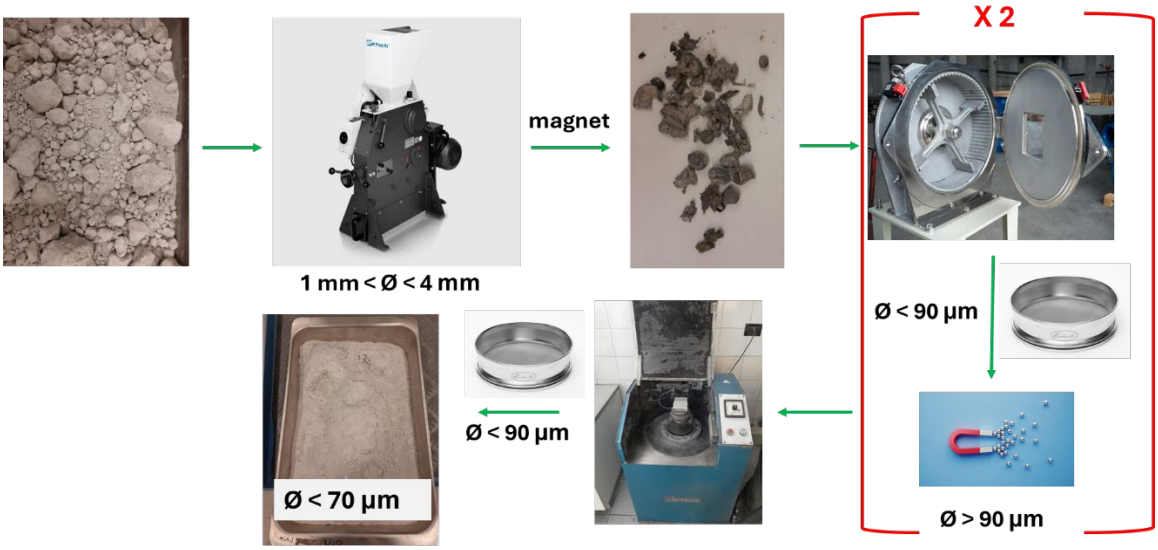

Figure 4. Dry iron metallic removal process. All steps of the procedure are illustrated: initial crushing of the material, removal of magnetic fractions using a magnetic separator, subsequent grinding, and final sieving to obtain particles smaller than 90 µm

3.3 Characterization of steel slag

3.3.1 X-Rays Diffraction (XRD) analysis

Crystalline phases of starting materials and carbonated products (**Table 5**, **Sections 4.1, 4.3** and **4.4**) were identified by X-Rays Diffraction analysis using a PANalytical X'Pert PRO diffractometer. The instrument is supplied with a Cu Kα anode and operated at 40 kV and 40 mA. The scan (2θ) has a step interval of 0.017°. The identification of the phases was executed by the software PANalytical X'Pert HighScore Plus version 2.1.0 and connected to the ICDD PDF2 database (1998). Quantitative analyses were finalized by the Rietveld method with open-source software PROFEX (version 5.0.2, released on 22 September 2022) [77], as described in a previous study [78]. As internal standard, corundum (Al_2O_3_Space Group 167, Crystal system: trigonal-hexagonal Scalenohedral (R32/c)) was used (25% in weight) because it wasn't a main phase in the samples. Crystallography Open Database (COD) was used to download all the mineralogical structures. Through this method, the CO_2 sequestered was calculated. The amorphous content (A) was calculated as followed:

$$A = 1 - \sum(MP) \tag{8}$$

where MP represents the calculated content of each mineralogical phase calculated by the Rietveld method.

PROFEX calculates the pattern (Pc) based on the crystalline phases inserted for the quantification by the fit on XRD pattern (Po). The difference line (Po – Pc) (grey line) is the subtraction between the XRD and calculated pattern. The flatter the line, the better is the fit and an example of fitting is reported in **Figure A- 15**.

The fit can be adjusted modified some parameters as:

- B1 stands for a Lorentzian broadening caused by size effects
- k1 describes a gaussian-like part of the size effects
- K2 describes the micro strain effect [79].

For each mineralogical phase, PROFEX calculates the concentration, expressed in wt%, and the error of the refinement (ESD = $\Delta\varepsilon$). All data about QXRD refinement were collected and the concentration and its specific error were plotted in **Figure 5.** Mainly, an error below 5% is related to concentration higher than 10%; whereas smaller is the percentage higher is the error due to low height and not defined peaks.

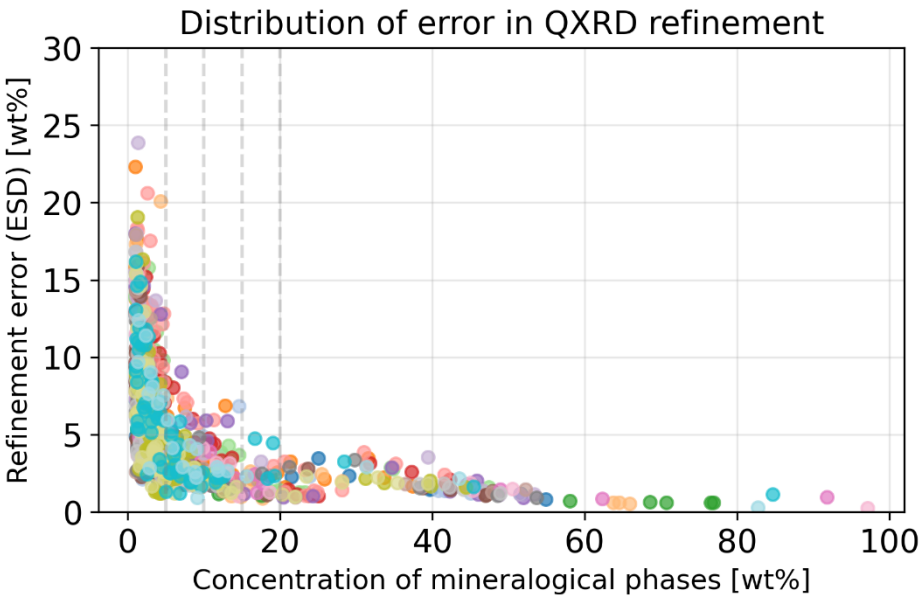

Figure 5. Distribution of error (ESD) in QXRD refinement. For each concentration, an error was calculated. Higher is the concentration smaller is the error

The XRD analysis for starting materials, carbonated products and hydrated mixes (**Table 7, Section 4.5** and **4.6**) were conducted by a Bruker D-8 Advance diffractometer in θ-θ configuration with a Cu tube (CuKα radiation, λ = 1.54059 Å) supplied with a LYNXEYE (1-d) detector. The generator operated at 40 kV and 40 mA, the acquisition range was 5-70°2θ and a step size of 0.02°2θ. The identification of the phases was done by the software DIFFRAC.EVA.V5.2; whereas the quantification analysis was executed by Rietveld method using an external standard approach. The external standard was synthetic quartz (space group 154; MAC 34.84; crystallinity 100; cell mass 180.253; density 2.648; volume 113.05531). The scale factor can change with each XRD acquisition, consequently, each day the quartz pattern was collected, and the right scale factor was used for the refinement.
Other two parameters were calculated: k-factor and MAC. The k-factor depends on the instrument parameters and was calculated as reported in **Equation 9** and MAC depends on the chemical composition by XRF analysis [80,81]. To calculate the MAC factor for each chemical element the X-Rays Mass Attenuation Coefficient was used [82]. The quantification was done by TOPAS V6 software.

$$k = \frac{S_q \cdot D_q \cdot V_q^2 \cdot MAC_q}{C_q} \quad (9)$$

where S_q is the scale factor, D_q is density, V^2_q is the cell volume, MAC_q is the MAC factor and C_q is crystallinity. All these parameters are referred to quartz (q).

3.3.2 X-Rays Fluorescence (XRF) analysis

The chemical composition of starting materials (**Section 3.1, Table 4**) was determined by a Bruker S8 Tiger 4 kW spectrophotometer. The instrument is equipped with a Rh tube and a detector gas composed by a mix of argon (90%) and methane (10%). Before the analysis, the sample was compressed into a bead and heated at 950°C to dry the powder and eliminate CO_2. 1.20 g of the

calcined sample was added to 12 g of flux, a mixture of 70% lithium tetraborate and 30% lithium metaborate. This compound acted as a solvent at 1100°C to dissolve the oxide components.

The chemical composition of starting materials and carbonated products (**Section 4.5** and **Table 6**) were conducted by a PANalytical Axios X-Ray Fluorescence Spectrometer. Firstly, the sample ((1 ± 0.05) g) was heated at 950°C for 15 minutes and then it was cooled to room temperature in a desiccator and weighed out to measure the Loss of Ignition (LOI). Successively, the sample was ground and homogenised with a pestle, and 0.7000g of the sample was mixed with 6.3000g of Fluore-x 6510LiF (mixing ratio 1:9). The mix was quantitatively transferred to an empty, pre-annealed (5 min, 1050°C ± 10°C) mould and the mould and the sample are mixed by rotating the mould. LiBr solution (5%, 2-4 drops) was added to the mix and then it was put in the muffle furnace at 1050°C ± 10°C for 6 minutes.

3.3.3 Scanning Electronic Microscopy (SEM) analysis

The morphology of these followed samples and carbonated products (AOD1, LF2, EAF3 and CKD, in **Section 4.1**) was characterized by a ZEISS EVO MA-15 instrument. It was equipped with a LaB-6 filament as electron source and the images were acquired by a secondary electron imaging. Before the analysis, the samples were covered with Pd particles to increase the conductivity, whereas the chemical composition was detected by AZTEC software version 6.1.7601 (Oxford Instruments, Abingdon, UK).

The morphology of starting material (LF2 in **Section 4.5**) and relative carbonated product was detected using ZEISS EVO LS10 instrument equipped with a XFlash Detector 610- Mini from Bruker. The sample was dried and deposited in a Teflon stamp and impregnated with a transparent epoxy resin (EpoTek® 301) under vacuum. Then it was slowly polished down to 0.25 µm by a diamond spray as lubricant and coated with a thin conductive carbon layer (30 nm). The mapping was collected by EDS-BSE technique.

The morphology of the starting materials and carbonated products in **Section 4.3** was detected by NANOEYE SNE-ALPHA tabletop SEM equipped with EDS detector. The sample was covered by Au particle to increase the conductivity, and the images were acquired as SE (secondary electron) image.

3.3.4 Infrared Spectroscopy (IR) analysis

The starting materials and the corresponding products (AOD1, LF2, EAF3 and CKD in **Section 4.1** and samples in **4.3** and **4.4**) were analysed by the Nicolet iN10 Infrared Microscope (ThermoFisher Scientific, Milan, Italy) in transmittance mode using a barium fluoride window. Each spectrum was collected with a spectral resolution of 8 cm^{-1} over 16 scans. The spectra were analysed using OMNIC software version 9.11.475 to detect the band.

The starting materials, carbonated products and hydrated mix (**Section 4.5** and **4.6**) were analysed by a Perking Elmer Spectrum instrument. The acquisition range is 380-4000 cm^{-1} and for each sample, 3 spectra were acquired, and the final spectrum was obtained by the average of transmittance values.

3.3.5 Particle Size Distribution (PSD) analysis

The particle size distribution analysis of the samples in **Table 8** were detected by Malvern MasterSizer 3000 in wet dispersion (isopropanol) using a particle range of 0.01-2100 µm. The data were collected by Fraunhofer evaluation method.

3.3.6 Thermogravimetric (TGA) analysis

Thermogravimetric analyses TGA (NETZSCH STA F449) were conducted on a range 30 ± 2 mg of sample (based on the density of the powder) using an open vessel in N_2 atmosphere and a heating scale of 20 K/min up to 1050°C. The percentage of calcite, presented in **Table 18** and in **Figure 34,** was calculated by the following equation:

$$\mathrm{Cc}\ (\%) = \left(\frac{\mathrm{Cc_{CO2}}(\mathrm{M_{400°C}} - \mathrm{M_{850°C}}) \cdot (\frac{100}{44})}{\mathrm{M_{850°C}}} \right) \cdot 100\% \qquad (10)$$

where Cc_{CO2} is the mass loss of CO_2 present in calcite, $M_{850°C}$ and $M_{400°C}$ is the mass loss at 850°C and at 400°C.
The carbonation degree was calculated using the percentage of CaO and MgO determined by XRF:

$$\mathrm{Carb.\,Degree}\ (\%) = \frac{\mathrm{mol\ CO_{2(seques)}}}{\mathrm{mol\ CO_{2(theor)}}} * 100 \qquad (11)$$

3.4 Carbonation set-up

Different set-ups were used in this work to test the influence of reaction parameters and reaction conditions.

3.4.1 High-pressure Carbonation test (small set-up)

The **Figure 6** describes the first set-up used in this work [66]: all the components were made of stainless steel from AISI 304 or 316L. By a pipette, the sample was transferred into a 150 mL volume sample barrel (SB) and then it was connected to a pressure transducer (PT) which recorded the gas pressure values with an accuracy of 0.125% and a rate of 100 values per second. The temperature was measured by a thermocouple (TC) outside and both pressure and temperature were collected by LabVIEW software every 5 seconds. Before the carbonation, the air inside was eliminated by a vacuum pump and then the CO_2 was injected into the barrel until it reached 15 bar. Then the valve was closed and the system isolated. Each step of the process was weighted using an electronic scale (accuracy of 0.1 g). If the initial mass and the final mass corresponded, no loss of CO_2 was underlined. The accelerated carbonation tests were conducted under uniform reaction conditions (room temperature, p = 15 bar, L/S = 1.5 ml/g and particle size less than 106 µm). Upon reaching 15 bar pressure, the valve was closed, and the injected CO_2 was approximately 2.50-2.60 g based on the environmental conditions.

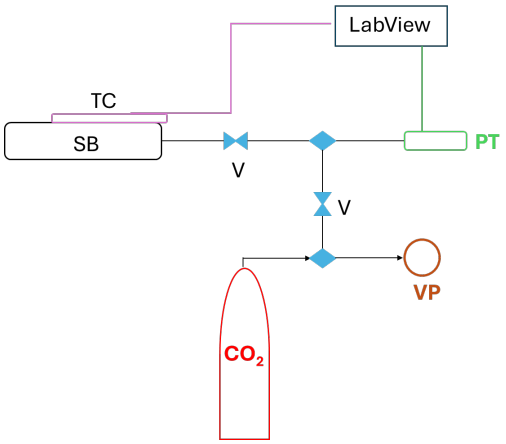

Figure 6. Scheme of the experimental setup: sample barrel (SB), thermocouple (TC), needle valves (V), vacuum pump (VP) and pressure transducer (PT) [66].

The mass of sequestered CO_2 was calculated using three different methods:

1. The Rietveld method with the internal standard (Corundum, Al_2O_3) was employed to quantify the mass of sequestered CO_2 associated with crystalline phases. Since XRD analysis only detects mineral phases with a crystalline structure, only calcite and aragonite were identified. If other carbonate phases had formed, they would not have been detected by this technique due to their amorphous nature. Furthermore, given the complexity of the mineralogical composition of steel slags, the system was simplified by considering only calcium silicates, the main reactive phases, using the following **Equation 12**:

$$Ca_2SiO_4 + 2CO_2 \rightarrow 2CaCO_3 + SiO_2 \quad (12)$$

The calculation of CO_2 content was calculated following these formulas:

$$\text{mol}\,(CaCO_3) = \text{mol}\,(CO_2) = \frac{m_s * \%CaCO_3}{MW_{CaCO3}} \quad (13)$$

$$\text{mass}\,CO_2 = (\text{mol}\,(CO_2) * MW_{CO2}) - m_i(CO_2) \quad (14)$$

where m_s is the sample mass after the carbonation, expressed in grams and weighted by a technical balance after dry process, $\%CaCO_3$ is the percentage of Rietveld calculation, MW_{CaCO3} and MW_{CO2}, is the molecular weight of $CaCO_3$ and CO_2, respectively, and m_i (CO_2) is the initial mass of CO_2 present in the sample, calculated by the **Equations 13-14**. The error was calculated by followed the **Equation 15**:

$$\Delta x = \left(\sqrt{\left(\frac{\Delta\varepsilon}{\%CaCO_3}\right)^2 + \left(\frac{\Delta m}{m_s}\right)^2} \right) \cdot m(CO_2) \quad (15)$$

were $\Delta\varepsilon$ is the error calculated by PROFEX, the software used for QXRD, $\%CaCO_3$ is the value calculated by Rietveld refinement, Δm is the balance accuracy (0.1) and m_s is the final mass of carbonated slag after dry process.

2. The amount of sequestered CO_2 was quantified by the difference between the final mass of the CO_2 sequestered and the initial mass of CO_2 injected. The setup is a closed system, and each component (slurry, barrel, CO_2) were weighted step by step. The sequestered CO_2 mass

was the difference between the final mass of the setup and the removal of the unreacted CO_2 and the initial mass of the setup. If the initial and final mass are equal a lack of CO_2 is not present. The absolute error (Δx) corresponds to the accuracy of the balance (0.1).

3. The perfect gas law was used by monitoring the pressure trend during the process using the initial pressure (p_i), final pressure (p_f) and initial mass of CO_2 as in the following equation:

$$m_f(CO_2) \text{ sequestered} = m_i\,(CO_2) * (1 - p_f/p_i) \quad (16)$$

The absolute error was calculated using the followed equation:

$$\Delta x = \sqrt{\left(1 - \frac{p_f}{p_i} \cdot \Delta m\right)^2 + \left(\frac{m_{f\,(CO2)}}{pi} \cdot \Delta p_f\right)^2 + \left(\frac{m_{f\,(CO2)} \cdot p_f}{p_i^2} \cdot \Delta p_i\right)^2} \quad (17)$$

where p_f and p_i represent the final and initial pressure, respectively, m_f (CO_2) is the mass of CO_2 sequestered. Δm refers to the balance accuracy used for weighing, while Δp_i and Δp_f are uncertainties associated with the pressure transducer, calculate as the percentage of the corresponding values (initial (i) and final (f)).

Finally, in three methods, the overall error was scaled in accordance with the final value of the sequestered CO_2 mass, as **Equation 18** shown:

$$Err = \Delta x \cdot \left(\frac{100}{m_s} \cdot 10\right) \quad (18)$$

3.4.2 Optimization of accelerated carbonation set-up

Based on tests conducted in the small set-up, the system shows some criticities:

- Insertion of sample was difficult due to not homogeneity of the sample
- No stirring
- No change of liquid-solid ratio
- No control of the inner temperature
- Extraction of the sample was not a conventional way

Consequently a high-pressure reactor was buyed in order to get better the carbonation process and eliminate the limitations of the small set-up. In the **Table 9** the two options are compared. The advantages of the Berghof set up are inner temperature control, variation of water volume, magnetic stirring and an easy extraction and insertion process.

Table 9. Comparison of technical characteristics of two reactors: the small set-up and high-pressure reactor (Berghof). The table underlines the main differences between the two proposed options

CHARACTERISTICS	SMALL SET-UP	BERGHOF SET-UP
Wet carbonation	Yes	Yes
Sample extraction/insertion	Difficult	Easy
T control	External	Internal
L/S	> 0.9	No limit
CO_2 mass	2-2.5 g	8-9 g
Stirrer	No	Yes
Autoclave	No	Yes

To verify the possible difference between the two options, a carbonation test was executed used the same reaction condition (15 bar, room temperature, L/S = 1.5) and same sample (LF2). As **Figure 7** shows, in the high-pressure reactor (Berghof set up), the reactive species completely reacts with CO_2 to form calcite and aragonite. Moreover, the mass of CO_2 sequestered is double than in small set up because the volume of the barrel is bigger, the injected CO_2 mass is higher, and the stirring speed was working. The CO_2 sequestered was calculated based on Rietveld data as shown in **Equations 13-14.**

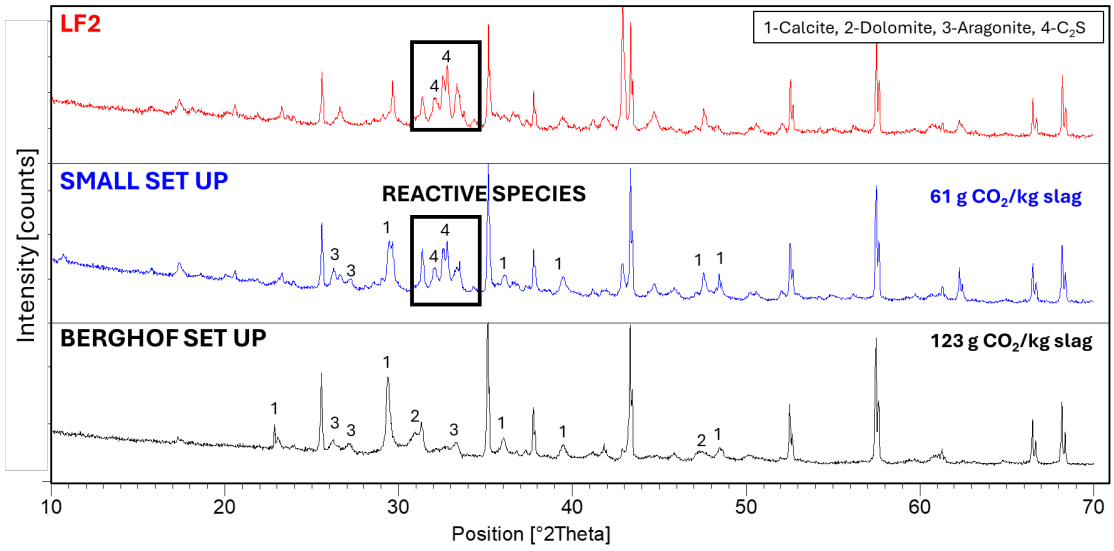

Figure 7. XRD patterns comparing the mineralogical composition of the same slag (LF2) sample before carbonation, after carbonation in small and Berghof set up. The experiments were conducted in the same conditions: 24 hours, room temperature, L/S = 1.5 and 15 bar. The differences in peak intensities and the appearance/disappearance of specific phases indicate varying extents of CO_2 sequestration and transformation of reactive phases, with Berghof 2 showing a higher degree of carbonation.

3.4.3 High-pressure carbonation set-up (Berghof Reactor)

The carbonation reaction was conducted in a high-pressure reactor (made by Berghof) in a stainless-steel reactor covered by PFTE insert (total volume 310 mL) reported in **Figure 8**. 30 g of slag, weighted at electronic scale (accuracy ± 0.1g) was diluted in 45 mL of distilled water (L/S = 1.5). After the closing of the reactor, the magnetic stirring was activated at different speed (60, 125 and 250 rpm). Successively, the CO_2 was injected until 15 bar and then the valve was closed. Pressure and temperature were collected by the set-up each minute. The reaction was running for 24 hours and then the sample was dried at 105°C overnight and ground by a mortar.

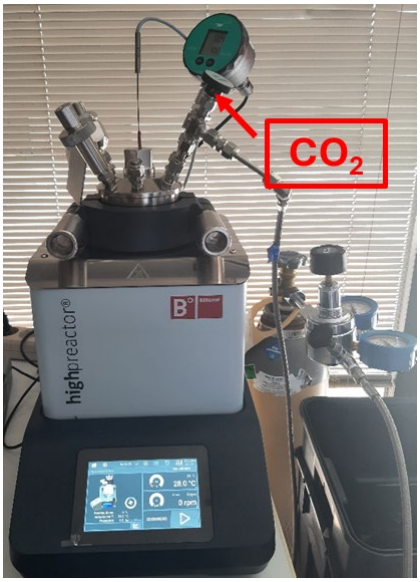

Figure 8. High-pressure reactor equipped with an internal thermocouple for temperature monitoring, a CO_2 inlet valve for controlled gas injection, a heating jacket, and a magnetic stirrer to ensure uniform mixing. The carbonation reaction was conducted for 24 hours at ambient temperature, using three different stirring speeds: 60, 125, and 250 rpm. This setup allows the investigation of the effect of mixing intensity on the efficiency and kinetics of the high-pressure carbonation process.

The calculation of sequestered CO_2 was made by two methods:

- Rietveld Calculations: the mass of captured CO_2 was calculated by the **Equations 13-14**
- Perfect gas Law: the value regarding the CO_2 uptake was calculated by the **Equation 16.**

The aim of this Section is to demonstrate the repeatability of the tests conducted under the described experimental conditions. The values regarding QXRD and sequestered CO_2, reported in the main text, represent the average of two tests, and the associated error is expressed as the standard deviation.

3.4.4 Mild condition environmental carbonation

Steel slags were mixed with distilled water to prepare a slurry, using a liquid-to-solid ratio in the range of 0.7–0.9 mL/g. This range was selected based on the solubility characteristics of each slag type, with the goal of achieving a homogeneous and stable slurry. The extent of slag dissolution was influenced by its specific chemical composition, which affected the overall consistency of the mixture.

Once prepared, the slurry was poured into circular moulds and placed into three separate sealed containers, each dedicated for a different curing period (1 month, 2 months, and 1 year), as illustrated in **Figure 9**. The samples were then exposed to natural carbonation under laboratory conditions, allowing them to react with atmospheric CO_2 over time without any forced gas injection or pressure enhancement. This setup aimed to simulate a passive carbonation environment and assess the long-term behaviour of each slag type. For each sample, XRD analysis were collected, and pH test was executed by the dissolution of the slag in MilliQ water (L/S =10) and measured by a pH-meter (Metrohm, model 827 Laband).

Figure 9. Sample preparation for natural carbonation experiments. Steel slag was mixed with water to form a slurry, which was then poured into moulds to shape the samples. These were subsequently exposed to ambient environmental conditions (airborne CO_2 and O_2) for different durations, 1 month, 2 months, and 1 year, to investigate the effects of natural carbonation over time. This setup simulates passive CO_2 uptake from the atmosphere under uncontrolled but realistic conditions.

The sequestered CO_2 is calculated following the **Equations 13-14** and the corresponding error is calculated by the **Equation 15**.

3.4.5 Enforced carbonation at room temperature and pressure

The carbonation reaction was conducted in a glass beaker (1L), and it was equipped with a pH-electrode (SevenExcellence S475A probe from Mettler Toledo, with a pH electrode Inlab Expert Pro-ISM, precision ± 0.05 pH units), a magnetic stirrer and a sponge to inject continuously CO_2. The pH-electrode was calibrated using 3 different standard solutions with pH values at 4, 7 and 10, provided by Mettler Toledo, before each test. 200 g of slag were diluted in 1000 ml of NaOH solution (0.1 M) which was acidified by the injection of CO_2 for 20 minutes before the addition of the material. The experiment was conducted at 20°C, 100% vol CO_2 and the gas flow was 100 L/h (glas flow meters by Vögtlin Instruments). After 6 hours, the agitation was stopped and the steel slag was filtered, dried in an oven at 105°C overnight and ground for 40 seconds in a disc mill (Siebtechnik) with a steel jar. The **Figure 10** illustrates the set up.

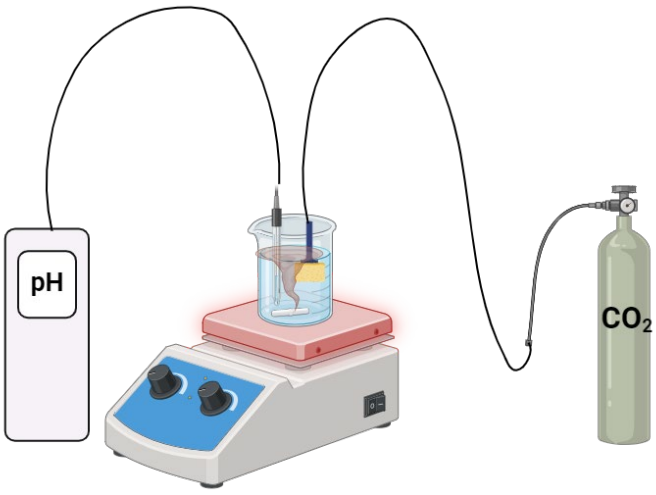

Figure 10. Enforced carbonation experimental setup. The system includes a pH meter that continuously records data over a 6-hour period, a sponge for controlled CO_2 injection (100% CO_2), and a magnetic stirrer to maintain homogeneous mixing of the solution. Prior to the carbonation process, CO_2 was dissolved in a 0.1 M NaOH solution to enhance the dissolution of the gas and the formation of carbonate ion thereby promoting more efficient carbonation. This setup enables the simulation of accelerated mineral carbonation under controlled chemical and physical conditions. Image was created by Biorender.com

3.5 Cement performance

3.5.1 Micro mortar mixes

Composite cements were formulated by partially replacing Ordinary Portland Cement (CEM I 52.5R, conforming to EN 197-1 standards) with both untreated and carbonated steel slags. The resulting mixtures were designated as CEM-Sx for those containing untreated slag, and CEM-Cx for those incorporating carbonated slag, where "x" denotes the specific slag type employed. In each formulation, 40% of the OPC was substituted with steel slag, used as a supplementary cementitious material. To accelerate early-stage hydration, a high-purity synthetic additive (99%) was introduced. For comparison, a reference mix comprising the same OPC blended with natural limestone (containing approximately 95% calcium carbonate) was prepared and labelled CEM-L. The mechanical performance of these composite binders was evaluated using micro mortar samples at different curing times (1, 2, 7, 28 and 90 days). Each batch contained a total of 220 g of cementitious material (132 g OPC and 88 g slag or limestone), mixed with 330 g of ISS1 standard sand (maximum particle size 0.4 mm). Subsequently, 110 g of deionized water was added, corresponding to a water-to-cement ratio (w/c) of 0.5. All mixtures were prepared in accordance with the EN 196-1 standard, with additives introduced last to ensure consistent proportions between cement and slag. The complete mix compositions are detailed in **Table 10**:

Table 10. Detailed experimental design of mortar mixes including the proportion of each component, expressed in percentage (L is limestone)

Sample name	CEM [%]	Steel slag/LIM [%]	Additives [%]
CEMI	100	-	-
CEMI_L	60	40	-
CEM_Sx	60	40	-
CEM_Cx_1.5%	60	40	1.5 HH
CEM_C1_1%	60	40	1 HH, 1 NC, 1 NS

where HH is hemihydrate ($CaSO_4 \bullet 0.5H_2O$), NS is sodium sulphate (Na_2SO_4), NC is sodium carbonate (Na_2CO_3) and x is 2, 3, 8 and 9, corresponding respectively to LF2, LF3, Slag8 and Slag9. After the preparation of mortar mixes and the compaction on the vibrating table, they were filled into a special made steel mould, covered and stored in a humidity chamber (20 ± 2°C and 50% RH) for 24 hours. Then, the cubes (2 cm x 2cm x 2 cm) were demoulded, and the cubes were stored under running tap water until the testing date. The mechanical performance, namely the compressive strength, was tested using Toni Technique instrument with a load speed of 0.4 MPa/s. For each designed testing day, 6 cubes were tested. The data reported in **Figure 43** and **Figure 44** are the average values and also standard deviation is reported as error measurement.

3.5.2 Calorimetry analysis

6 g of sample was used for isothermal calorimetry and the heat of reaction was measured for 3 days at 20°C by an 8-channel TAM Air calorimeter. The pastes were mixed using cement and supplementary cementitious materials in the followed proportion 0.60/0.40 by adding the accelerators as shown in **Table 10**. Quartz was used as reference in the calorimetry channel. The results are normalized by total amount of the paste.

3.5.3 Hydration mix

The paste was prepared by 60% of by-product (untreated (MIS-Sx) and carbonated (MIX-Cx)), 39% of portlandite (Merck product) and 1 % NaOH in a w/c = 0.85 (the ratio considers NaOH solution as water, extra water was not added). The role of NaOH is mimic the alkali concentration presents in the cement. The powder mix was homogenized in a Turbula for 30 minutes and then the mix was mixed for 1 minute using a shaker. Small vessels were filled with the paste and closed. The tests were conducted at 1,2,7,28 and 90 days. The experiments were conducted at 20°C ± 1°C and the stoppage of hydration process consisted of a solvent exchange process by 150 ml of 2-propanol and 150 ml of petroleum ether. The sample was put in a vacuum chamber (p = -0.06 bar) until the solvent evaporated completely. XRD and TG analysis were done and the portlandite was calculated by the formula:

$$\mathrm{CH}\ (\%) = \left(\frac{\mathrm{CH_w}(\mathrm{M_{420°C}} - \mathrm{M_{500°C}}) \cdot (\frac{74}{18})}{\mathrm{M_{850°C}}} \right) \cdot 100\% \cdot \mathrm{M(BW)_{850°c}} \quad (19)$$

where CH_w is the loss mass of water from portlandite and $M(BW)_{850°C}$ is the loss mass of water at 850°C. $M_{420°C}$ is the starting value of the decomposition of portlandite.

CHAPTER 4

RESULTS

4.1 High-pressure Carbonation (small set-up)

The results reported in this section are collected in the paper "Accelerated Direct Carbonation of Steel Slag and Cement Kiln Dust: An Industrial Symbiosis Strategy Applied in the Bergamo-Brescia Area", published on 29th of May 2023 in section "Materials" in the journal MDPI [66].

Table 4 provides the chemical composition results of the collected samples, which demonstrate significant variability depending on the type of steel scraps and the specific process involved [11]. LF/AOD slags were characterized by higher percentage of reactive compounds as CaO and MgO, whereas EAF slags exhibited a greater amount of Fe_2O_3. These data align with previous studies reported in literature [10,11,83–87]. Notably, EAF3 slag contained a higher percentage of SiO_2 due to the addition of SiO_2 fume (20% in weight) during the grinding process. The CKD sample displayed a substantial CaO content (44.7%), but part of this Ca is contained in calcite in accordance with XRD pattern (in **Figure A- 1G**) and the high loss of ignition (LOI) value (29.92), as it reflects both the mass reduction caused by decarbonation and the loss of water. According to Abdel-Ghani et al. [69], CKD underwent partial calcination, and the observed weight loss is attributed to CO_2 release, associated with the presence of calcite as the dominant phase in the XRD pattern, show in **Figure A- 1G**. This observation agrees with previous findings [84,87].

The XRD spectra for both steel slags and relative carbonated products are displayed in **Figure A- 1** and QXRD refinement are reported in Table 5 and in **Table A- 1**. The LF2 and AOD1 slags shared similar main phases as gehlenite ($Ca_2Al(AlSi)O_7$), periclase (MgO) and dicalcium silicate (Ca_2SiO_4). The presence of silicate compounds was also confirmed by IR spectroscopy (**Figure A- 2**), where the characteristic Si-O bond symmetric stretching was observed in the 1200–800 cm^{-1} region. Bands within this range are attributed to β-C_2S, γ-C_2S, merwinite, and bredigite [88]. In the case of the EAF1 slag, the main crystalline phases were identified as larnite (Ca_2SiO_4), wuestite (FeO), maghemite (Fe_2O_3), and brownmillerite ($4CaO{\cdot}Al_2O_3{\cdot}Fe_2O_3$). For EAF2 slag, the dominant phases included gehlenite ($Ca_2Al(AlSi)O_7$), wuestite (FeO), magnetite (Fe_3O_4), and larnite (Ca_2SiO_4), as shown by the XRD patterns in **Figure A- 1E**. These latter two phases were also predominant in the EAF3 slag, as indicated in **Figure A- 1F**. IR analysis further verified the mineralogical phases identified: β-C_2S exhibited a vibration band at 805 cm^{-1}, amorphous silica showed a stretching vibration at 1111 cm^{-1}, and the carbonate ion displayed bending and stretching vibrations at 871 cm^{-1} and 1469 cm^{-1}, respectively (**Figure A- 2C**). These findings are consistent with previously published studies [11,44,89,90].

Regarding the carbonation process, the pH of the slurry was measured using pH paper before (pH_i) and after (pH_f) carbonation. The initial (p_i) and final pressure (p_f) data are summarized in **Table 11**. For all the samples, about 30 g of the slag was inserted.

Table 11. Reaction parameters (initial and final) for the high-pressure carbonation process at 15 bar, including pH, initial and final pressures, and the mass of CO2 injected, with the parameters referring to the carbonation reaction at elevated pressures.

Sample		AOD1	LF2	EAF1	EAF2	EAF2+ SiO_2	EAF3 + SiO_2	CKD
pHi		13	13	12	10	12	13	12
pi	**[bar]**	15.1	15.1	14.9	15.0	15.0	15.0	15.0
pHf		9	9	9	8	8.5	10	8
pf	**[bar]**	2.2	4.0	6.0	7.2	7.1	5.5	7.6
mCO_2 injected	**[g]**	2.53	2.59	2.44	2.59	2.69	2.69	2.57
$m_{s\ (initial)}$	**[g]**	30.7	31.2	30.2	32.1	30.1	30.5	30.5
$m_{s\ (final)}$	**[g]**	32.9	33.1	31.6	33.1	31.4	32.2	31.6

During the carbonation reaction, the internal pressure evolution was monitored by recording data at specific time intervals. **Figure 11** displays the pressure trends observed up to 20 hours of reaction time. All experiments were conducted for a total duration of 24 hours, except for the CKD sample, for which pressure measurements were interrupted at 20 hours due to external factors. However, the cumulative data presented in **Table 11** refer to the full 24-hour period. In all samples, a general decrease in pressure over time was observed, reflecting the progressive uptake of CO_2. Nonetheless, the pressure decay profiles varied significantly between the different materials, primarily due to the intrinsic reactivity and mineralogical composition of each matrix. For instance, highly reactive phases in AOD and LF slags facilitated a more rapid and complete CO_2 uptake, leading to a stabilization of internal pressure within 24 hours, suggesting near-complete reaction. In contrast, EAF slag and CKD exhibited a slower pressure decline, likely due to a lower content of reactive Ca- and Mg-bearing phases, resulting in a partial carbonation under the same conditions. Interestingly, a minor pressure increase—or "jump"—can be observed within the area highlighted by the grey rectangle in **Figure 11**. This anomaly is attributed to the repositioning of the reactor barrel from a vertical to a horizontal orientation, which temporarily increased the contact surface area between the CO_2 gas phase and the slurry. This enhanced interaction likely caused a brief acceleration in the carbonation reaction, as more reactive surface became available. The results also suggest that process parameters such as mixing and reactor geometry could be optimized to improve overall carbonation efficiency, particularly for materials with lower initial reactivity.

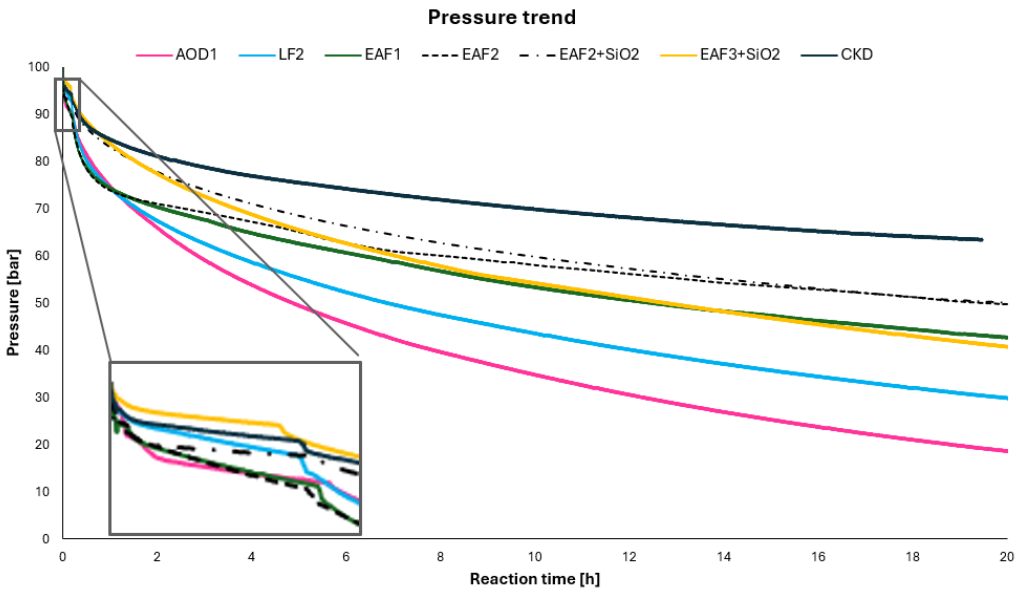

Figure 11. The graph illustrates the decreasing trend of CO_2 pressure consumption over a 20-hour process. Each slag exhibits a unique pattern, highlighting how CO_2 consumption varies based on the specific characteristics of each slag. This different behaviour reflects the complexity of the process and the distinct response of each slag to the treatment.

To calculate the sequestered CO_2, the Rietveld method is commonly used. However, high background (fluorescence effect of iron) in EAF samples and complex XRD pattern for AOD and LF samples makes the interpretation difficult and complex. For these reasons, as underlined in **Section 3.4.1,** three methods were used to quantify the captured CO_2 to check the accuracy of the data (**Figure 12**). The errors of three methods were calculated based on the **Equations 15, 17** and **18** in **Section 3.4.1** and they were under 3%. The major error values are of weighting method because the accuracy of the balance is 0.1 g.

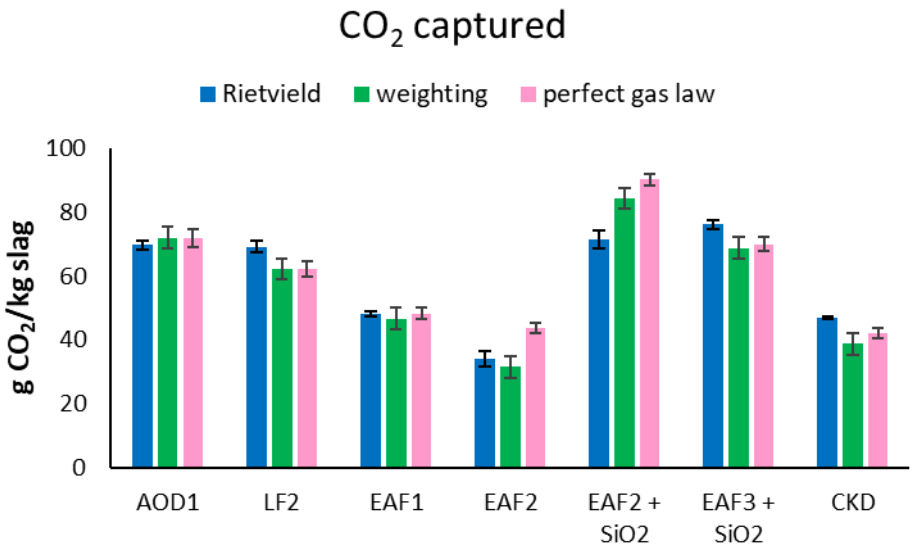

Figure 12. Carbonation results about sequestered CO_2 by high-pressure reactor using three quantification methods: Rietveld, by weight and perfect gas law. The results refer to tested steel slag. The error bar represents the error for each calculation method. The equations are reported in the **Chapter 3.4.1**

Despite of similarity in three methods, some differences were observed. For example, EAF2 had a high concentration of Fe_2O_3, which contributed to the quick separation of the slurry. During the sample charging process, the excess water may have diluted the CO_2 in water rather than allowing

it to be adsorbed by the sample, potentially leading to an overestimation of the amount of CO_2 sequestered.
When comparing the CO_2 sequestration capacities of the steel slags, it is evident that AOD and LF slags demonstrated similar performances, likely due to their distinct mineralogical and chemical compositions. As show in **Figure A- 1** and in **Table 5,** these slags contain Ca-based species, such as dicalcium silicates and mayenite, which are highly reactive in the carbonation process [42,43]. This trend also explains the pressure decrease observed for AOD1 and LF2 in **Figure 11**, where the presence of different Ca species enhanced the leaching of Ca^{2+} into the water, promoting the reaction with CO_2. Consequently, the pressure dropped rapidly within the first few hours.
Moreover, in LF2 periclase reacts, although there was no evidence of crystalline magnesite formation in XRD pattern (**Figure A- 1**). While the formation of amorphous magnesite or hydro magnesite is possible, its confirmation was not feasible due to the unknown composition of the amorphous phase. Both LF2 and AOD1 exhibited the formation of calcite and aragonite, with LF2 being confirmed via IR spectroscopy at 1470 cm^{-1} (**Figure A- 2**). Also, SEM images (**Figure 14**) confirmed the formation of carbonated products: for AOD1 calcite present an irregular and crystalline shape, whereas in LF2 $CaCO_3$ was in the form of long needles (**Figure A- 3**). Additionally, the low content of iron minerals in these slags favoured the carbonation process. In fact, when the experiment occurs in an oxidative environment (as in this study), the iron compounds were oxidized and form a surface layer of hematite (Fe_2O_3), which has low solubility [91], impeding the interaction between CO_2 and the slurry and thereby slowing the reaction kinetics and decreasing ionic diffusivity [92,93]

Conversely, the Electric Arc Furnace (EAF) slag contains significantly higher concentrations of iron oxides, such as Fe_2O_3 and Fe_3O_4, which are characterized by their inherently low solubility in water [91]. This low solubility leads to the rapid sedimentation of solid particles when the slag is mixed with water, thereby hindering the formation of a stable and homogeneous slurry. As a result, the solid phase quickly separates from the liquid, compromising the uniform distribution of the material and making the slurry preparation process considerably more challenging.

This lack of homogeneity not only affects the reproducibility and consistency of the experimental setup but also impacts the subsequent carbonation performance, as the reduced contact surface between the reactive solid and CO_2 can limit the efficiency of the reaction. Furthermore, during the reactor loading phase, the rapid decantation led to operational difficulties, including uneven dosing and poor dispersion of the material within the system. These findings highlight the need to optimize pre-treatment or dispersion techniques—such as the use of dispersing agents, mechanical stirring, or alternative mixing protocols—when working with high-Fe slag systems to ensure proper slurry stability and maximize carbonation potential. Among the EAF slags, EAF3 demonstrated the best performance, likely due to its lower iron content and higher levels of amorphous silica, which is soluble at high pH [94], facilitating the dissolution of calcium ions and maintaining slurry homogeneity. The amorphous decreases in carbonated products (**Figure 13**) which may include some reactive species that could not be identified.

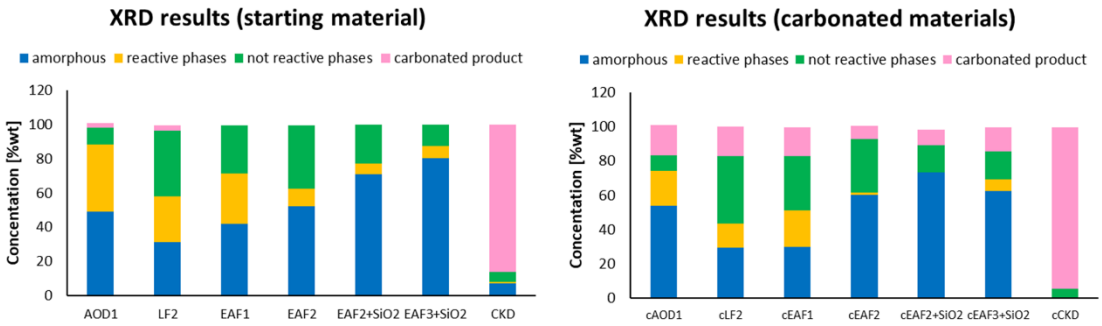

Figure 13. Quantitative phase analysis of untreated and carbonated slag samples obtained by Rietveld refinement. The 4 groups are the sum of mineralogical data obtained by QXRD refinement. The graph illustrates the changes in mineralogical composition following the carbonation process.

Furthermore, SEM images show a change in morphology after the carbonation. In fact, in the starting materials two phases were recognized: amorphous silica in the form of small and circular particles and crystal minerals present in the slag, whereas the carbonated product was homogenous, and calcite was growing on C_2S crystals (**Figure A- 4** and **Figure A- 5**).

In EAF2, the presence or absence of SiO_2 yielded different outcomes: the slurry initial pH increased from 10 to 12 with the addition of silica (**Table 11**) and the CO_2 uptake increases in the EAF2+SiO_2 sample. This experimental evidence suggests that SiO_2 promoted the carbonation process while improving slag solubility and slurry homogeneity at higher pH levels. EAF1 also demonstrated strong CO_2 sequestration potential. Although EAF1 contained the highest percentage of CaO compared to other EAF slags, slurry decantation and consequently less inserted sample mass affect the results.

Both EAF1 and EAF2 exhibited similar pressure trends (**Figure 11**) during the first two hours, likely due to rapid calcium ion leaching, followed by a change in trend that may be related to the decantation of iron components.

CKD exhibited the poorest pressure behaviour (**Figure 11**), likely due to calcite being the dominant phase, which has low solubility in water and does not easily react with CO_2. Despite this, CKD showed a notable CO_2 sequestration capacity, likely due to the presence of calcium oxide not only in its crystalline form but also possibly in the amorphous phase, influenced by the specific collection point of the CKD sample [6]. Indeed, the amorphous phase in the carbonated product decreased as indicated in **Figure 13**. Unfortunately, it was not possible to precisely determine the chemical composition of the amorphous phase. However, FT-IR analysis suggested the potential formation of a Ca-rich silica phase at 1060 cm^{-1} (which was not detected by XRD analysis because amorphous) [95] and confirmed the presence of calcite in the 800–1500 cm^{-1} range, which its particles have a different morphology due to completely absence of control in the particle growth [96] as demonstrated in the SEM picture (**Figure 14C-D**).

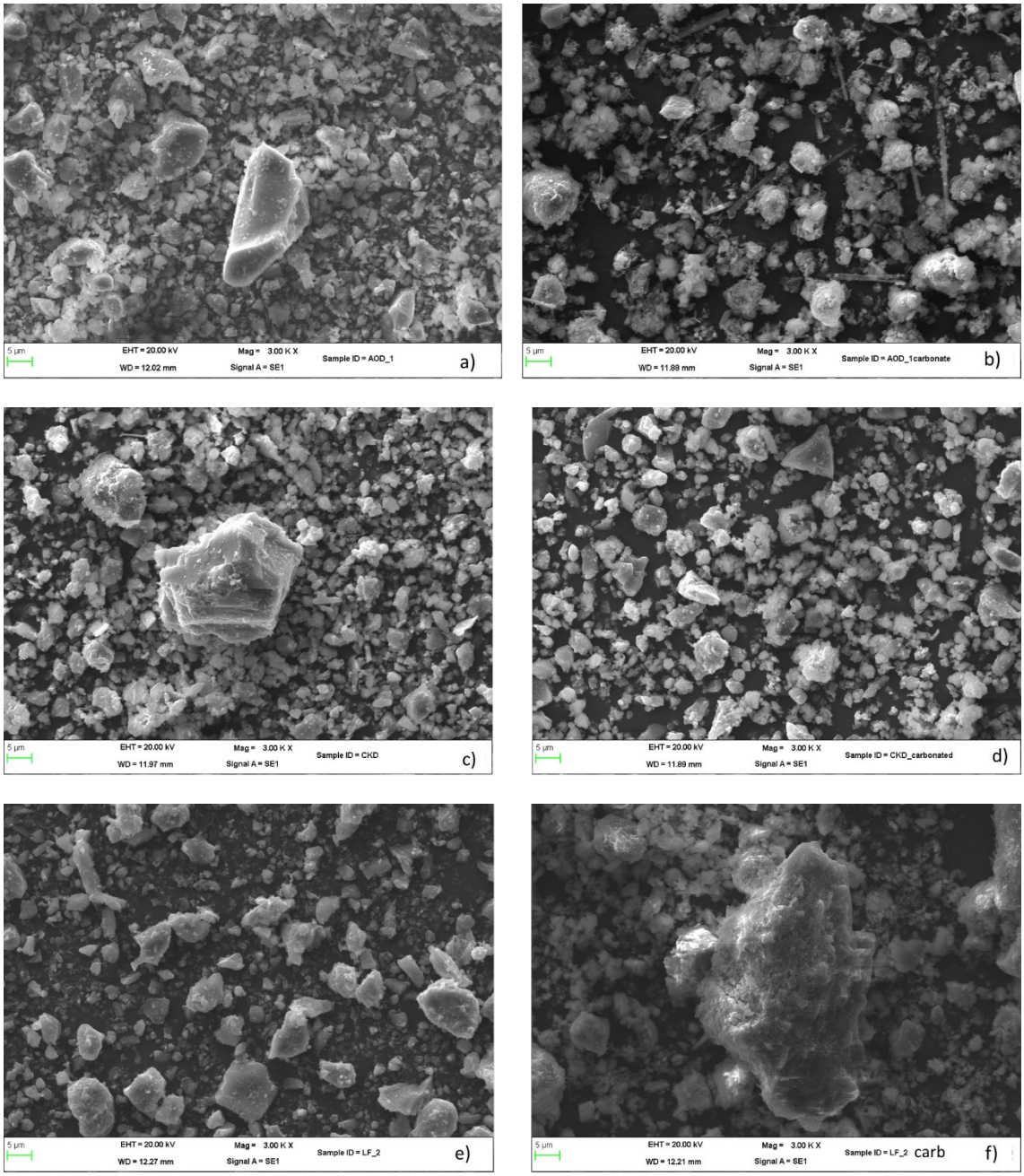

Figure 14. Comparison of SEM images of byproducts before and after carbonation. In particular, these pictures represent AOD 1 slag (a) and AOD1-carb (b); CKD (c) and CKD-carb (d); LF2 (e) and LF2-carb (f)

In conclusion, by this set-up about 70 g of CO_2/kg of slag can be sequestered, value that can change based on type of slag. As explained previously, with this set-up the completely carbonation of the materials was not refuse and only belite phases are considered in the calculation as shown in **Equation 12**, because C_2S is the main reactive phases and the system is complex. Consequently, the calculations don't consider the amorphous products and if all amount of CaO (**Table 4**) reacts steel slags can sequestrate 200-313 g CO_2/kg for slag, aligning with literature findings [53,97,98]. On the other hand, CKD captured about 55 g CO_2/kg of material but its potential is close to 124-240 g CO_2/kg of CKD. Literature studies [99,100] have demonstrate CKD might be more efficient in an indirect method, where Ca and Mg are leached using solvents and then reacted with CO_2. For this reason, CKD was not condisered for other tests.

4.2 Iron magnetic component removal process

4.2.1 Magnetic and Disc mill separation

Argon Oxide Decarburization slag

AOD1 slag contains the lowest Fe_2O_3 concentration than other slags. The application of magnetic and disc mill separation lead to a decrease in the ferrous species in both cases even if with different results as show in **Table 12**. In fact, in the first case, the quantity is halved whereas in the second case the quantity is below 1%. Again, a magnet is passed over the part with diameter > 90 µm and the ferromagnetic property is verified in agree with chemical analysed. It is important to underline that the chemical composition of the most present species remains unchanged. Probably the magnetic separation is less efficient due to the "power" of the used magnet or because after grinding process some ferromagnetic parts were extracted.

Table 12. Comparison of chemical composition of AOD1 slag before and after the treatment with a magnet and disc mill separation. The data were detected by XRF analysis

	AOD1	**Magnetic separation**	**Disc mill separation**
	[%wt]	[%wt]	[%wt]
SiO_2	24.5	23.9	24.4
Al_2O_3	11.2	11.9	11.6
Fe_2O_3	2.94	1.42	0.80
CaO	48.3	47.7	50.8
MgO	8.76	8.80	9.30

Ladle furnace slags

- Ladle Furnace slag (LF1)
  LF1 contains about 9% of Fe_2O_3. The sample is not homogenous, but it consists of a fine components and chunks (Ø < 3 cm). A representative sample is sieved (Ø < 600 µm) to separate these two components and they are analysed separately by XRF analysis, after a grinding process to reach a size closed to 90 µm. As shown in **Table 13**, the powder contains low percentage of Fe_2O_3 whereas the chunk part contains higher quantity. Otherwise, the chunks contain also other important elements as Ca, Al, Si and Mg, consequently this fraction can't be excluded.

Table 13. Comparison of chemical composition of LF1 slag fractions (powder and chunks) after a sieving process (Ø < 3 cm). The data were detected by XRF analysis

	LF1	**powder**	**chunks**
	[%wt]	[%wt]	[%wt]
SiO_2	26.8	24.4	27.6
Al_2O_3	14.8	17.6	13.2
Fe_2O_3	8.90	3.71	13.4
CaO	25.7	34.0	22.6
MgO	18.7	11.1	21.4

The application of magnetic and disc mill separation lead to a decrease in the ferrous species in both cases. The results are similar as shown in the **Table 14**.

Table 14. Comparison of chemical composition of LF1 slag before and after the treatment with a magnet and disc mill separation. The data were detected by XRF analysis

	LF1	Magnetic separation	Disc mill separation
	[%wt]	[%wt]	[%wt]
SiO_2	26.8	26.8	26.7
Al_2O_3	14.8	15.8	16.2
Fe_2O_3	8.90	4.74	4.33
CaO	25.7	28.5	29.3
MgO	18.7	16.42	15.7

- Ladle furnace slag (LF2)
  For LF2 the grinding time was changed to check if this parameter can influence the separation of interested component. As reported **Table 15**, there is any change in the percentage of Fe_2O_3 in comparison with the starting material. This result represents that the techniques used are not suitable for remove ferromagnetic components and maybe the main Fe phases present in this samples haven't magnetic properties.

Table 15. Comparison of chemical composition of LF2 slag before the treatment and after several treatment: magnetic and disc mill separation, grinding process by different time (1 minutes and 30 seconds). The data were detected by XRF analysis

	LF2	Magnetic separation	Disc mill separation	Grinding 1 min	Grinding 30 sec
	[%wt]	[%wt]	[%wt]	[%wt]	[%wt]
SiO_2	15.2	16.5	16.8	17.0	17.0
Al_2O_3	10.2	12.1	12.1	11.7	12.6
Fe_2O_3	17.5	17.0	16.9	18.6	13.9
CaO	40.3	37.0	38.8	37.2	40.5
MgO	7.85	7.23	6.71	6.91	6,83

4.2.2 Wet magnetic separation

Argon Oxide Decarburization slag

For this material, an aqueous separation technique was tested. A representative sample was placed in the separator, and it was immediately observed that Fraction 1, composed of magnetic particles, was attracted by the magnet (see **Figure 3**). However, this technique did not allow for a complete separation of the two fractions, as also confirmed by the XRD patterns (in **Figure 15**). Although the magnetite peak is less intense in the fraction 2, which was not trapped by the magnet, most of the other mineral phases are still present in both, indicating that the magnetic separation was only partially effective.

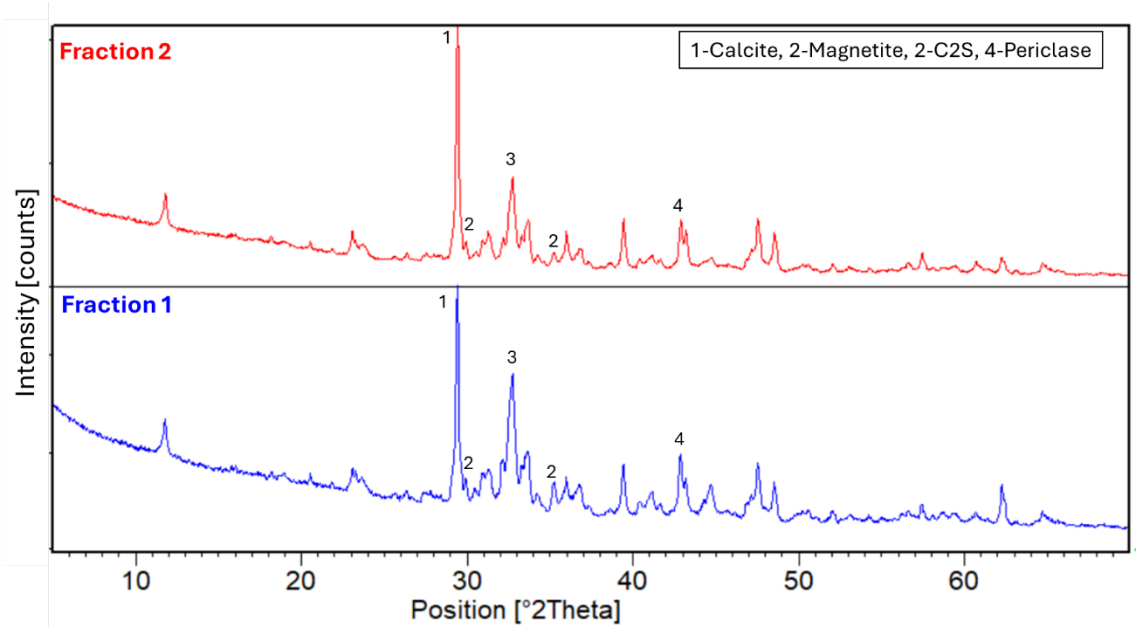

Figure 15. Comparison of XRD pattern of AOD1 slag fractions obtained by magnetic separation in wet process: iron magnetic fractions, magnetically susceptible fractions (Fraction 1), and no iron magnetic fraction (Fraction 2). Only the main mineralogical phases were highlighted to consider Iron phases, involved in the separation.

Electric Arc Furnace slag (EAF1)

EAF slag contains high percentage of Fe_2O_3 (about 51%). Aqueous magnetic separation is tested. Also in this case, based on XRD data, this approach doesn't isolate the Fe part even if the magnetite phase is separated as reported in **Figure 16**. In fact, the main Fe-phases are wuestite (FeO) and brownmillerite ($Ca_2(Al,Fe)_2O_5$) which are not magnetically susceptible.

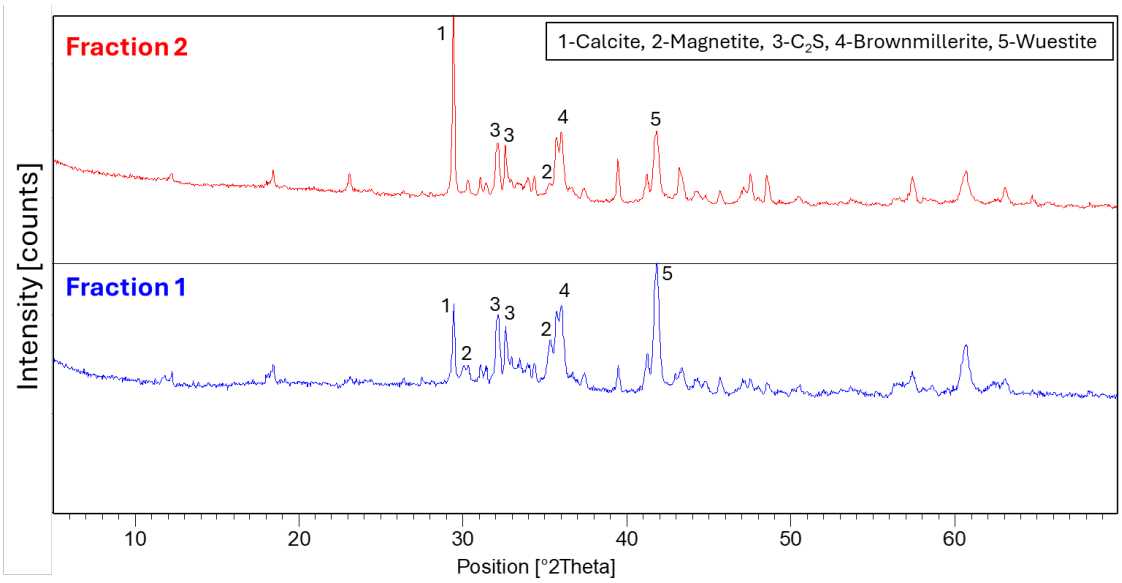

Figure 16. Comparison of XRD pattern of EAF1 slag fractions obtained by magnetic separation in wet process: iron magnetic fractions, magnetically susceptible fractions (Fraction 1), and no iron magnetic fraction (Fraction 2). Only the main mineralogical phases were highlighted to consider Iron phases, involved in the separation.

In both cases, calcite is formed may be due to the interaction of slag and CO_2 present in the air during the wet extraction. In conclusion, when the slags are powdering the Fe separation is

difficult due to compactness of the material. For EAF the process is more difficult due to higher content of FeO.

4.2.3 Dry magnetic separation

Chemical analysis by XRF were executed to check if this process modified the chemical composition for other elements as Ca, Al, Si and Mg which are the main components in all the samples. From the **Figure 17,** the concentration of principal oxides is unchanged, consequently, the gradual removal of magnetic fragment works better than the separation of a powder. Moreover, for LF and AOD samples the Fe_2O_3 percentage decreases of half of the value. In fact, Fe is present as magnetic phases (magnetite and maghemite) but also as no-magnetic compounds as brownmillerite, hornblende, wuestite etc. For EAF slag, the process was not efficient as for the other samples due to the nature of the slag, the presence of high percentage of iron and the dark colour which isn't allowed to distinguish the metallic parts.

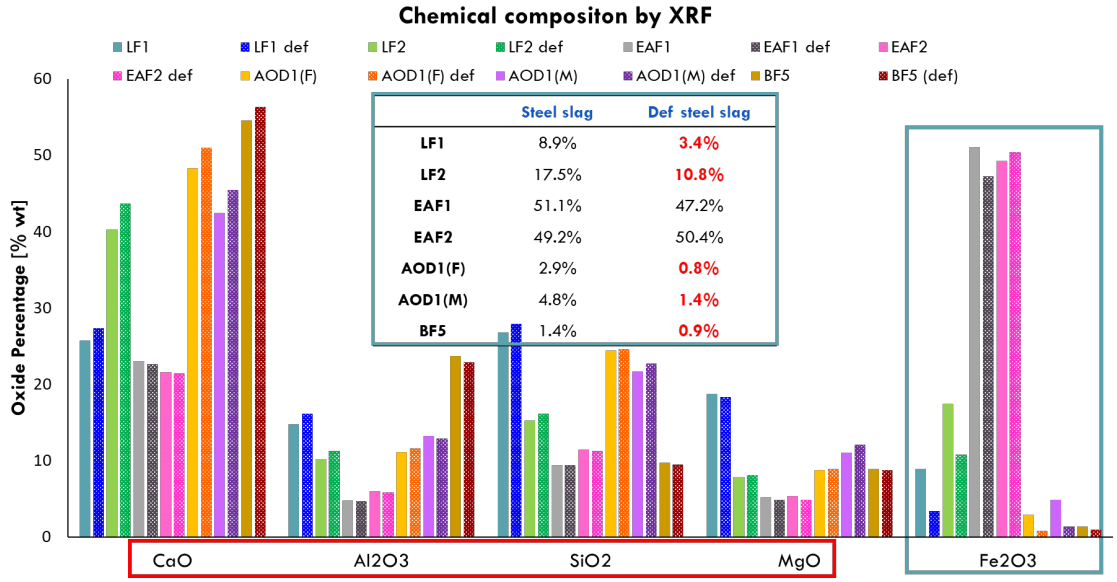

Figure 17. Chemical composition of steel slag after the dry iron metallic removal process. The graph represents the main oxides content before and after the iron separation. In the table, the iron oxide (Fe_2O_3) percentage is reported to underline the reduction of it

4.3 High pressure carbonation (Berghof set up)

Based on different chemical composition, LF1 and LF3 were chosen to study the stirring speed influence on carbonation process at high pressure to understand which stirring speed is better for an optimization of the process. LF1 was selected due to higher percentage of MgO (19.4 %) to verify the Mg role in this process, whereas in LF3 for the highest content of CaO (44.5%) than collected LF slags. As described in **Section 3.4.3,** the reaction was conducted at about 15 bar, room temperature and a liquid to solid ratio 1.5 (ml/g). To invest the influence of stirring speed three different values were used: 60, 125 and 250 rpm. For all the three speed three tests were executed using only water (45 ml) as a blank to check CO_2 dissolution in the liquid. **Figure 18** represents the average pressure values for each stirring speed value. Three repetitions are reported in **Figure A-6** and each test is like other ones. Moreover, **Table 16** represents the initial and final reaction parameters for blank test. As demonstrated in **Figure 18**, there is not a significant difference in the pressure trend when the stirring speed changes.

Table 16. Reaction parameter for blank test reporting pressure, temperature and stirring speed and beginning and the end of reaction. The three different colours were used to distinguish three different stirring speed: 60 rpm (pink), 125 rpm (green) and 250 rpm (purple)

		Blank1	Blank2	Blank3	Blank4	Blank5	Blank6	Blank7	Blank8	Blank9
v	**[rpm]**	60	60	60	125	125	125	250	250	250
p_i	**[bar]**	16.5	15.7	15.7	17.1	15.2	16.4	16.0	16.7	16.0
T_i	**[°C]**	25.5	28	30.27	29.1	28.01	31.1	23.9	28.6	29.9
p_f	**[bar]**	12.9	11.9	11.8	13.1	11.4	12.0	12.3	13.2	11.7
T_f	**[°C]**	26.5	28.9	28.4	27.9	26.5	28.5	26.4	29.5	27.3

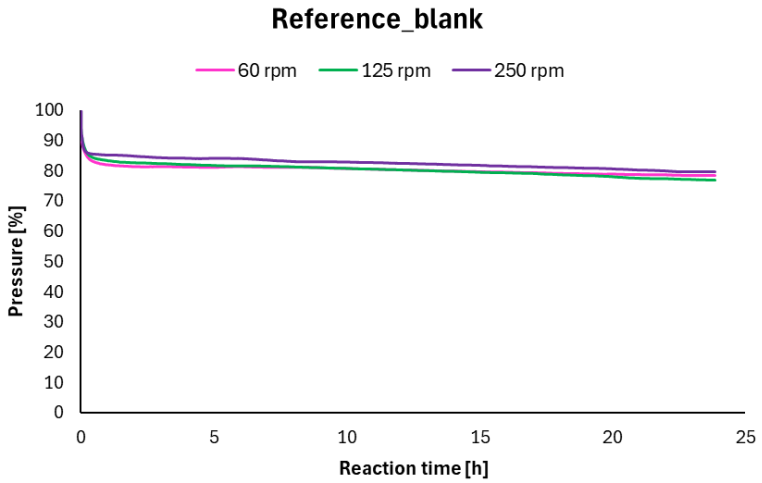

Figure 18. The graph illustrates the decreasing of CO_2 pressure consumption over a 24-hour process, room temperature and 15 bar. Three different stirring speed were tested 60 (pink curve), 125 (green curve) and 250 rpm (purple curve). The trend was similar in all the three cases and the 80% of injected CO_2 didn't react

The pH of the slurry was measured by pH paper before and after carbonation and for both materials the initial pH is around 12 due to alkaline content and it decreases until 7 due to the formation of calcite. For each material and each speed two tests were executed to verify obtained results. In fact, the optimization of the carbonation process in the high-pressure reactor is still ongoing and the execution of a second test is to check if the system is closed, consequently no gas lacks are presented, and if the process has a certain repeatability. In the main manuscript, only a test for each speed is reported but the comparison between two repetitions is reported in the graphs in **Figure A- 7** and **Figure A- 8**. For each test, the CO_2 was injected after 1 minute of stirring only even if the initial temperature is different from 25°C to address hydration time of the slag that can interfere with the carbonation process as observed for BF5 in **Section 4.4.2**. To a better understanding of the process, all the initial and final parameters are reported in this document. **Table 17** resumes the reaction conditions of the first tests indicated with number 1, whereas the repetitions are labelled with number 2 (the data are presented in **Table A- 2**).

Table 17. Reaction parameters (initial and final) for the high-pressure carbonation (Berghof set up) process at 15 bar, 24 hours, including pH, initial and final pressures and temperature, three different stirring speed, final mass of the dry sample and initial injected CO_2 mass, with the parameters referring to the carbonation reaction for LF3 and LF1. The table shows the data regarding one test for each speed and material

		LF3_60_1	LF3_125_1	LF3_250_1	LF1_60_1	LF1_125_1	LF1_250_1
v	**[rpm]**	60	125	250	60	125	250
pH_i		12	12	12	12	12	11
p_i	**[bar]**	16.3	18.4	16.9	16.8	15.4	16.9
T_i	**[°C]**	26.5	25.8	24.1	25	26.2	25.5
pH_f		8	8	8	7	7	7
p_f	**[bar]**	1.61	2.65	2.77	5.66	4.37	4.06
T_f	**[°C]**	26.4	26.6	27.8	28.4	26.7	28
m_{sf}	**[g]**	39.4	38.1	38.8	34.1	33.4	33.0
mCO_2 injected	**[g]**	9.1	10.2	9.5	9.4	8.6	8.6

As the **Table 17** indicated, it was not possible to achieve exactly 15 bars of pressure due to the closing valve time. To make the pressure trend independent from the starting values, the pressure was reported in percentage as shown in **Figure 19** for LF3 and in **Figure 20** for LF1. In general, mechanical stirring may affect the dissolution of ions in solution and make the crystallization uniform [101]. In both materials, the stirring speed influences the kinetic of CO_2 adsorption: in fact, higher speed increases the adsorption rate of pressure [102]. This phenomenon is evident in the first 5 hours because the pressure diminishes of 60% in all the cases. As underlined in the graphs, the 60 rpm curve decreases slower than 125 and 250 rpm line. In fact, the high stirring speed causes that CO_2 bubbles interact with the solution by a higher shear stress and, consequently, these bubbles break and dissolve rapidly. Moreover, this event increases the amount of generated CO_3^{2-} ions and consumed Ca^{2+} ions in the first hours favouring the reaction [102]. Additionally, the temperature is influenced by stirring speed. As well-known, the carbonation reaction is an exothermic process, and this energy is released mainly in the first hour, as reported in **Figure 19C-D** and **Figure 20C-D**. In fact, higher the speed higher is the temperature peak in the first hour due to the faster reaction and consequently the energy is released previously.

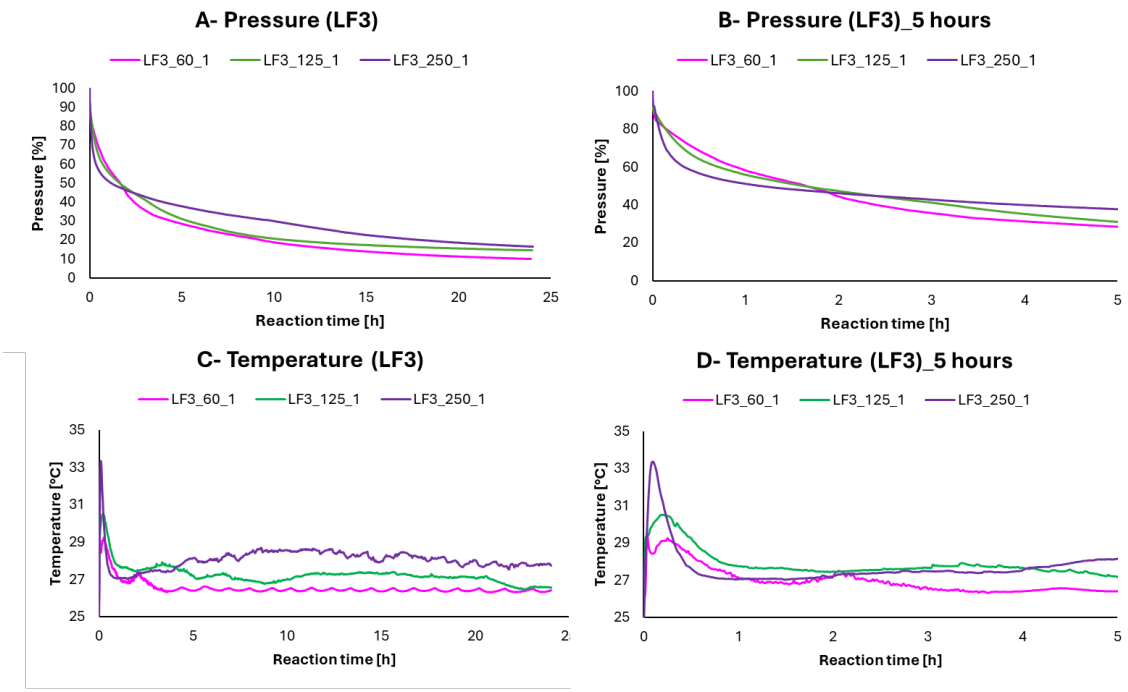

Figure 19. This figure illustrates the behaviour of CO_2 pressure and temperature over time at three different flow rates: 60, 125, and 250 for LF3 slag. Picture A shows the overall trend of CO_2 pressure decreasing over a 24-hour period, highlighting how the pressure varies depending on the flow rate. Graph B provides a closer look at the pressure drop within the first 5 hours, allowing for a more detailed comparison in the early stage of the process. Image C presents the temperature evolution over the full 24-hour period for the three flow conditions, while graph D focuses on the temperature changes during the first 5 hours, offering insight into the initial thermal dynamics

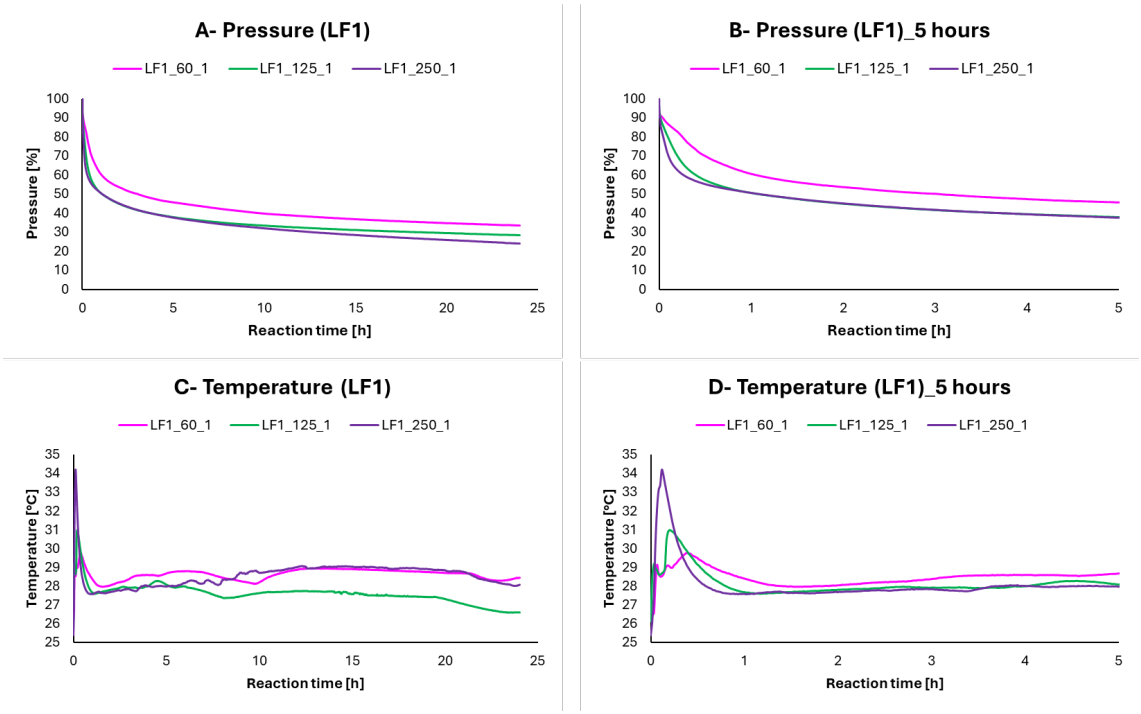

Figure 20. This figure illustrates the behaviour of CO_2 pressure and temperature over time at three different flow rates: 60, 125, and 250 for LF1 slag. Picture A shows the overall trend of CO_2 pressure decreasing over a 24-hour period, highlighting how the pressure varies depending on the flow rate. Graph B provides a closer look at the pressure drop within the first 5 hours, allowing for a more detailed comparison in the early stage of the process. Image C presents the temperature evolution over the full 24-hour period for the three flow conditions, while graph D focuses on the temperature changes during the first 5 hours, offering insight into the initial thermal dynamics

Comparing the pressure and the temperature tendency in the same graph for the first 3 hours, two peaks in temperature trend are noted in **Figure 21A-B.** In fact, when CO_2 is injected into the reactor the temperature increases for few minutes (first peak) and then, after a quick decrease, the value increases again (second peak) due to the reaction start. In the case of 250 rpm test these two peaks coalesce in one may due to a rapid reaction in these conditions, as demonstrated in **Figure 21C.** Same results are observed for LF1 in **Figure A- 9**.

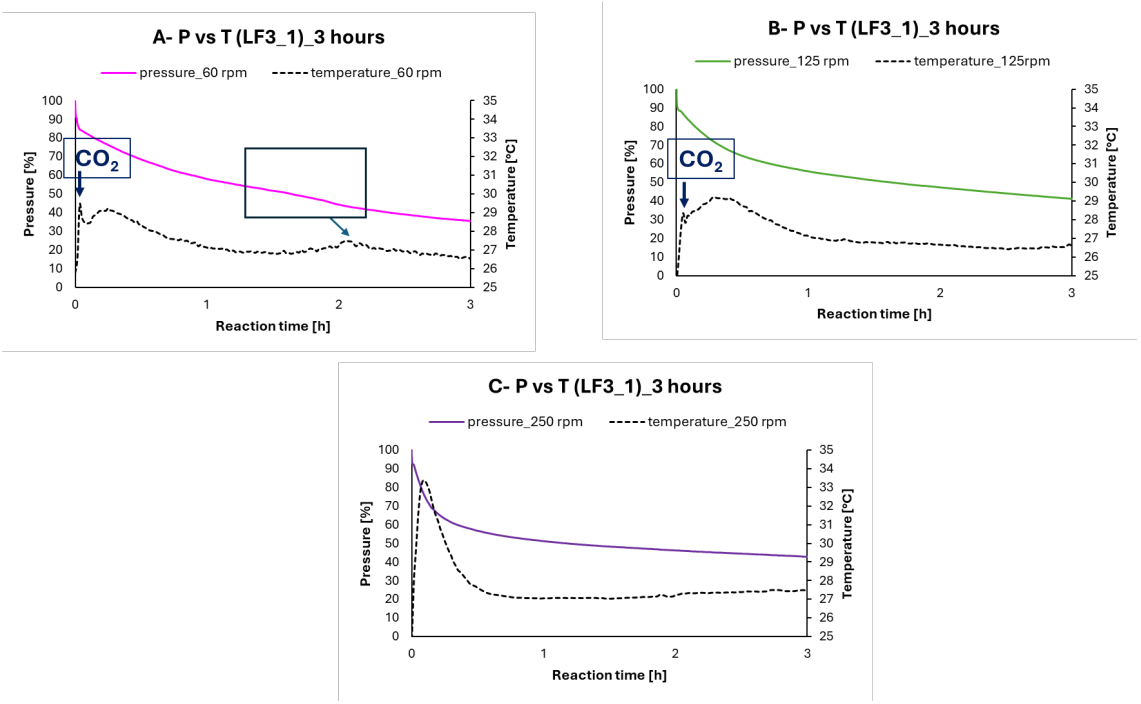

Figure 21. Comparison between CO_2 pressure and temperature trends for LF3 slag during the first 3 hours of reaction at different stirring speeds: *(A)* 60 rpm, *(B)* 125 rpm, and *(C)* 250 rpm. In each graph, a noticeable correlation is observed between temperature peaks and sharper drops in pressure, suggesting an active phase in the reaction process. Temperature is represented by dotted lines, while pressure trends are shown as continuous curves, highlighting the dynamic interplay between thermal and pressure changes at varying stirring intensities

As reported in **Table 17**, LF3 and LF1 have a different behaviour in the carbonation reaction. In fact, final pressure in LF3 is lower than that of LF1 due to a lower content of reactive phases in the starting material, respectively 58 % and 34.4 % by Rietveld method, as shown in **Figure 23**. The presence of high content of MgO but a lower content of CaO **(Table 6)** may be the cause of a low reactivity. In fact, Mg phases as enstatite are not reactive and the low percentage of Ca-reactive phases as belite and aluminate influence negatively the performance of this byproduct, as demonstrated in **Table 7** and **Table A- 3**. Consequently, the content of carbonated products is different because in LF3 the three polymorphs of $CaCO_3$ are present, calcite, aragonite and vaterite, whereas in LF1 only calcite is formed as demonstrated in **Figure 24.** However, in both cases Mg-calcite is formed with a concentration minor 5 % and the amorphous content increase as the results of the formation of Si-gel and $CaCO_3$ amorphous [59,103,104], as demonstrated in **Table A- 3.** The formation of Si-gel is confirmed also by FT-IR spectra (in **Figure 22**) in the silica region at 1110-1000 cm^{-1}, where the band of C_2S at 980 cm^{-1} is transformed in a wide band at 1040 cm^{-1} but it also remains in the carbonated products as confirmed by XRD pattern.

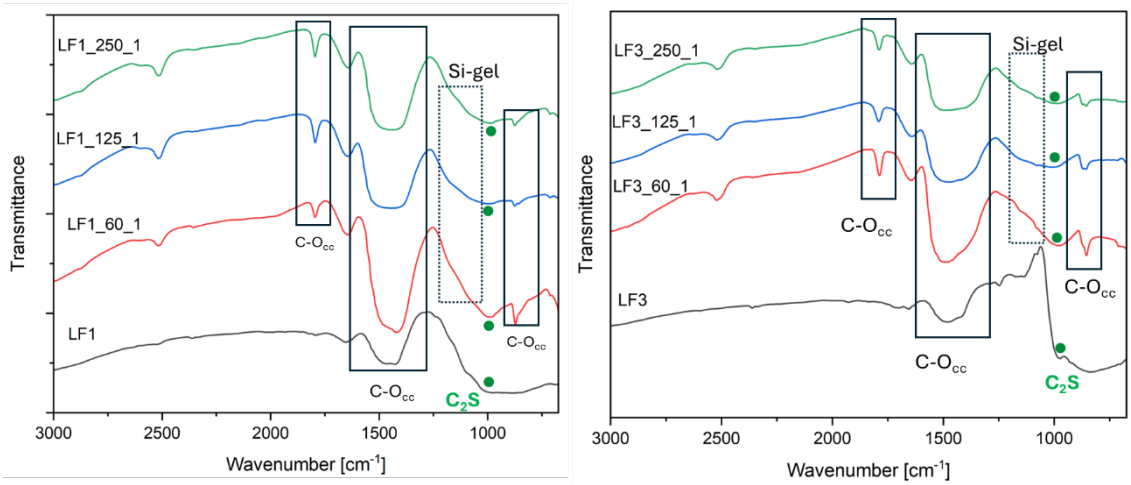

Figure 22. FT-IR spectra of LF1 and LF3 and corresponded products at different stirring speed. The spectra underlined the formation of calcite and Si-gel in the carbonated samples independent by the stirring speed. The large band around 3000-3500 cm^{-1} is correlated with the moisture content of the sample

Moreover, the reactive phases do not completely disappear, even if in LF3_125_1 the percentage is the highest compared to that at 60 and 250, respectively 20 %, 12% and 14% [105]. This is due to the presence of some Ca-phases as mayenite that don't react efficiently at 125 test1 maybe caused by the solubility of the phase. In fact, the reaction is conducted following a thin-route film process and the low liquid to solid ratio may make dissolution of Ca^{2+} ions difficult influencing negatively the general performance of the material.

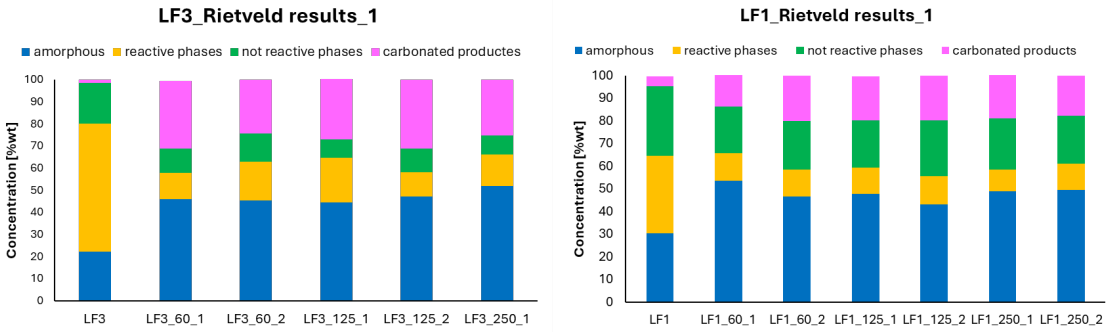

Figure 23. Quantitative phase analysis of untreated and carbonated slag samples (LF1 and LF3) obtained by Rietveld refinement. The 4 groups are the sum of mineralogical data obtained by QXRD refinement. The graph illustrates the changes in mineralogical composition following the carbonation process.

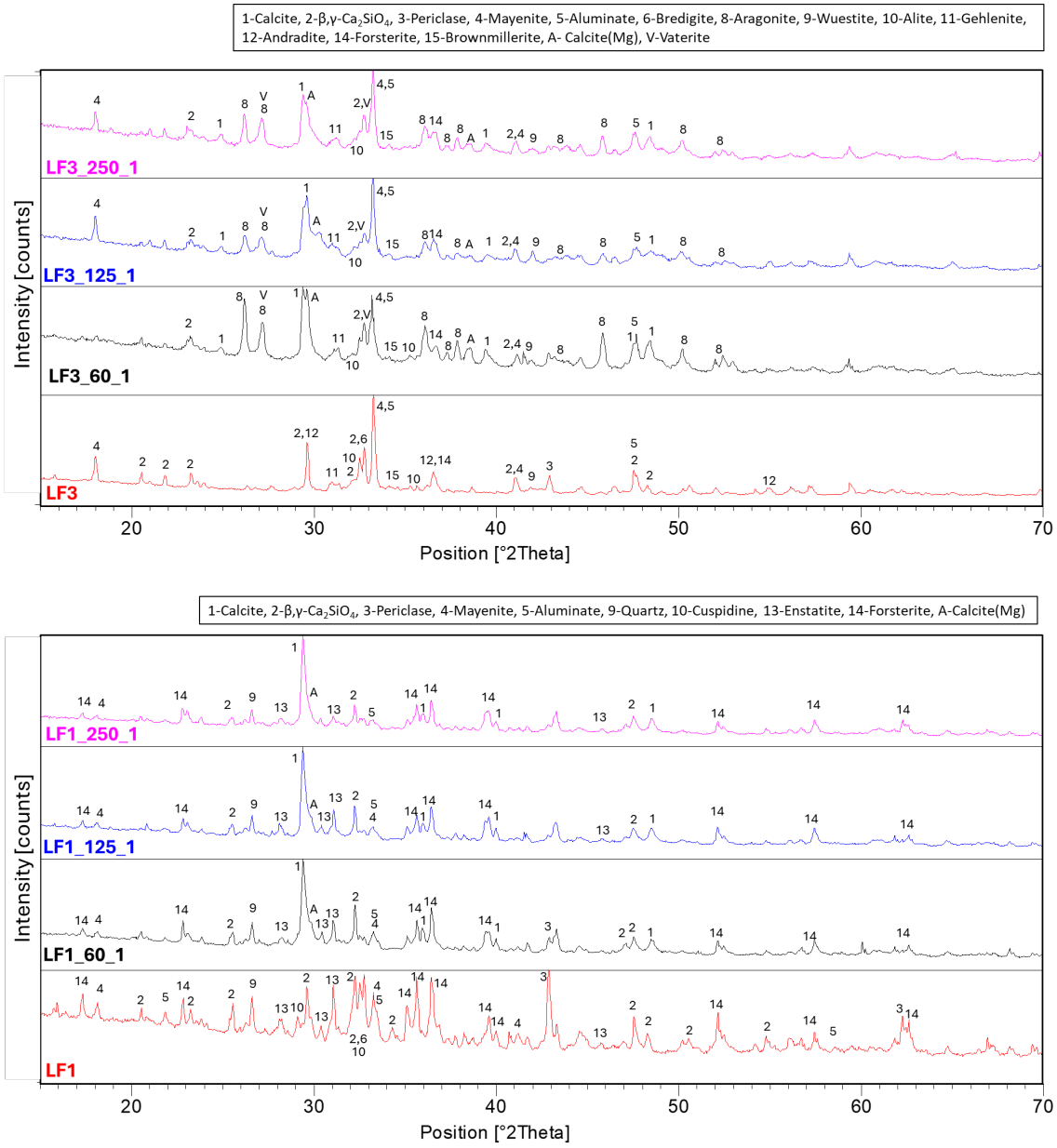

Figure 24. XRD pattern of carbonated products of LF3 and LF1 (test 1) at different stirring speed (60, 125 and 250 rpm). The carbonation test was conducted at room temperature, 15 bar and L/S = 1.5. All the mineralogical phases were numbered. The graphs underline the difference in carbonation results between the two slags. In LF3 vaterite, aragonite, calcite and calcite-Mg were formed, whereas the last two phases are the only carbonated products for LF1

SEM images are collected in **Figure 25** and **Figure 26** for LF3 and in **Figure A- 12** and **Figure A- 13** for LF1. They provide further insights into the morphology of the samples before and after the carbonation process. In **Figure 25** the elements as Ca, Al, Mg, Si and Fe are randomly distributed within the microstructures as we expected, and the dimensions of the particles is different due to the grinding process. **Figure 25C** confirms the presence of calcium silicates (the green-blue crystal) but also the presence of aluminium silicates on which periclase crystals have grown. Moreover, the blue is the main colour underlying that calcium is the main element as demonstrated by chemical analysis (**Table 6**). For LF1 the random distribution is also confirmed by SEM (in **Figure A- 12**) but the main elements present are Si and Ca (29 % and 25 % by XRF analysis collected in **Table 6**).

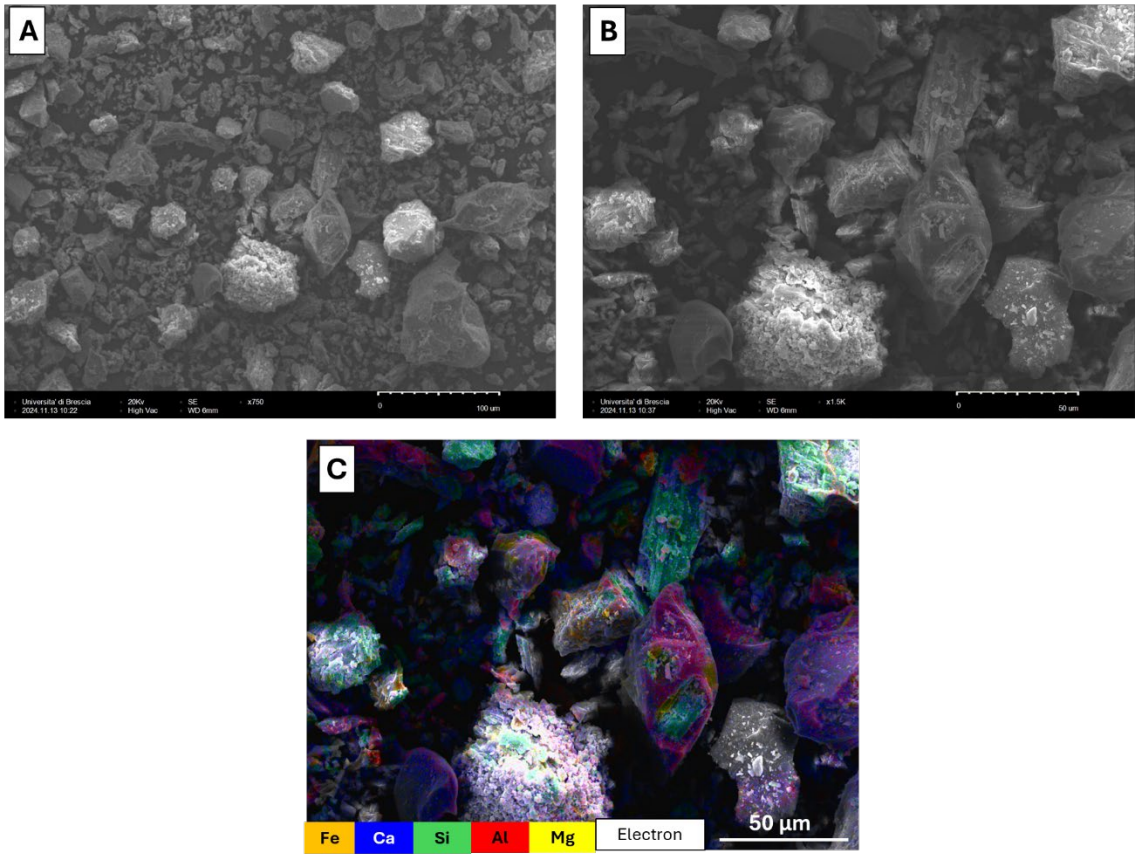

Figure 25. SEM images of starting material LF3 at different blows-up (A-B). Backscatter electron images of LF3 (C) plotted with the corresponding element concentration maps. In the composite maps, the saturation of each colour doesn't correspond to the concentration of the elements

Regarding the carbonated products, samples at 60 and 250 rpm are analysed to determine the influence of stirring speed on the morphology. **Figure 26** compares carbonated LF3 at 60 and 250 rpm. It seems that when the speed increases the product morphology changes from rectangular/hexagonal crystal with big dimensions to spindle-shape $CaCO_3$ crystals. When the stirring speed enhances, sheer forces generated by the stirring process increase driving the crystallization nuclei across the potential barrier and resulting in the coagulation of nucleation centres. Consequently, the nucleation rate enhances, and the particle size decreases [101]. For LF1 same results are presented in **Figure A- 13** despite the LF1 is different than LF3 in terms of chemical and mineralogical composition.

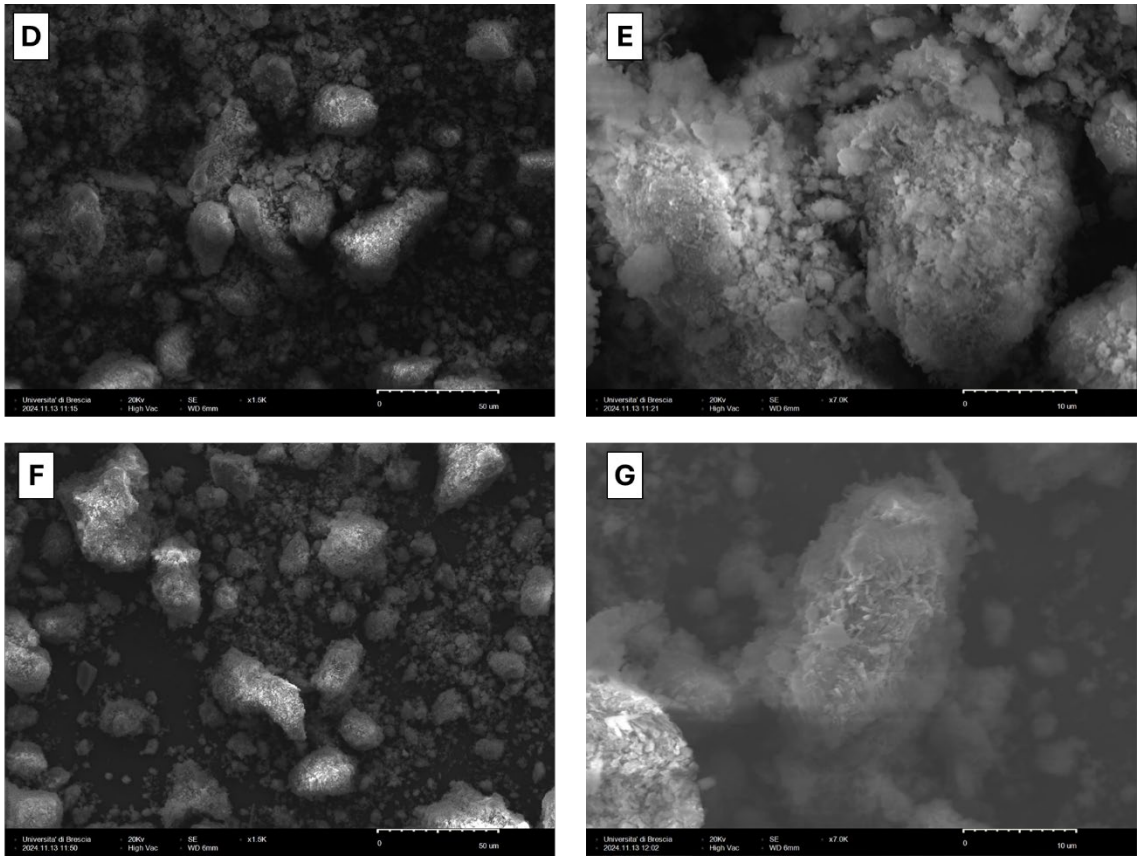

Figure 26. SEM images of carbonated products: LF3_60_1 at different zooming (D-E) and LF3_250_1 at different zooming (F-G). The images underline some changes in the morphology of the samples by using different stirring speed

The CO_2 uptake is calculated based on the **Equation 13** and **14** in **Section 3.4.1** and the average data are reported in **Figure 27.** The results for test1 and test2 are reported in **Figure A- 14**. In the graph, the results related to perfect gas law calculations are two: the first is CO_2 injected in the reactor and that potentially can react, the second is the difference between the total CO_2 injected and the CO_2 adsorbed by the water in the blank samples and it is around 2 g independent of the stirring speed. This aspect is correlated to the fact that not all the CO_2 inserted in the reactor can react with the material. In fact, subtracting the final mass (m_f) with initial mass of the slag (30 g) and comparing with the CO_2 injected mass, reported in **Table 17**, if for LF3 the these values are similar, for LF1 they are different due to lower reactivity of this byproduct that is also confirmed in mild condition experiment in **Section 4.5.1.** Moreover, the Rietveld method shows the lowest CO_2 uptake and the highest standard deviation. On one hand, Rietveld refinement quantifies only the crystalline phases and does not account for calcite formed within the amorphous fraction. On the other hand, the high variability may be attributed to the complex mineralogical composition and the possibility of selecting a reference phase from the database that does not perfectly match the synthesized crystalline phase. This mismatch can negatively affect the pattern fitting performed by the Profex software. An example of fitting is reported in **Figure A- 15**. Moreover, the thin-film route doesn't facilitate the dissolution of powder and, probably, low stirring speed as 60 rpm don't favour a homogenization of the sample. It can cause a different reactivity of the slag under the same condition. To make the reproducibility better, the number of repetitions need to be increased avoiding too low stirring speed values and increasing the liquid to solid ratio in the range of 5-10 ml/g.

The obtained results are in line with literature data (250 g CO_2/kg of slag) [53,97,98]. In conclusion, in these condition the stirring speed influences mainly the kinetic mechanism, in particular the rate of pressure, in the first hours but not the carbonation performances as demonstrated in some studies in literature [101,102] Moreover, this experiments at high pressure are included in a preliminary study and the process needs to be optimized by change the liquid to solid ratio to increase the Ca ions solubility, increasing the temperature to verify its influence, changing the initial pressure of CO_2 and scaling up the process.

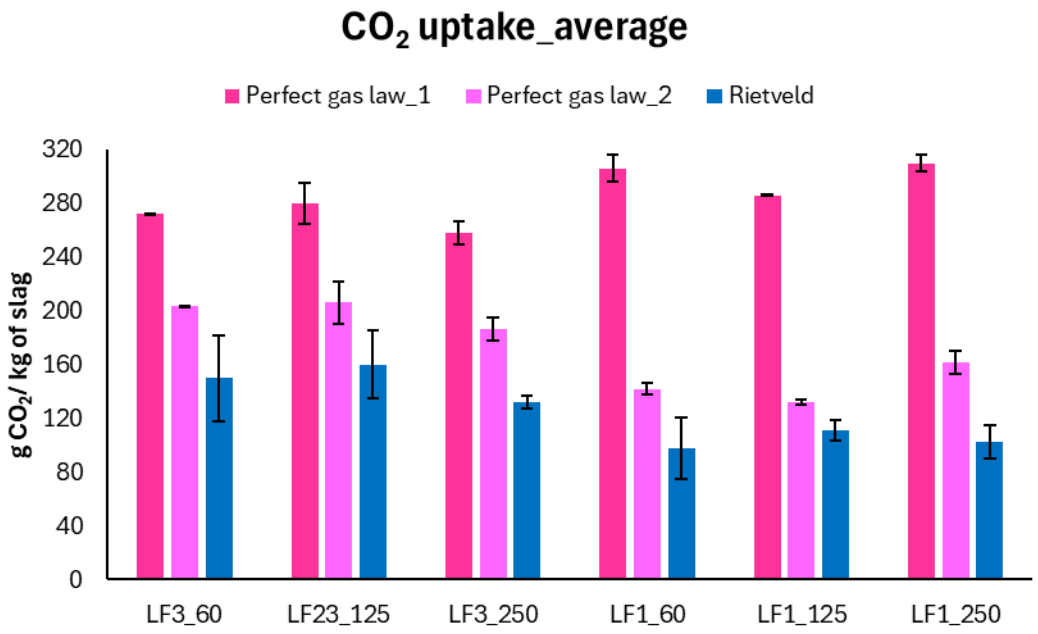

Figure 27. The values represent the average CO_2 uptake, with error bars indicating the standard deviation. Two approaches based on the perfect gas law were applied: Gas Law 1 does not consider CO_2 absorption by water (as measured in the blank sample), whereas Gas Law 2 includes this correction, resulting in a more accurate estimation of the CO_2 uptake by the slag.

4.4 Mild condition environmental carbonation

4.4.1 Characterization of steel slag

As the **Figure 17** described, there is no difference in the chemical composition after the iron separation excluded for iron part and the same consideration is valid for mineralogical composition as shown in **Figure 28**.

Based on the XRD data reported in **Figure 28** and in **Table A- 4/10**, steel slags have similar phases as belite (β-C_2S and γ-C_2S), periclase (MgO) and mayenite ($Ca_{12}Al_{14}O_{32}$) and they can be divided in three groups. LF1-2 and AOD1 present higher percentage of aluminium that is part of phases as gehlenite ($Ca_2Al[AlSiO_7]$) and aluminate (C_3A), even if LF1 contains phases as forsterite and estantite due to higher content of Mg. EAF1-2 exhibit a higher concentration of iron which is mainly in wuestite (FeO) and brownmillerite ($Ca_2(FeAl)_2O_5$). At least, in BF5 the amorphous structure is predominantly even if some crystalline phases as portlandite and lime are observed. The mineralogical composition of the steel slags is in line with literature data [7]. The XRD patterns are reported in **Figure A- 16** and show that the only difference after the Fe-removal process is the lack of iron-magnetic phases (magnetite, hematite) peaks.

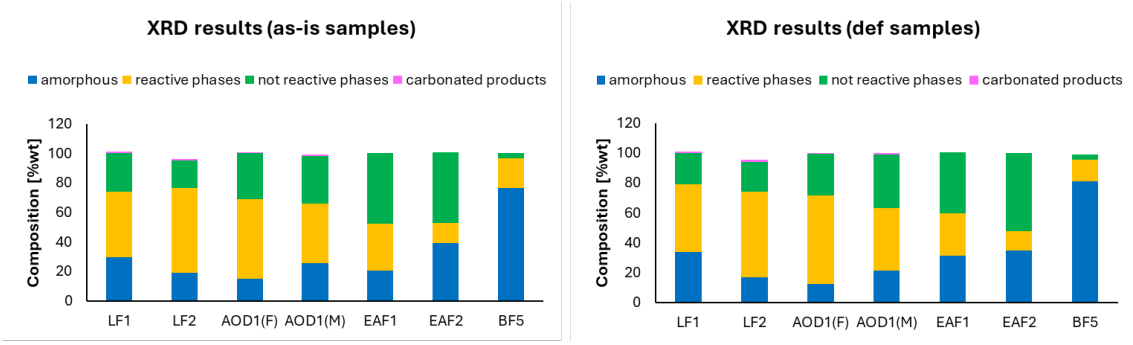

Figure 28. Quantitative phase analysis of untreated slag samples before and after dry iron removal process, obtained by Rietveld refinement. The graph illustrates the changes in mineralogical composition following the carbonation process.

4.4.2 Carbonation performance

The high-pressure reactor used "strong" conditions as 15 bar of pressure and these conditions may be not suitable for an industrial process. As discussed in the **Chapter 1.3**, the carbonation mimics the weathering of the rocks. Consequently, tests at mild conditions, like what happens in environment, were used, also to verify if steel slags are reactive in these conditions. Moreover, both untreated and Fe-removed samples were tested to evaluate if the iron separation can affect the carbonation process. Regarding the experimental process, the pH values are reported in **Figure 29**. The pH of starting materials is similar and close to 12 due to high content of basic oxides [98]. The trend of pH decreases over the course of the time reaching values about 8.5-10 due to the consumption of alkali oxides. The decrease is more evident in samples LF1, LF2 and BF5 (untreated and iron separated) because they also contain higher percentage of $CaCO_3$ than other tested samples as shown in **Figure 30** (the data were normalized subtracting the initial CO_2 mass). It is important to underline that the CO_2 sequestrated data are based on Rietveld calculation which considers only the crystalline part. Moreover, in Appendix (**Figure A- 16**) both starting materials are compared only with def carbonated product after 1 month because the differences between def and not def products after 2 months and 1 year are not distinguished in the figures.
The total CO_2 sequestered, considered also the amorphous content, was not determined. From a FT-IR point of view, the calcite formation is evident in the region of 800-1400 cm^{-1}, respectively 873 cm^{-1} and 1410 cm^{-1}. However, only in LF2 the silica gel, as secondary product, is detected around 1040 cm^{-1} but for the other samples (BF5, LF1 and AOD1(F)) this band is not identified. Consequently, belite band around 856 cm^{-1} remains in the carbonated product (**Figure A- 17**).

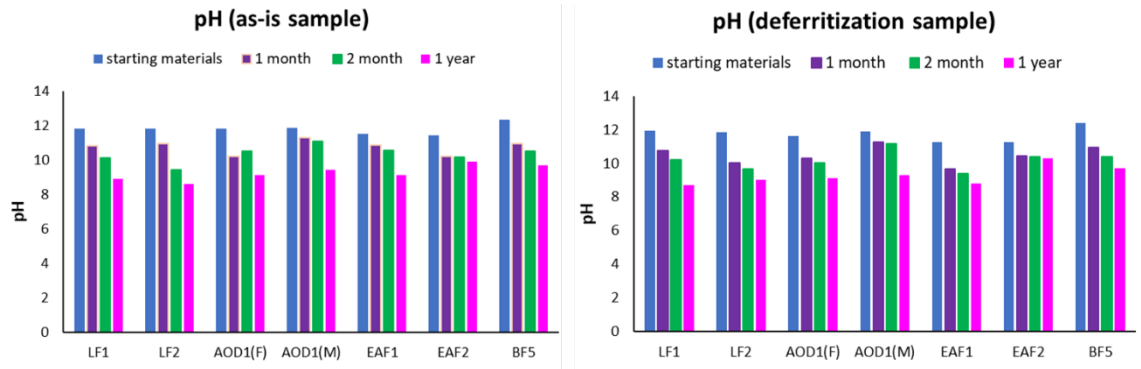

Figure 29. pH evolution in carbonation process, at 0, 1 and 2 months and 1 year for steel slag and steel slag after Fe-removal. The pH was measured dissolving the slag in Milli-Q water with a liquid-solid ratio about 10

Regarding the carbonation performances of selected materials, BF5 shows the best performances in both cases with a 175 g CO_2/kg of slag. This is due to highest concentration of CaO (**Table 6**) than other slags. Otherwise, from XRD analysis, it contains also the highest percentage of amorphous (about 89%), consequently, it is difficult to identify the mineralogical phases. Based on XRD pattern (in **Figure 31**), lime and portlandite were identified, which are reactive species in the considered process. Moreover, the amorphous content decreases during the reaction time because crystalline phases were formed as calcite and aragonite.

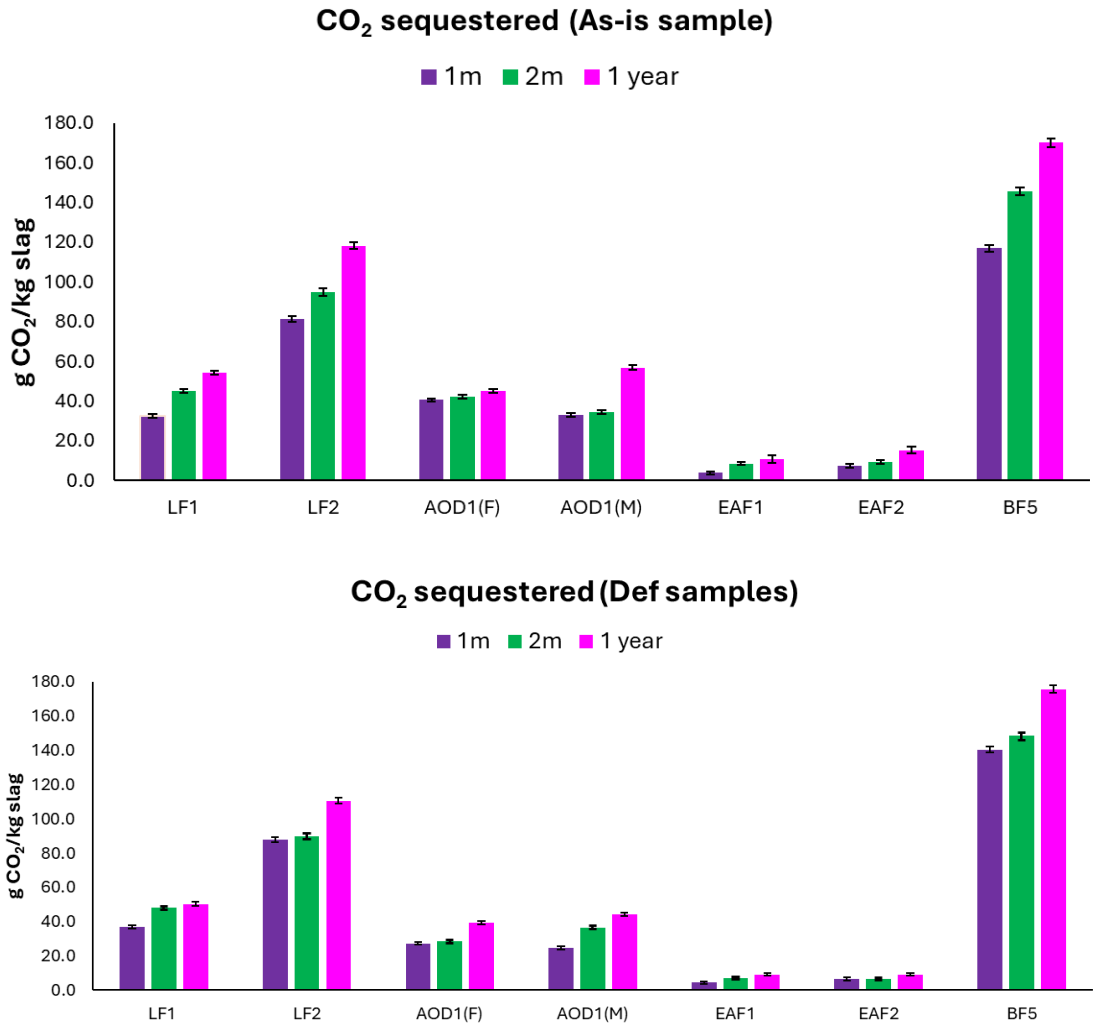

Figure 30. Comparison of captured CO_2, calculated by Rietveld quantification and expressed in g CO_2/kg slag at 1 and 2 month and 1 year for untreated and Fe-removed steel slag. The error was calculated by Equation 15 and 18

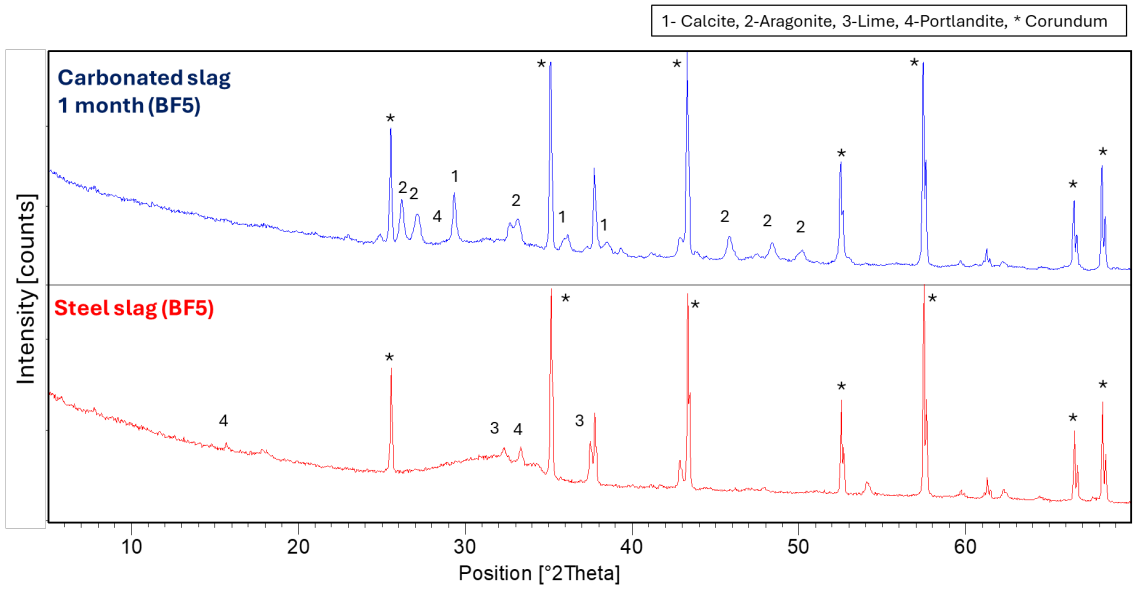

Figure 31. Comparison of XRD pattern of def BF5 slag at the start and after 1 month of natural carbonation. The pattern includes alumina peaks (used as internal std)

Concerning the other slags, LF2 can sequestrate around 81-87 g of CO_2/kg of slag considering both samples, whereas the worst materials are EAF1 and EAF2 due to the lowest content of CaO (**Table 6**) the presence of low quantity of reactive species (only belite and mayenite) and the Fe content which can interfere in the carbonation process. In fact, working in an oxidative environment (as in this case), Fe-phases are oxidized in hematite which obstructs the CO_2-slurry interaction by the formation of a surface layer [66]. Moreover, for all the samples the amorphous content increases (**Figure 32**) during the reaction period and this is correlated with the formation of $CaCO_3$ and SiO_2 gel amorphous [58,106]. Another aspect to underline is the formation of calcite and their polymorphs aragonite and vaterite especially for LF and AOD slags. In the thesis, only data related to 1 month were reported because the changes are more evident respect to 2 month and 1 year. To a complete comprehension, Rietveld results at 1 year are reported in **Figure A- 18**.

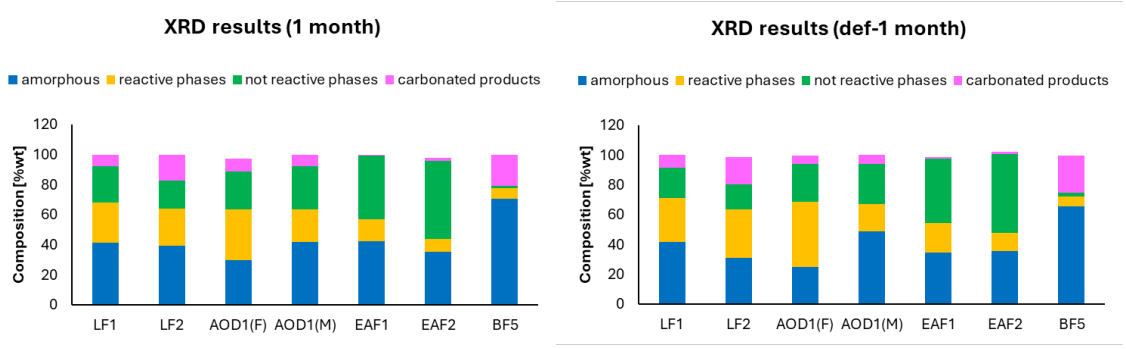

Figure 32. Quantitative phase analysis of carbonated slag (untreated and iron-removed) samples obtained by Rietveld refinement. The graph illustrates not main differences in mineralogical composition despite of the dry Fe removal process

4.5 Enforced carbonation

In this Chapter, only iron removed samples were used to study their performance in enforced carbonation at room temperature and pressure. The data regarding the chemical and mineralogical composition are reported in **Table 6** and **Table 7.**

Part of the results are contained in the paper "Evaluation of steel slags in CO_2 sequestration and as Supplementary Cementitious Material", submitted to Construction and Building Materials on 17th of November 2024.

During the entire reaction period, the pH was measured for each sample. Initially, the pH of solution was around 5-6 because the NaOH solution reached an equilibrium with CO_2 gas. By the addition of slag into solution, the pH increased around 10-13 due to different solubility and alkaline concentration of the byproduct. After 30 minutes, the system reached an equilibrium state, and the pH was closed to neutral values (in **Figure A- 21**). The carbonated samples were analysed by TG, XRD and FT-IR to quantify the carbonation degree and study the resulting phase assemblage. TG data are collected in **Table 18** and show the formation of calcite in all the samples. cLF2, cAOD1 and cSlag8 show the highest calcite content and, consequently, the CO_2 captured because they exhibit the largest content of reactive species as show in (46 %, 50 %, and 43% respectively) despite these components are not completely reacted [105] as demonstrated in **Figure 33** and in **Table A- 11.**

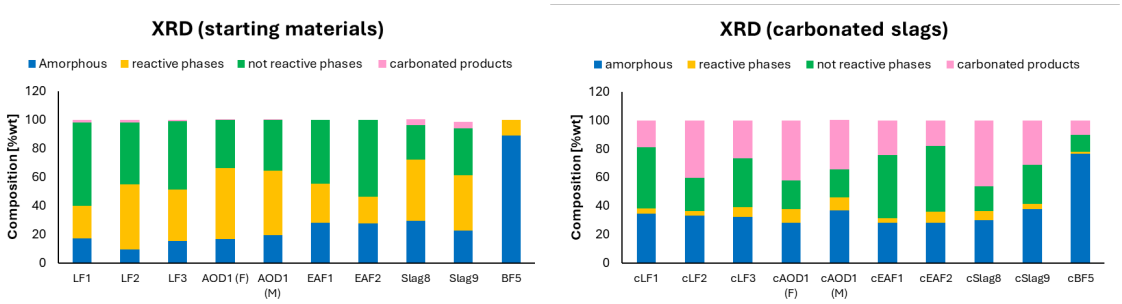

Figure 33. Quantitative phase analysis of untreated and carbonated slag samples obtained by Rietveld refinement. The graph illustrates the changes in mineralogical composition following the carbonation process

The TGA analysis of the carbonated materials is shown in **Figure 34**. The thermogravimetric curves mainly highlight changes occurring between 400 and 800°C, which are associated with the decomposition of calcium carbonate. Since 500°C poorly crystallized calcium carbonate decomposes [107,108]. Notably, the most pronounced weight loss is observed in the 700–800°C range, indicating that the predominant crystalline phase of calcium carbonate forms during the wet carbonation process.

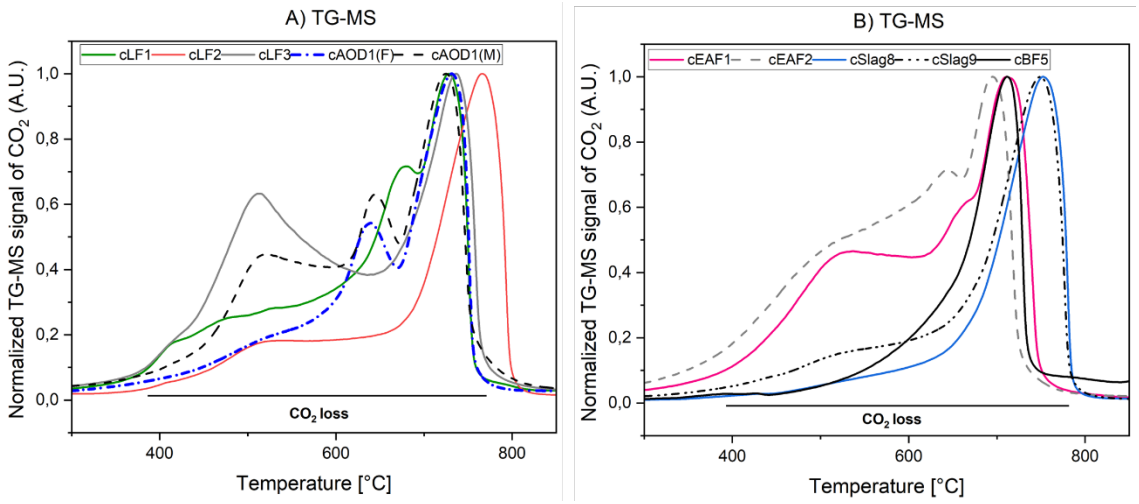

Figure 34. TG-MS data about the CO_2 loss of carbonated slags in the temperature range 300-850°C. The slags are divided in two groups for a better understanding. The CO_2 loss is underlined with a black line (400-850°C). The difference shape in TG curve may be due to formation of poor crystalline carbonated product and different carbonated product

The carbonation degree is calculated considering only CaO content and then both, Mg and Ca oxides because it has been verified that Mg may be involved in the reaction with CO_2 forming Mg-doped calcite, but the mechanism and the role of this element are still studying [109]. The Carb Degr 1 is calculated through the theoretical CO_2 mol if CaO reacts completely, the second one consider also the total reactivity of Mg. The sum of MgO and CaO content decreases the second carbonation degree value because the denominator is higher than only CaO is considered. For LF1 the parameter diminishes about half of the Carb Degr 1 because the MgO is higher than in other samples (19.4 %). Additionally, the carbonation degree confirms that some Ca and Mg phases are not reactive in this process.

Table 18. TG data normalized by LOI and carbonation degree. The carbonation degree (Carb Degr 1) is correlated with the theoretical mol of CO_2 considering a complete CaO reaction; the second one (Carb Degr 2) also accounts for the complete reaction of MgO

Samples	$CaCO_3$ (TG data) [g/100g]	CO_2 sequestered [g/kg of slag]	Carb Degr 1 (CaO) [% wt]	Carb Degr 2 (CaO+MgO) [% wt]
cLF1	40.8	16.8	80.4	39.2
cLF2	58.1	24.6	71.2	55.9
cLF3	43.0	18.5	53.8	41.8
cAOD1(F)	51.8	22.5	60.1	47.7
cAOD1(M)	50.1	21.2	60.8	44.0
cEAF1	24.0	10.4	72.5	53.8
cEAF2	19.1	8.2	60.2	44.6
cSlag8	62.7	26.3	68.7	50.2
cSlag9	45.9	20.2	64.5	40.8
cBF5	16.7	7.0	16.8	13.7

BF5 shows the low calcite content probably due to high amorphous content (89 %) which affects negatively the reactivity of the slag [105,110]. Due to low performance in the process, in FT-IR analysis the band related to Si-gel around 1040 cm^{-1} was not identified (**Figure A- 20H**). However, the slag can be activated by the hydration in NaOH solution overnight before adding CO_2 as shown in **Figure 35**. In fact, the carbonate TG data increases to 55 % and the main products are calcite and aragonite.

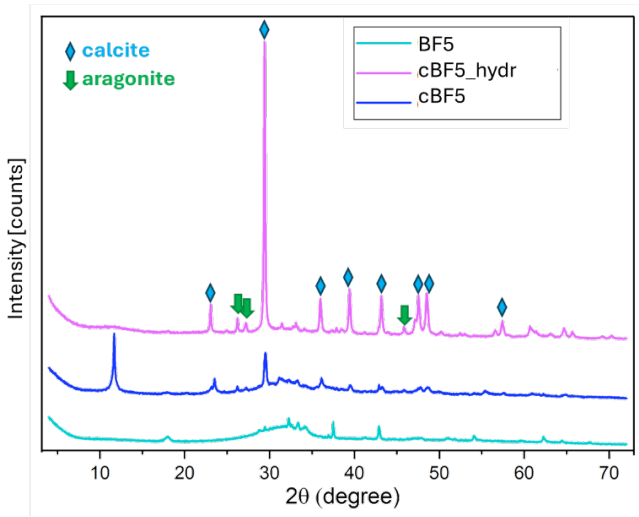

Figure 35. Comparison of XRD pattern of starting material (BF5), carbonated byproduct (cBF5) and carbonated slag after hydration process overnight (cBF5_hydr) underling the mineralogical peaks differences. When the slag is hydrated overnight the reactivity enhances, more CO_2 is sequestered, and the formation of carbonated phases is evident and, consequently, the amorphous content decreases.

The mineralogical composition of carbonated steel slag is reported in **Figure 36, Figure A- 19** and summarized in Table A- 11. As demonstrated, the percentage of reactive phases (*f*-CaO, C_2S, portlandite and periclase) decreased with the carbonation process and, as a result of carbonation, calcite, main product, aragonite and calcite (Mg) were formed, as shown in **Figure 33**. Simultaneously, an hydration reaction takes place, leading to the formation of calcium silicate hydrate (C-S-H) gel, calcium hydroxide ($Ca(OH)_2$), and magnesium hydroxide ($Mg(OH)_2$). However, these products do not persist during the carbonation phase; instead, they immediately engage in further chemical reactions within the studied process. The calcium and magnesium hydroxides undergo direct interaction with carbonate ions (CO_3^{2-}), resulting in the formation of the corresponding carbonates, which are precipitated on the surface of the steel slag particles. Concurrently, the C-S-H gel undergoes a continuous decalcification process, in which calcium ions are leached out, leading to the progressive polymerization of silicon-oxygen (Si-O) tetrahedra. This results in the formation of silica compound, a more stable phase that contributes to the material's overall structural integrity. The continuous transformation of these phases during carbonation not only alters the microstructure but also enhances the material's durability and mechanical properties, making it more suitable for applications in construction and other engineering fields [111]. The Si product has not been detected by XRD, consequently it contributes to the increase of amorphous content [59,103,104].

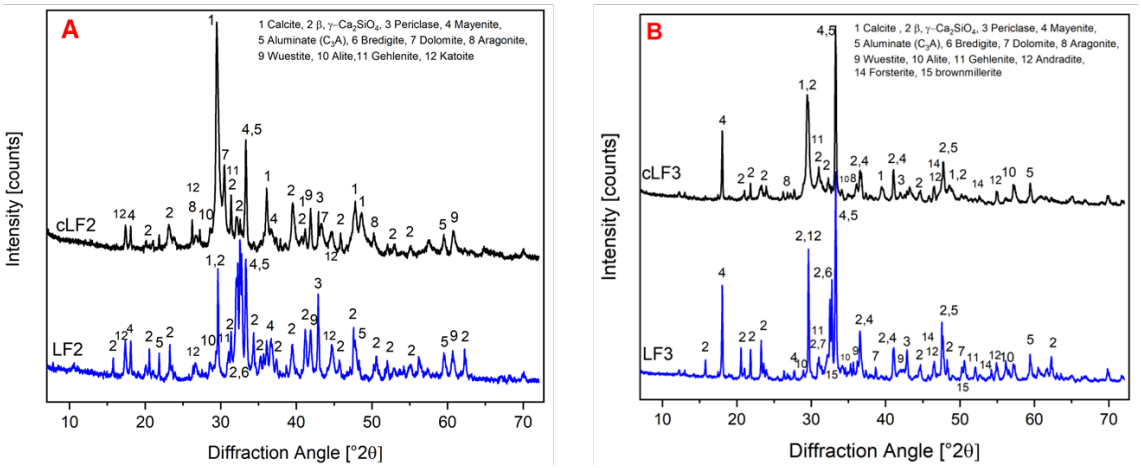

Figure 36. Comparison of XRD pattern of LF2 and LF3 before and after carbonation (cLF2 and cLF3), highlighting the phase transformations and mineralogical changes induced by the carbonation process. The mineralogical phases are reported in the figure, and they are numbered

This evidence is demonstrated by FT-IR spectra reported in **Figure 37**. In the Si-O vibration region, 800-1200 cm^{-1}, the starting material shows a band at 848 cm^{-1}, associated with silica stretching in belite [112,113], whereas in the region 800-400 cm^{-1}, the band at 497 cm^{-1} is related to the bending of Si-Al bond [114]. However, in the carbonated slag, it is shifted to 1040 cm^{-1} indicating the decalcification of the calcium silicates and the formation of silica product. Furthermore, the **Figure 37** underlines the formation of calcium carbonate as calcite in the carbonated materials as evidenced in the bands 713 cm^{-1}, 875 cm^{-1} and 1412 cm^{-1} corresponding to vibration C-O bond. FT-IR spectra of other analysed samples are in **Figure A- 20** and same consideration can be done. EAF1 and EAF2 shows in the carbonated spectra bands correlated with Si-bond of belite, meaning that uncompleted reactivity of this phase (**Figure A- 20**).

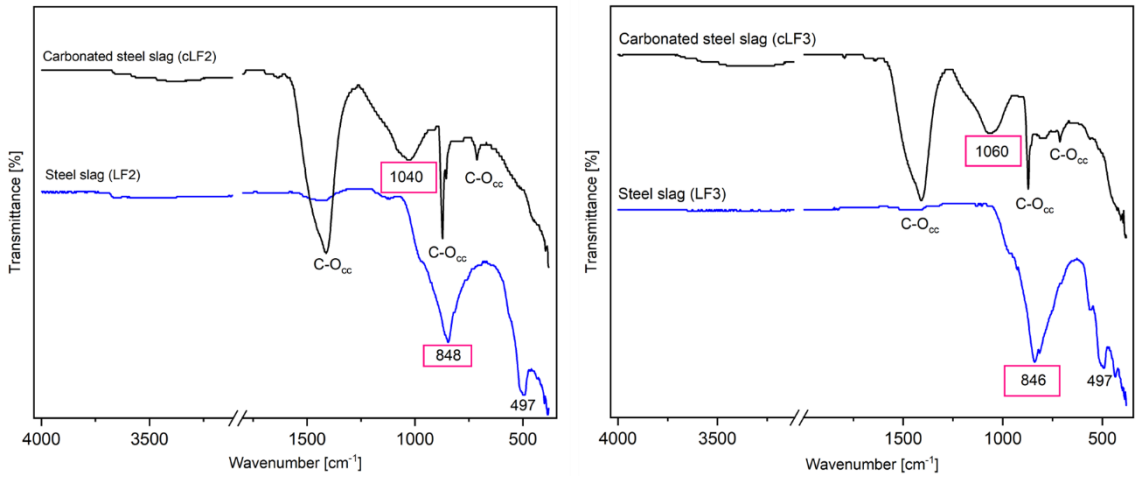

Figure 37. Comparison of FT-IR analysis of LF2 and LF3 before (blue line) and after carbonation (cLF2 and cLF3), highlighting the formation of carbonate bond and silica-gel.

SEM analysis, reported in **Figure 38**, provides further insights into the carbonation products, revealing elements such as Ca, Si, Mg, and Al randomly distributed within the microstructure, as we expected. Additionally, within the highlighted red rectangle, the green area denotes the formation of silica product encased by a “white outline” representing calcium carbonate. Another observation is the alteration of the material's surface. In the untreated sample, the particles exhibit a smooth and dense structure; while following carbonation, the particles are enveloped by porous products, as illustrated in **Figure 38**.

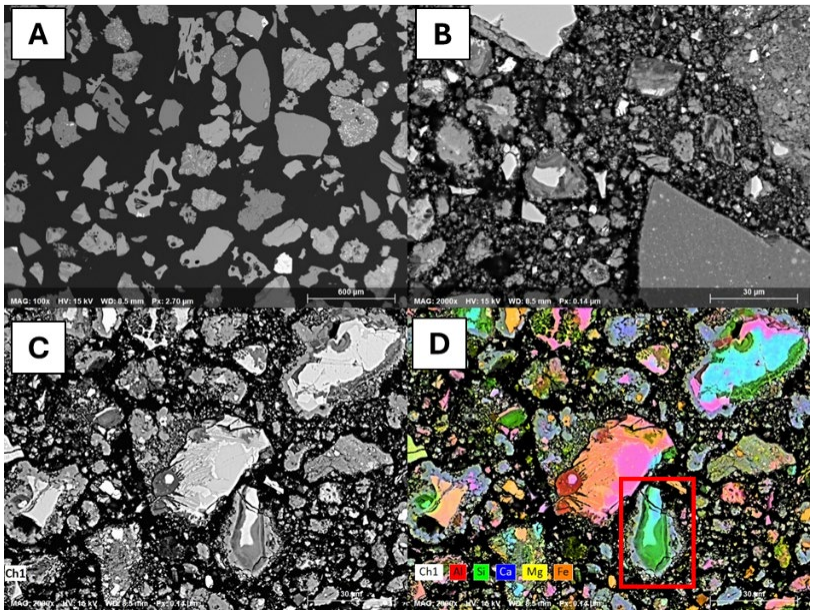

Figure 38. SEM images of starting material LF2 (A) and carbonated slag cLF2 (B). Backscatter electron images of carbonated slag (C-D) plotted with the corresponding element concentration maps for the carbonated slag. In the composite maps, the saturation of each colour doesn’t correspond to the concentration of the element

4.6 Cement performance

To investigate the behaviour of composite cements where 40 % of cement was replaced by steel slag (untreated and carbonated), calorimetry study, hydration study and compressive strength were executed. The calorimetry study was conducted for all the samples by a first comparison

between the untreated slag-mix (CEM-Sx) and carbonated slag-mix (CEM-Cx). These preliminary results demonstrated each slag has a different behaviour in cement. Consequently, several tests with different accelerators and ratio were done to optimize the formulation and study the effect of slag in the composite cement. In the thesis, only the main results were reported and discussed and only five samples were chosen for a complete study in cement performance based on kinetics results, carbonation performance and iron content. The selected samples are LF1, LF2, LF3, Slag8 and Slag9.

Calorimetry Study

The calorimetry study was executed for all the samples using starting material and carbonated slag to study the hydration kinetics of composite cement mixes. Calorimetry test results of composite cements (w/c = 0.5, 60% CEM, 40% slag/limestone and additives). The kinetic of the hydration cement reaction was compared between the reference mixes (CEM and CEM-L), shown in **Figure 39A**, and the slag mixes, underlining the necessity to optimize the composite cements by the addition of accelerators. Both references are used to examine how incorporating slag can affect the reactivity of cement clinker and whether it can enhance mechanical performance compared to an inert phase. When cement is replaced by limestone, the heat flow decreases due to a lower percentage of alite (C_3S) and ettringite (C_3A), which are primarily responsible for early-stage cement hydration [115]. Steel slags have been observed to affect the reaction kinetics of cement clinker by delaying the induction period, depending on the material studied. In this study, two distinct behaviours were noted, as shown in **Figure 39**. In the analysed samples, adding carbonated steel slag resulted in a different behaviour than when non-carbonated slags were introduced to the cement. Steel slag has a lower sulphate content than Portland cement (2.6-3.6%) [54,116], as shown in **Table 6**. In undersulphated systems, the initial ettringite (C_3A) reaction precedes that of alite (C_3S), negatively affecting setting and hardening [54]. In CEM-S1, an unusual evolution of alite and ettringite peaks was observed, while the incorporation of cLF1 (CEM-C1) extends the induction period (first 3 hours), possibly due to the formation of lower amounts of C-S-H [54], although reactivity seems to approach that of cement. Moreover, cLF1 has a low content of calcite than other tested samples (40.8 g) and the hydration reaction of alkaline phases is dominant [58]. The combination of three different "accelerators" balances the sulphate content (CEM-C1_1%) and reduces the induction period (**Figure 39B**). Additionally, the presence of an unexpectedly high MgO content (about 20%) may influence the system's reactivity. In CEM-C2, there isn't a delay in reactivity, but the sulphate content needs to be adjusted by adding hemihydrate (**Figure 39C**) to separate the alite and ettringite peaks (CEM-C2_1.5%). In LF3 graph, the raw material (CEM-S3) shows a high intensity peak which the heat, released by the hydration, decreases by carbonation process (**Figure 39D**). At least, CEM-S8 shows the most similar kinetic because it contains portlandite (as shown in **Figure A- 19H**) which simulates in a better way the composition of cement (**Figure 39E**). The kinetic study for slag BF5, EAF1-2 and AOD1(F) are reported in **Figure A- 22**, whereas for Slag9 the calorimetry tests were not executed because the mineralogical composition is like Slag8 (as shown in **Figure A- 19H-I**). AOD1 (F) was excluded because an optimization of the mixes proportion was difficult whereas EAF slags were not considered due to high iron content which can be oxidised by air contact and to hardness of material.

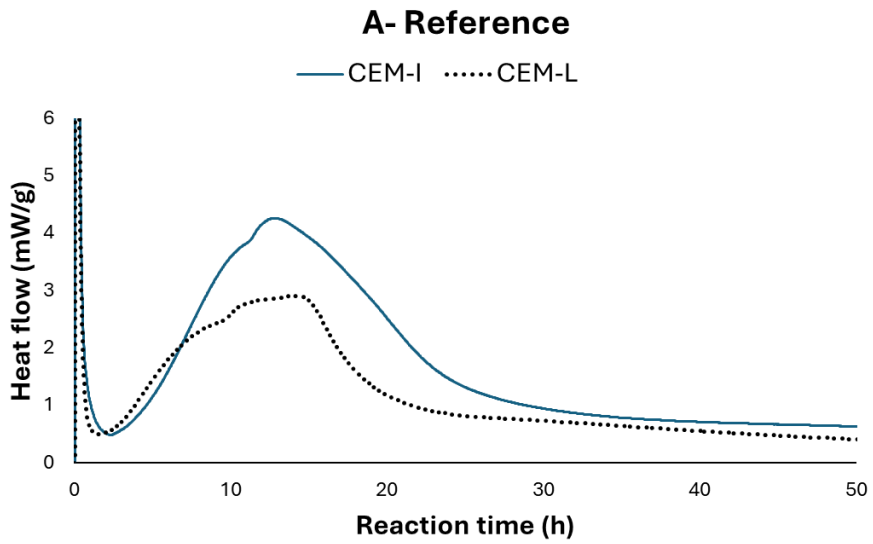
A- Reference
CEM-I
CEM-L
Heat flow (mW/g)
Reaction time (h)
0
1
2
3
4
5
6
0
10
20
30
40
50

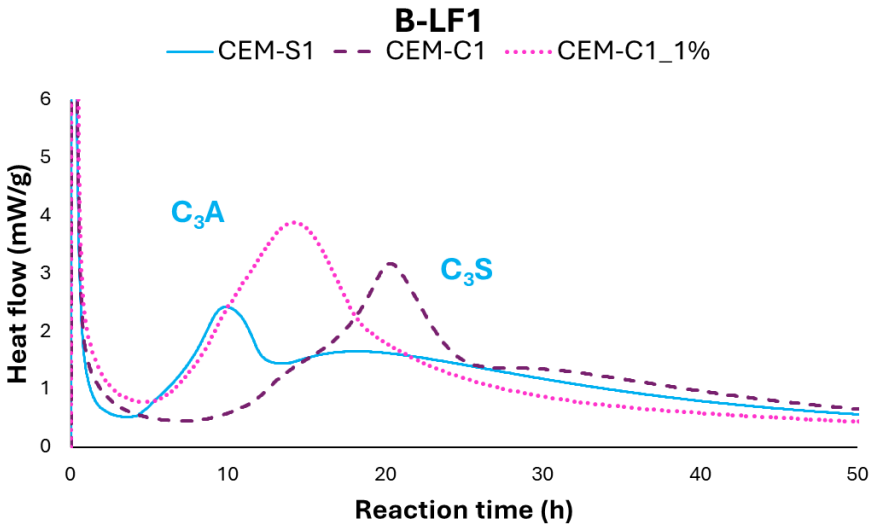
B-LF1
CEM-S1
CEM-C1
CEM-C1_1%
C3A
C3S
Heat flow (mW/g)
Reaction time (h)
0
1
2
3
4
5
6
0
10
20
30
40
50

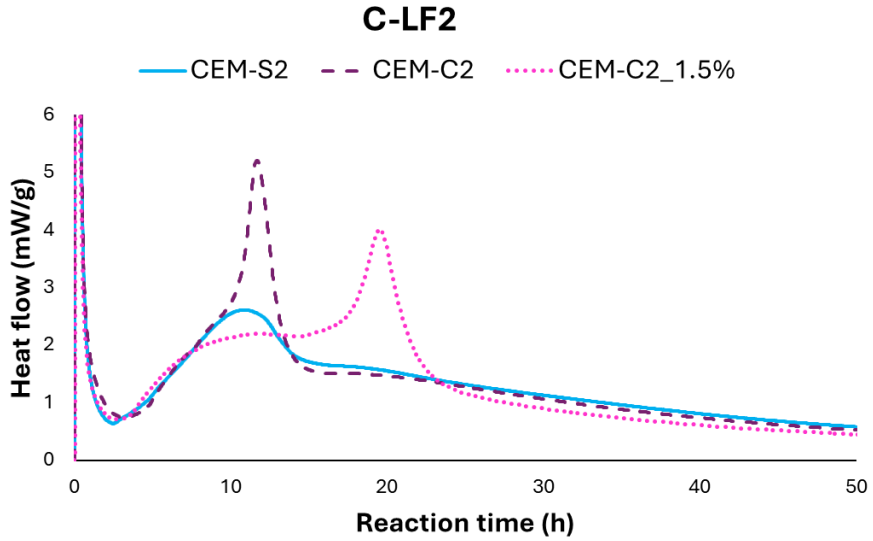
C-LF2
CEM-S2
CEM-C2
CEM-C2_1.5%
Heat flow (mW/g)
Reaction time (h)
0
1
2
3
4
5
6
0
10
20
30
40
50

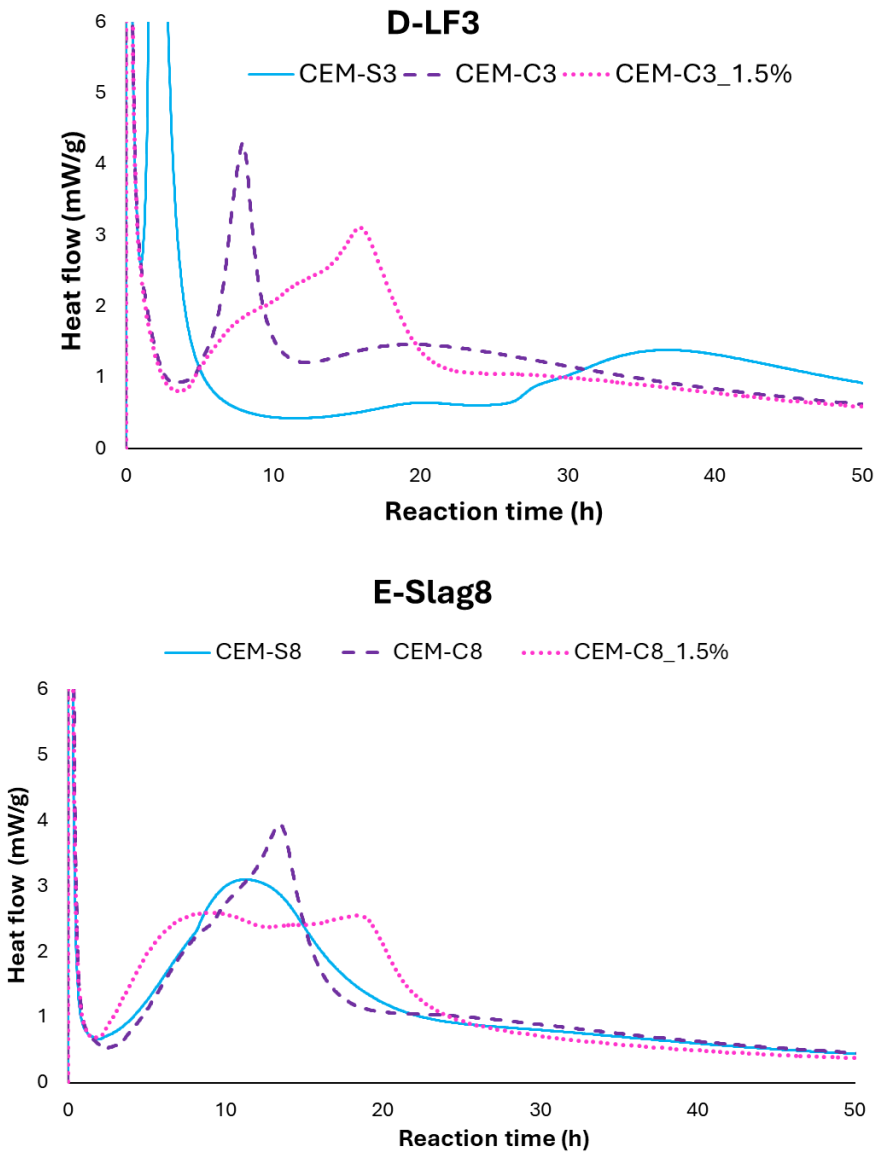

Figure 39. Calorimetry tests results of composite cements (w/c = 0.5, 60% CEM, 40% slag/limestone and additives). The kinetic of hydration cement reaction is compared between the reference mixes (CEM and CEM-L) and the slag mixes underling the necessity to optimize the composite cements by the addition of accelerators. Reference, LF1, LF2, LF3 and Slag8 mixes are reported respectively in figure A, B, C, D and E

While our study confirms that carbonation enhances the pozzolanic activity of steel slag, it also aligns with previous findings that carbonation alone does not result in optimal composite cement performance. As reported in Srivastava et al. [103] the degree of carbonation significantly affects the reactivity of steel slags as SCMs, with excessive carbonation potentially leading to passivation of reactive sites and reduced cementitious performance. To address this challenge, researchers have suggested the incorporation of chemical activators such as calcium sulphate and hydration accelerators, which have been shown to counteract the potential strength reduction due to carbonation-induced mineral transformations [117].

Pozzolanic activity

To assess the potential benefits of the carbonation process, the analysis of the pozzolanic reactivity of steel slags is necessary. For this purpose, hydration mixtures (blends with portlandite) were employed [118]. This hydration test replicates the pozzolanic reaction that occurs in composite cements, where portlandite interacts with semi-hydraulic or siliceous pozzolanic materials, forming hydrates like C-S-H and AFm phases if Al-Si gel is also present. Experimental results, presented in **Figure 40**, illustrate portlandite consumption and bound water content, which is directly linked to the amount of reacted silica gel [118,119]. In the untreated materials, no portlandite consumption is observed (as shown in **Figure 40A**), as belite reacts with water to produce both portlandite and C-S-H, as explained in the **Equation 20:**

$$C_2S_{slag} + H_2O \rightarrow CH + C\text{-}S\text{-}H \quad (20)$$

Figure 40C confirms the hydration mechanism, indicating a steady increase in bound water content up to 28 days. After 90 days the bound water content increases for Slag 8 and 9 whereas it stays stable for the other three samples. This increase is correlated with the increase of portlandite after 90 days (**Figure 40A**). FT-IR analysis reveals the formation of C-S-H at around 950 cm^{-1}, attributed to Si-O-Si vibrations. In the OH region, bands at 3636 cm^{-1} and 3539 cm^{-1} are linked to the O-H stretching vibrations from portlandite and hydration water, respectively [120,121] (see **Figure 41A,C**). Slag8 and 9 exhibit higher portlandite levels due to its presence in the initial materials (in **Figure A- 19H, I**).

Carbonated slags show rapid portlandite consumption within the first 7 days, with minimal reaction progress beyond 90 days (see **Figure 40B**). This effect is most notable in cLF2 and cLF3, which have a high calcite content as shown in **Table 18**, but also cLF1 with lower calcite content reaches similar levels. The rapid consumption of CH content in carbonated slag mixes is due to the cooperation between carbonated slag and portlandite (one of the main phases of Portland cement) in providing nucleation sites for the formation of C-S-H gel in the hydration process, as shown in Equation 4 [60]. The reduction in CH content results from the pozzolanic reaction between the Si-gel and CH in water, forming C-S-H gel, as shown in **Equation 21**:

$$(Si\text{-}gel)_{cslag} + CH + H \rightarrow C\text{-}S\text{-}H \quad (21)$$

where Si-gel is the silica product after carbonation, C-S-H is calcium silicate hydrates phase, CH is portlandite, and H is water

This evidence is also confirmed by the bound water (BW) content in carbonated slag, which simultaneously enhances when the portlandite content decreases. In fact, the highest BW values correspond to MIX-C3, which also has the highest CH decrease. MIX-C8 and C9 show the lowest bound water content as CH consumption. Otherwise, comparing graphs in **Figure 40C-D,** the carbonation process influences the consumption of portlandite in favour of C-S-H formation underlying the change of activity from hydraulic to pozzolanic in slags [104,122]. Moreover, the results reported in this manuscript are also confirmed by studies about Si-NMR data of carbonated steel slag before and after carbonation. They have demonstrated the decrease of amorphous SiO_2 after hydration, while the content of [SiO_4] related to C-S-H gel structures increases [111,118,123] This result confirms the Si-gel is involved in pozzolanic reactions to form C-S-H gel by the consumption of portlandite, present in Portland cement.

During hydration, Ca ions migrate into the Si-gel product, shifting the vibration band from 1040 cm^{-1} to 950 cm^{-1}, characteristic of C-S-H (**Figure 41B,D**) [59,104]. In carbonated slags, bound water

(BW) content aligns with CH consumption patterns, as reported in **Figure 40D**. MIX-C3, with the highest CH reduction, also exhibits the highest BW values, while Mix-C8 and C9 show the lowest BW levels corresponding to lower CH consumption. Comparing **Figure 40**, carbonation effectively enhances portlandite consumption, favouring C-S-H formation and highlighting a shift from hydraulic to pozzolanic activity in slags [124,125].

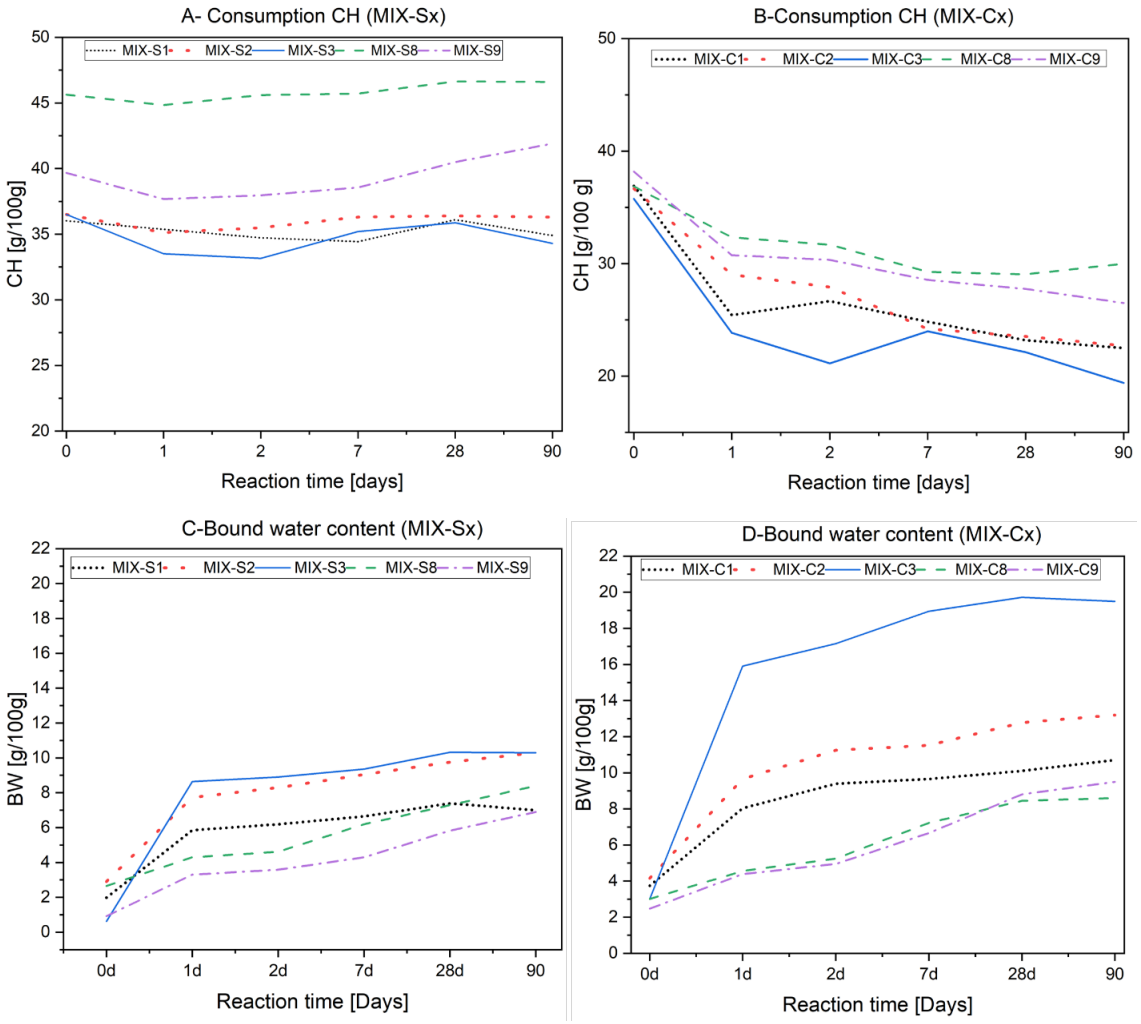

Figure 40. Portlandite consumption for starting materials (A) and carbonated products (B) mixes, underling the different reactivity of these two systems in term of pozzolanic reactivity. Bound water data for starting materials (C) and carbonated slag (D) mixes strengthen the high hydration in carbonated mixes. The shown data were collected by TGA analysis from 0 to 90 days

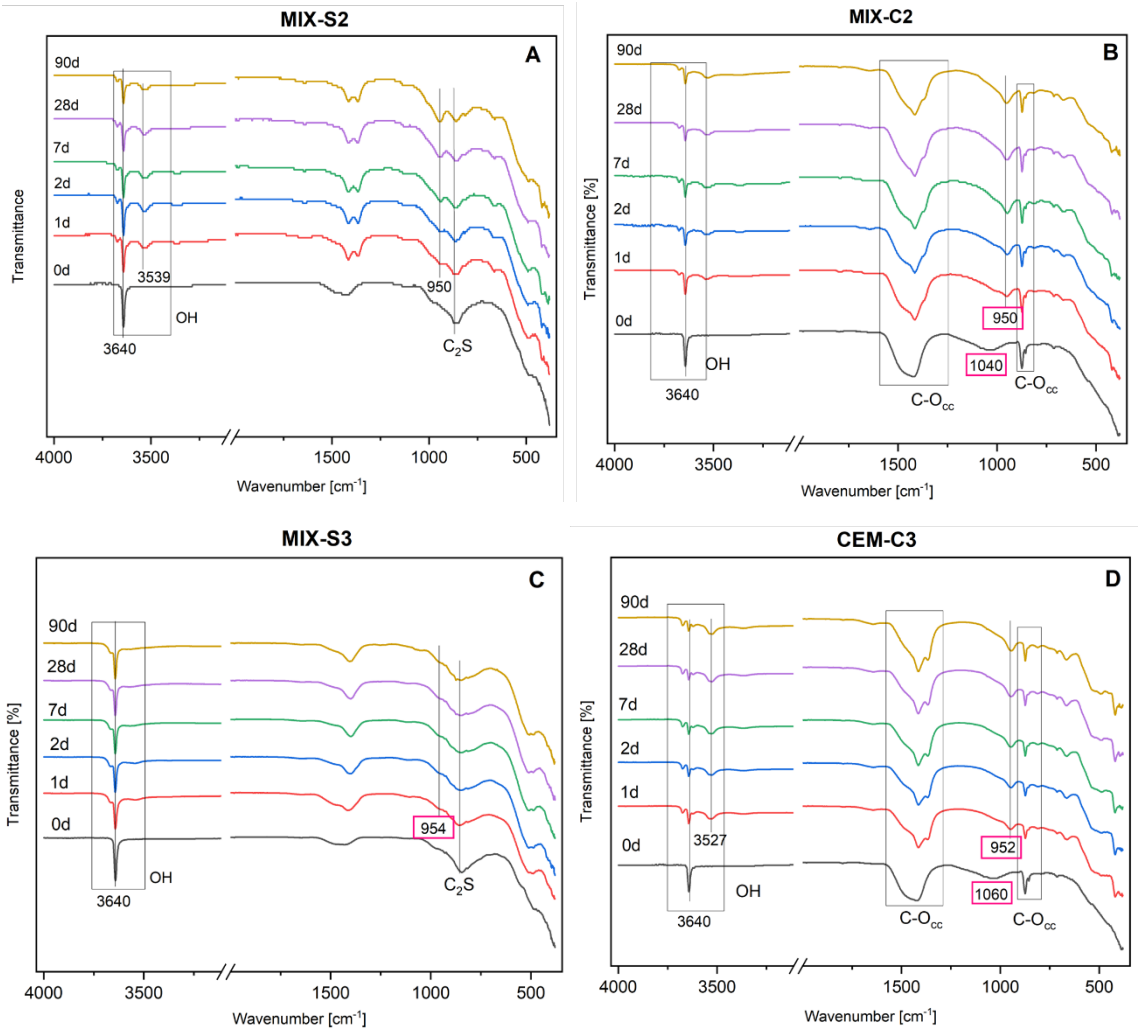

Figure 41. FT-IR analysis of starting materials, LF2 and LF3 (A and C) and carbonated products, cLF2 and cLF3 (B and D) portlandite blends, underling the formation of C-S-H product especially in carbonated by-products blends from 0 and 90 days

XRD analysis, as shown in **Figure 42**, was used to investigate the hydrated products, revealing hemicarbonate ($CaO\cdot Al_2O_3\cdot \frac{1}{2}CaCO_3\cdot \frac{1}{2}Ca(OH)_2\cdot 11.5H_2O$) and monocarbonate ($3CaO\cdot Al_2O_3\cdot CaCO_3\cdot 11H_2O$) phases as the primary crystalline products of the pozzolanic reaction. C-S-H also forms but cannot be detected by XRD due to amorphous properties. These phases form through reactions between calcium carbonate and aluminium [124,126]. In detail, katoite ($Ca_3Al_2(OH)_{12}$) is the main hydrated product of MIX-S3 since the first day (it isn't present in starting material as **Figure 36B** shows) whereas the presence of carbonate group in relative carbonated slag produces monocarbonate and hemicarbonate. Furthermore, a comparison of MIX-C3 with other carbonated MIX reveals a predominant formation of monocarbonate phases. This predominance likely accounts for the observed increase in bound water content, as well as the consumption of portlandite, both of which were quantitatively assessed through thermogravimetric (TGA) analysis (in **Figure 40**). For MIX-S8 and S9, the formation of expected hydration products isn't as evident as for other samples until 90 days confirming the low content of BW and portlandite decrease. Their corresponding products blends show the hemicarbonate is the main phase until 28 days but, at 90 days, in MIX-S9 hemicarbonate reacts with water and CO_3^{2-} ions becoming monocarbonate (as shown in **Figure 42E-F**).

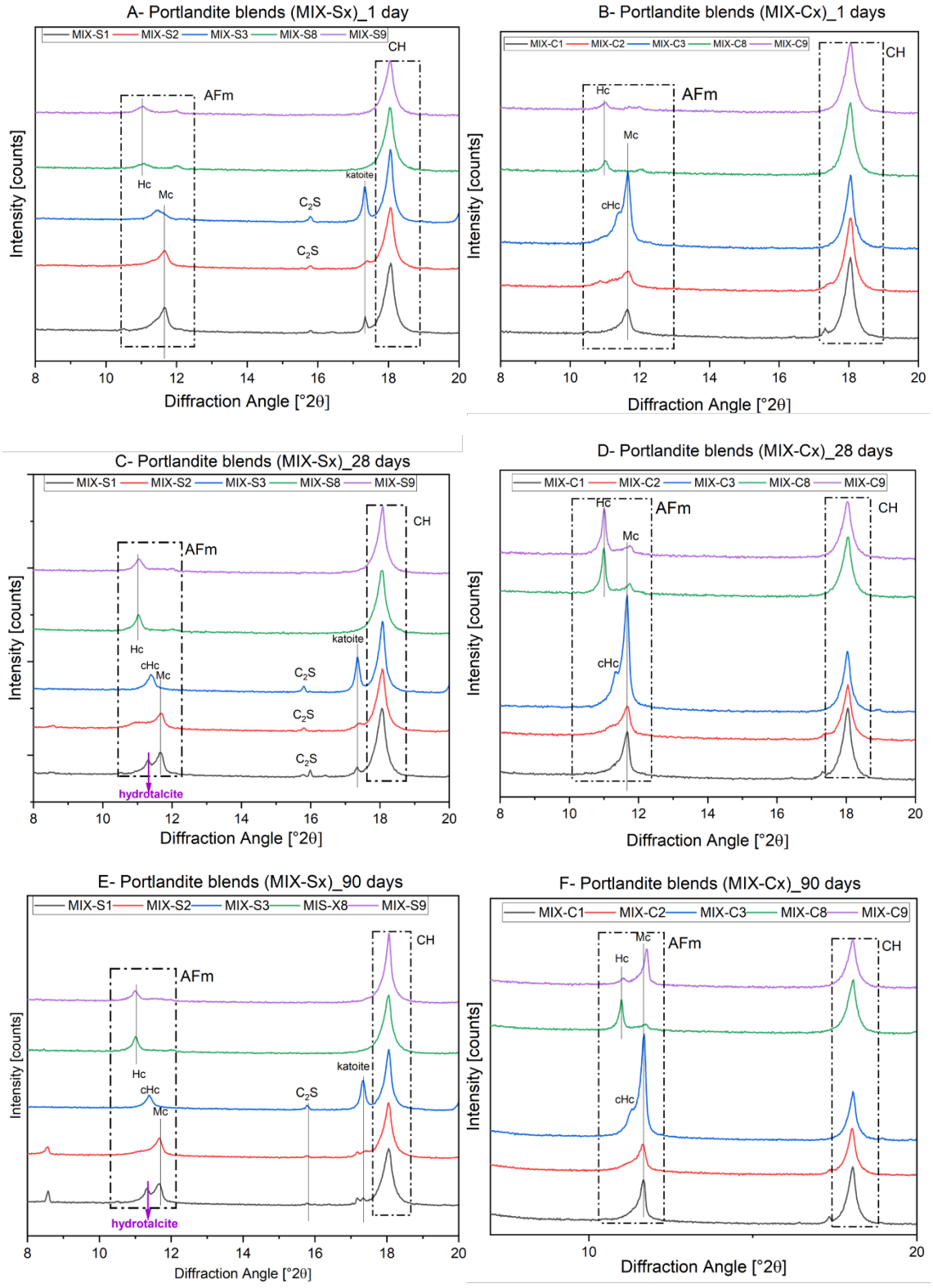

Figure 42. Comparison of XRD pattern of portlandite blends with starting material (A, C and E) and carbonated slag (B, D and F) at 1, 28 and 90 days. The graphs underline the formation of hydrated products, especially in mixes with carbonated slags (MIX-Cx) highlighting the importance of carbonation in the valorization process of slags as SCM

Mechanical performance

The compressive strength of untreated and carbonated slag mixes is reported in **Figure 43** and **Figure 44**. In this work, the reference sample was a composite cement that included limestone as a filler, with the same cement clinker replacement ratio as the samples with supplementary cementitious material. Limestone is considered a minor influencing factor in mechanical performance. It is important to note that the Portland cement CEM I used already contains small amounts of calcite, which are sufficient to generate monocarbonate and stabilize ettringite content [127]. Consequently, any differences in mechanical performance between cement containing limestone and that incorporating carbonated materials highlight the role of the pozzolanic reaction in overall mechanical behaviour. When the cement is partially replaced by limestone (CEM-L), in 40 % weight, the mechanical performances decrease due to the dilution effect. The same result is obtained when steel slag replaces the CEMI because of C_2S and iron phases has a poor hydraulic and reactive characteristic which negatively impacted the formation of C-S-H [62]. Despite that, CEM-S8 shows the highest value at 28 days (50.8 MPa) due to the presence of Ca phases that reacts with water to form C-S-H. The worst performances at 1 and 2 days are reported for CEM-S3 and CEM-S9 which compressive strength doesn't reach 10 MPa, but after 28 days these values increase, especially for CEM-S9 which reaches 46.5 MPa. This behaviour may be due to slow hydration kinetics for some mineralogical phases as belite that can happen at 10 days [54]. A different behaviour is exhibited from carbonated steel slag mixes. The mechanical performances of corresponding mortar mixes are not equal to reference values, but the values are higher than mixes with untreated slag. The main cause is the valorization of hydraulic activity of slag's mineral in pozzolanic calcium hydrates silicates (C-S-H) by carbonation process. After 28 days, the increase of carbonated slag addition is highlighted respect when the steel slag is added, for CEM-C3 (at 7 days 50.2 MPa and 28 days 58.5 MPa) with an increment of 42 %. However, for Slag8 and 9, the reactivity of starting material is comparable with carbonated slag after 28 days. The calcite content of cLF3 is lower than of cLF2 and cSlag8 and Fang et al. [58] have demonstrated that a higher degree of carbonation favours the pozzolanic reaction but an excessive of calcite can decrease the hydration activity of steel slag.

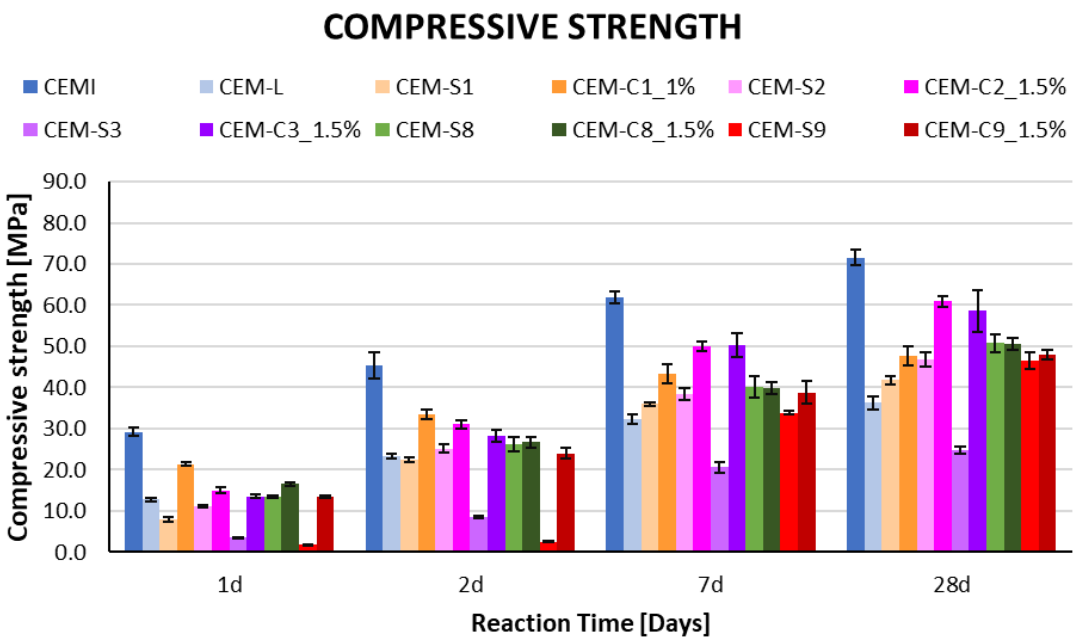

Figure 43. Compressive strength evolution in the composite cement mixes at 1, 2, 7, 28 and 90 days. All composite cements contain 40% of different supplementary cementitious materials and the additives as reported in **Table 1.** The values are the average of six measurements and the standard deviations are reported as error bar.

Based on the results reported from TG and XRD techniques, only mortar mixes with carbonated steel slag were tested at 90 days to verify if the amorphous content has a latent reactivity. As reported in **Figure 44**, only CEM-C2_1.5% and CEM-C3_1.5% has a difference of 7 MPa between 28 and 90 days, like the reference trend.

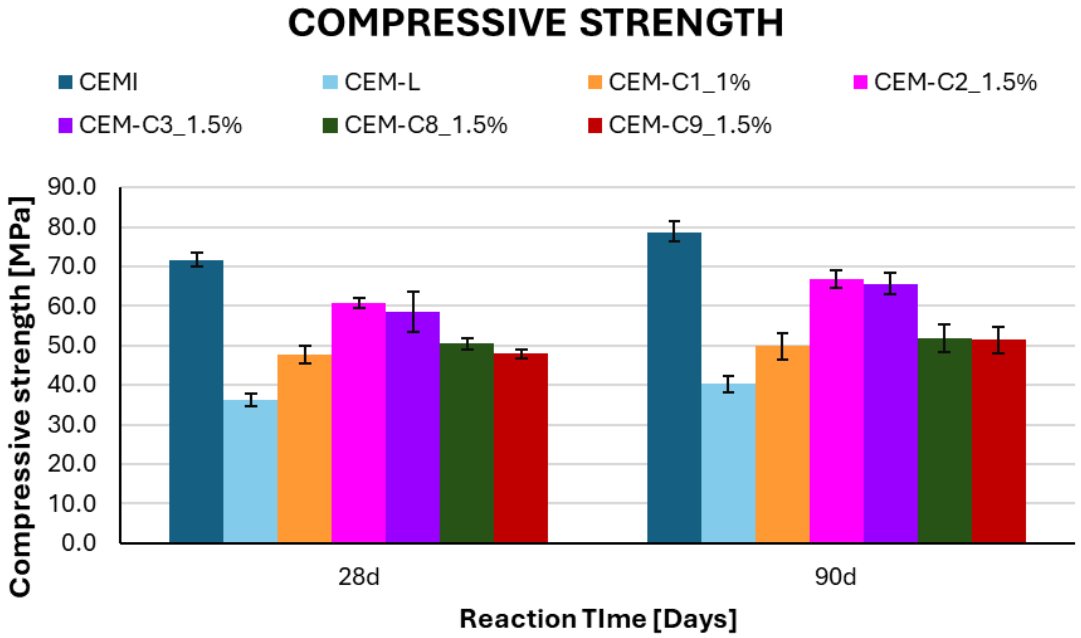

Figure 44. Compressive strength evolution in the composite cement mixes at 28 and 90 days. All composite cements contain 40% of different supplementary cementitious materials and the additives as reported in **Table 1.** The values are the average of six measurements and the standard deviations are reported as error bar

Conversely, while the incorporation of carbonated steel slag tends to reduce compressive strength relative to plain cement, it still yields higher values compared to mixtures incorporating uncarbonated steel slag or limestone. Comparative analysis with prior studies sheds light on the positive influence of carbonation on mechanical performance. For instance, He et al. ([128]) observed that increasing the degree of carbonation facilitated the formation of nano-scale $CaCO_3$ crystals, which enhanced crystallinity and promoted hydration, leading to a 58.5% improvement in early-age compressive strength when 30% of cement was substituted with carbonated slag. In a similar vein, Fang et al. ([129]) found that semi-dry carbonation resulted in a 22.7% increase in the 3-day compressive strength of mortar relative to its non-carbonated counterpart, a result attributed to a denser microstructure and stronger interaction among hydration products.

From an environmental perspective, the utilization of steel slags via carbonation processes contributes meaningfully to global sustainability targets by facilitating CO_2 sequestration and supporting circular economy principles within the cement sector. Ongoing research into the development of advanced carbonation methodologies, specifically tailored to the physicochemical characteristics of various slag types, is essential for optimizing mechanical performance and expanding the potential application of carbonated steel slags in high-performance cementitious systems.

CHAPTER 5

CONCLUSIONS

This project represents a preliminary investigation into the potential of steel slag for CO_2 sequestration and its reuse as a Supplementary Cementitious Material (SCM) in composite cements. The research particularly focuses on how the mineralogical and chemical composition of various steel slags influences the carbonation process, and how the subsequent carbonation enhances the mechanical performance of cementitious systems incorporating these slags. A range of different slags were systematically tested to evaluate how their intrinsic properties affect their behaviour during carbonation and their effectiveness as SCMs.

One key question addressed is: what factors most significantly influence the carbonation reaction? Undoubtedly, the mineralogical and chemical composition, two closely interconnected parameters, play the most critical roles. The presence of high concentrations of calcium and magnesium bearing minerals strongly enhances the CO_2 uptake. Reactive phases such as belite (C_2S), bredigite ($Ca_7Mg(SiO_4)_4$), mayenite ($C_{12}Al_{14}O_{33}$), and periclase (MgO) are particularly known for their high reactivity in this process. Consequently, slags such as AOD (Argon Oxygen Decarburization) and LF (Ladle Furnace) exhibit greater suitability for carbonation compared to EAF (Electric Arc Furnace) slags, which typically have a less reactive composition.

Another important parameter influencing carbonation efficiency is the particle size distribution (PSD). Finer particles present a larger specific surface area, increasing the contact area between the powder and the CO_2 gas, and thus promoting higher reaction rates. However, in this study, the PSD was intentionally homogenized across different slag samples by applying a highly energy-intensive grinding process, achieving a uniform PSD, with maximum variations of 10–15 µm. To better understand the influence of PSD, it would be useful in future work to perform carbonation experiments on the same material at different controlled particle sizes, to identify the optimal balance between fineness, reactivity, and energy consumption.

Additionally, the iron content in the slags is another crucial aspect to consider. Some studies have shown that the presence of Fe can lead to the formation of surface layers that inhibit the interaction between the material and CO_2, limiting the extent of carbonation. Furthermore, higher Fe content increases the hardness of the material, making the grinding process more energy-demanding. Materials with FeO contents below 10% are notably easier to process. In this study, a magnetic separation process was employed to reduce the Fe content in the slags, aiming to minimize potential interference in the cementitious system due to oxidation reactions and consequent alterations in the colour of the cement product. However, this magnetic separation process is itself complex and energy-intensive, and future optimizations should include a detailed cost and emissions analysis.

An additional aspect to consider is the hydration process of the mineralogical phases. As demonstrated for BF slag, increasing the hydration time of the material significantly enhances its

reactivity, with calcite formation increasing fivefold (from 16% to 60%) while the amorphous phase content, initially around 80%, was substantially reduced. This finding underlines the importance of further investigating the role of hydration for other slag types as well, to determine whether certain phases, if hydrated over specific periods, could improve their reactivity and to better understand the mechanisms by which hydration facilitates this improvement. This could open new avenues to optimize the carbonation process, especially by combining controlled hydration and carbonation stages.

Different experimental carbonation conditions were tested, leading to different results. Under ambient conditions, reactive slags such as LF2 demonstrated a CO_2 sequestration of about 100 g CO_2/kg slag, whereas AOD slags, despite their reactivity under high-pressure conditions, showed lower yields under mild conditions due to the presence of poorly reactive phases like bredigite. The highest sequestration performance was recorded for BF (Blast Furnace) slag, reaching 160 g CO_2/kg slag, also correlated to its highest CaO content (56%). Poorly reactive slags such as EAF slags exhibited the lowest sequestration capacity, achieving only 20 g CO_2/kg slag. Although carbonation under ambient conditions is low-cost and industrially feasible, the yields are not yet competitive when compared either to enforced carbonation methods or to the scale of industrial CO_2 emissions.

Regarding enforced carbonation, two different strategies were explored: the first involved the use of high CO_2 pressure (15 bar) combined with a thin film route (low L/S ratio), while the second employed ambient pressure, continuous gas flow, and higher L/S ratios. In the first case, calcium-aluminate phases reacted more efficiently. Continuous CO_2 flow experiments allowed for real-time monitoring of CO_2 uptake, while high-pressure reactor tests enabled the study of exothermic behaviour, such as temperature increases during reaction and the influence of stirring speed on absorption rates. However, from an industrial perspective, maintaining such high pressures is more challenging both in terms of plant design and operational costs. Conversely, continuous CO_2 flow under ambient pressure better mimics realistic industrial conditions, particularly in facilities such as cement or slag processing plants where CO_2 capture is already integrated.

Therefore, the selection of materials with higher reactivity, lower Fe content, and controlled particle size is essential to improve the industrial feasibility of the process. From this study, it is evident that LF slags (particularly LF2 and LF3) and AOD slags are the most suitable candidates for the carbonation process, due both to their high CaO contents (approximately 40–45%) and MgO contents (around 10%), as well as their relatively low FeO content, which remains below 15%. These chemical characteristics strongly favour CO_2 uptake while minimizing the negative effects associated with high iron content, such as reduced reactivity and increased grinding energy demand. Understanding the right particle size to ensure an optimal compromise between reactivity and process efficiency will also be crucial, especially for scaling up within an industrial setting.

From the perspective of practical applications, this study highlights the valorization potential of carbonated steel slag within the construction sector. Carbonation plays a crucial role in activating hydraulic phases, with slow reactivity, such as C_2S, thus improving the material's performance as a cement substitute. As demonstrated, the partial replacement of cement with carbonated slag leads to higher compressive strengths compared to the use of non-carbonated slags. LF3 slag showed the best performance as SCM, especially when compared to its non-carbonated counterpart. The presence of high amounts of $CaCO_3$ and Al_2O_3 promoted the formation of monocarbonate phases, significantly improving the mechanical properties of the composite

material. Moreover, the addition of hemihydrate as an additive helped balance the sulphate content, further enhancing performance.

In general, the amount of $CaCO_3$ formed during carbonation, as well as the chemical and mineralogical composition of the slag, have a crucial influence on the suitability of carbonated slags as SCMs. An excessively high calcite content may negatively impact the hydration activity of the slags, potentially reducing their contribution to mechanical strength development. On the other hand, the presence of aluminium can promote the formation of beneficial phases such as monocarbonate, which contribute positively to the hydration process. Additionally, the presence of mineral phases with reactivity like that of ordinary cement phases is an important added factor, as it enhances the compatibility and performance of the composite cement system.

Overall, this project offers a comprehensive overview of the opportunities and challenges associated with the use of steel slag in CO_2 sequestration and as an SCM. It identifies key achievements while acknowledging the considerable work still required to fully optimize the process for industrial-scale applications. In general, steel slag demonstrates a strong potential for CO_2 capture, in agreement with findings from previous studies [53,97,98]. Nevertheless, a deeper understanding of the effects of various reaction parameters, such as slag composition, carbonation conditions, and pre-treatment methods, is essential for improving process efficiency and scalability.

About its application in cementitious systems, this research represents an initial step toward a broader evaluation, as several complex factors including the influence of heavy metals, residual sulphates, and slag fineness could affect the hydration kinetics and performance but were beyond the scope of this work. It is well established that cementitious matrices have the capability to immobilize heavy metals, suggesting that with careful process optimization, environmental risks can be minimized.

In conclusion, this study offers a new valorization pathway for steel slag by coupling carbonation with the integration of industrial by-products, such as cement kiln dust, as functional additives, thereby enhancing the circular economy framework within the construction industry. This approach not only supports sustainable waste management strategies but also contributes to the reduction of carbon emissions in the cement sector, pointing the way toward greener, more resilient construction materials.

CHAPTER 6

FUTURE RESEARCH

A key priority for future research is the identification and selection of steel slags with the highest potential for both CO_2 sequestration and utilization as Supplementary Cementitious Materials (SCMs). Slags such as LF2, LF3, and AOD have demonstrated favourable characteristics, including high contents of CaO and MgO and lower FeO levels, making them promising candidates for further studies and industrial application.

Building upon this, several promising directions for future research emerge to optimize the use of steel slag in CO_2 sequestration and as SCMs. Firstly, a deeper investigation into the influence of mineralogical hydration is crucial. As demonstrated with BF slag, prolonged hydration significantly increased its reactivity, specifically the amorphous phases, and CO_2 sequestration capacity; similar studies should be conducted on other slags to understand if controlled hydration periods could improve their carbonation behaviour and SCM performance. Additionally, the role of particle size distribution (PSD) needs further exploration. Although in this work the PSD was homogenized, systematic studies using different particle size fractions of by-products could better define the ideal size range for maximizing reactivity while balancing industrial energy costs.

Moreover, the impact of Fe content deserves more attention, particularly in developing more efficient and less energy-intensive magnetic separation processes to reduce FeO concentrations without significantly increasing emissions or costs. Future works should also investigate the optimization of carbonation conditions. Comparing the kinetic behaviour under different pressures, gas flows, and liquid-to-solid ratios has shown promising but complex trends that need to be better modelled to design scalable and economically viable industrial processes. In parallel, the optimization of the carbonation and grinding processes should be re-evaluated together with companies interested in the project, both to assess the industrial feasibility and to directly involve stakeholders in the Bergamo-Brescia area. Establishing partnerships with industry could support the development of scalable, cost-effective processes and accelerate real-world application.

Regarding the use of carbonated slag as SCM, further research is required to fully understand how different $CaCO_3$ contents, Al_2O_3 levels, and phase assemblages affect the long-term hydration kinetics and durability of the final composite material. In particular, the amount of $CaCO_3$, chemical and mineralogical composition of the slag play a crucial role: while a certain amount of calcite can be beneficial, too high a content could inhibit the hydration reactions, reducing mechanical performance. At the same time, the presence of Al can favour the formation of monocarbonate, and the existence of mineral phases like those of cement provides an additional advantage for reactivity and mechanical performance. Another critical point for future studies is the behaviour of heavy metals in the composite cements. It is important to understand whether heavy metals, such as Cr, influence cement hydration reactions and, if so, by what mechanisms. Furthermore, leaching tests should be conducted to evaluate the environmental safety of the final material and prevent the release of potentially hazardous elements.

Additionally, a deeper environmental impact assessment is essential, including not only CO_2 emissions and sequestration balances but also a broader evaluation of the benefits from using recycled materials and minimizing virgin resource consumption. Future research should also focus

on the use of non-synthetic additives containing sulphates, such as cement kiln dust, offering a double advantage: rebalancing sulphate contents and valorising waste materials from the cement industry itself.

On the other hand, carbonation under very mild conditions should not be further pursued, as the results obtained demonstrate that it is not competitive compared to enforced carbonation processes, both in terms of sequestration efficiency and industrial applicability.

Finally, future research should integrate life cycle assessments (LCA) and techno-economic evaluations to validate the overall sustainability, environmental viability, and cost-effectiveness of the carbonation and slag valorization processes developed.

At the end, beyond the purely scientific and technical advancements, this project lays down the essential foundations for a broader vision: one where industrial symbiosis becomes a concrete reality. The hope is that the work initiated here can inspire greater collaboration among the companies operating in this sector, creating a virtuous network within the Bergamo-Brescia area, a region historically shaped by steel and cement industries. Here, where tradition and innovation have always gone hand in hand, the challenge is to build new models of sustainability, transforming what was once considered waste into a valuable resource for the future. The path has been outlined; now it is up to a shared commitment to turn this opportunity into a lasting and tangible reality.

APPENDIX

7.1 High-pressure Carbonation (small set up)

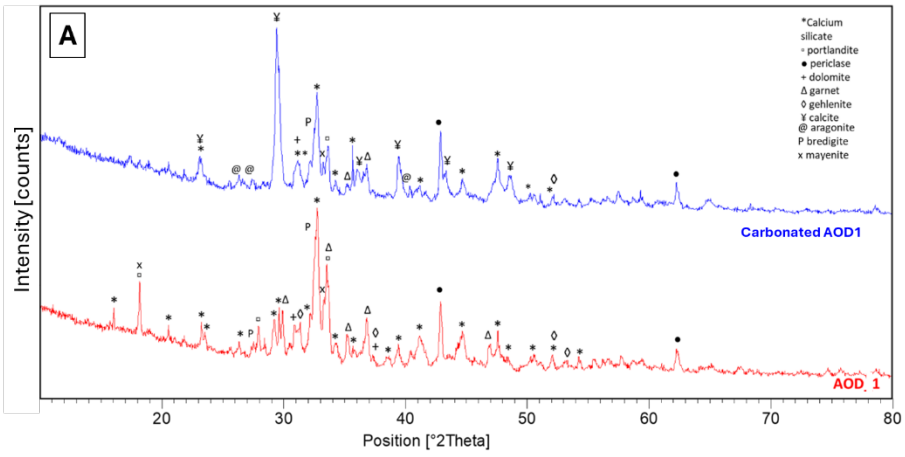

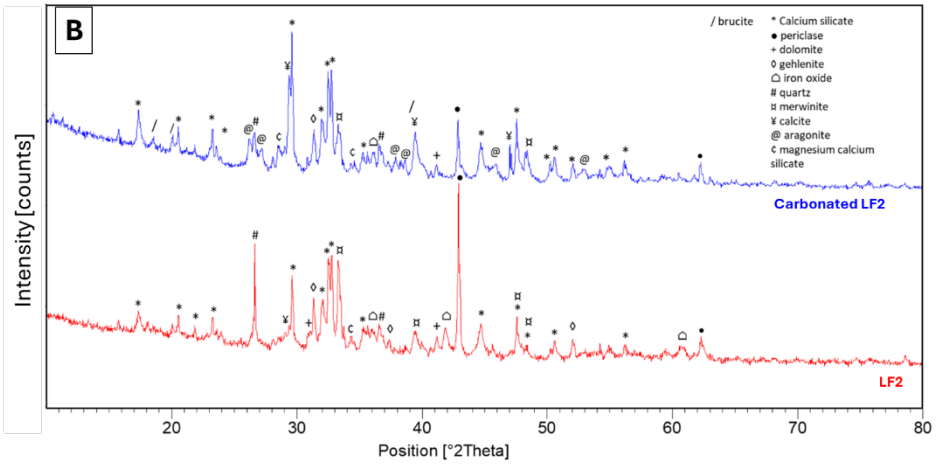

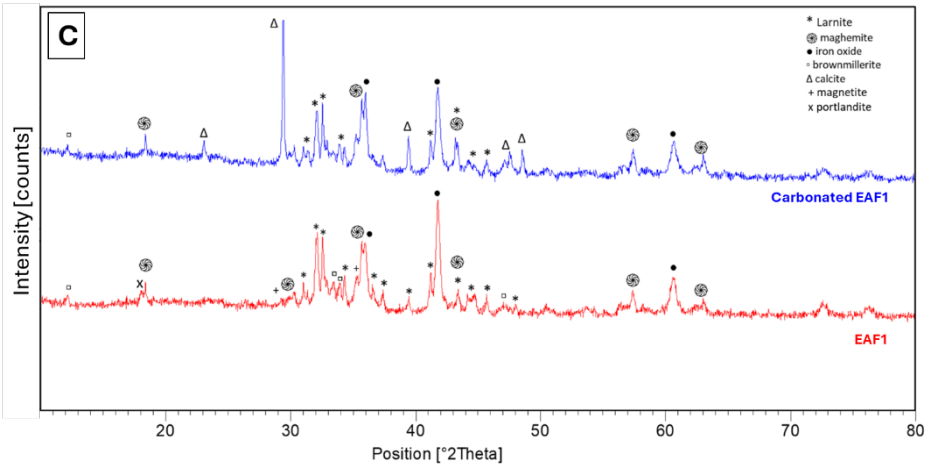

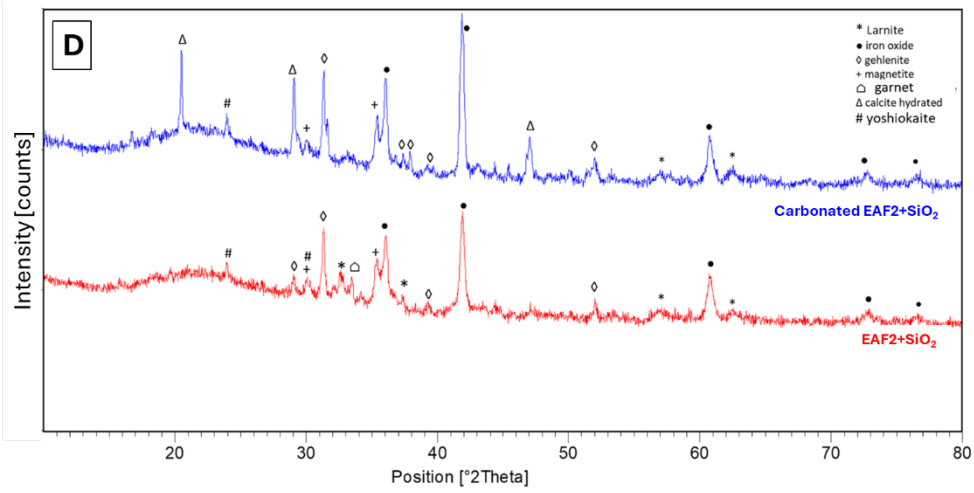
D
* Larnite
● iron oxide
◊ gehlenite
+ magnetite
⌂ garnet
Δ calcite hydrated
yoshiokaite
Carbonated EAF2+SiO2
EAF2+SiO2
Intensity [counts]
Position [°2Theta]
20
30
40
50
60
70
80

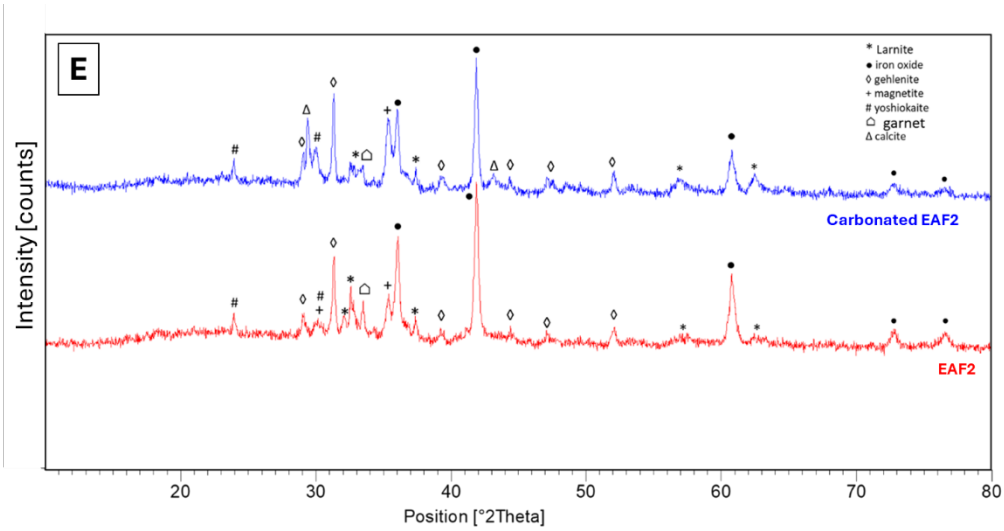
E
* Larnite
● iron oxide
◊ gehlenite
+ magnetite
# yoshiokaite
⌂ garnet
Δ calcite
Carbonated EAF2
EAF2
Intensity [counts]
Position [°2Theta]
20
30
40
50
60
70
80

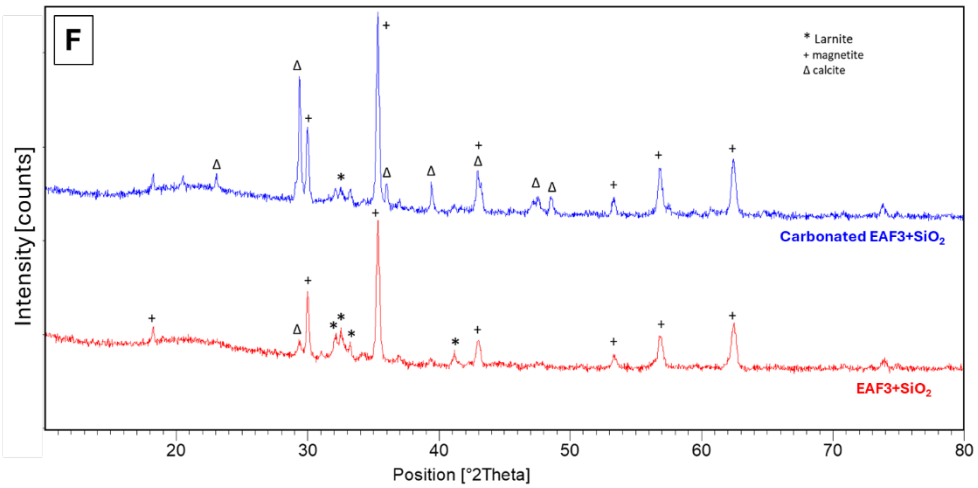
F
* Larnite
+ magnetite
Δ calcite
Carbonated EAF3+SiO2
EAF3+SiO2
Intensity [counts]
Position [°2Theta]
20
30
40
50
60
70
80

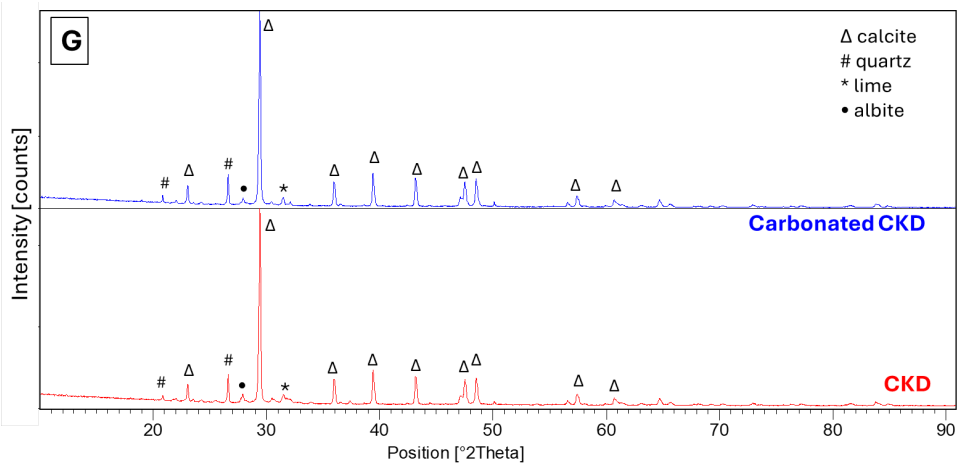

Figure A- 1. Comparison of XRD pattern before and after carbonation, highlighting the phase transformations and mineralogical changes induced by the carbonation process. The mineralogical phases are reported in the figure, and different symbols represents different mineralogical phases. The XRD pattern of starting materials and relative carbonated products are in the followed order: AOD1 (A), LF2 (B), EAF1 (C), EAF2+SiO_2 (D), EAF2 (E), EAF3+SiO_2 (F) and CKD (G)

Table A- 1. QXRD quantification about accelerated carbonation in the small set up (24 hours, 15 bar, L/S =1.5, room temperature). The values below 1% are expressed as < 1 %. Carbonated samples are named by using letter c before the name.

Sample	**cAOD_1**	**cLF_2**	**cEAF_1**	**cEAF_2**	**cEAF_2 + SiO2**	**cEAF_3 + SiO2**	**cCKD**
	[wt%]	[wt%]	[wt%]	[wt%]	[wt%]	[wt%]	[wt%]
Albite	-	-	-	-	-	-	< 1
Amorphous	54.0	29.5	29.5	60.2	73.5	62.3	2.5
Aragonite	1.0	8.7	-	-	-	-	-
Bredigite	2.2	-	-	-	-	-	-
Browmillerite	-	-	9.31	-	-	-	-
Brucite	-	< 1	-	-	-	-	-
Calcite	16.7	8.8	16.7	7.5	9.2	14.0	95.0
Dolomite	3.0	< 1	-	-	-	-	-
f-lime	-	-	-	-	-	-	< 1
Garnet	3.6	-	-	-	-	-	-
Gehlenite	< 1	5.4	-	8.8	6.2	-	-
Hydrogarnet	-	14.3	-	-	-	-	-
Maghemite	-	-	7.8	-	-	-	-
Magnetite	-	-	3.1	5.7	2.1	16.6	-
Mayenite	2.8	-	-	-	-	-	-
Merwinite	-	0.5	-	-	-	-	-
Olivine	-	17.7	-	-	-	-	-
Periclase	5.2	5.1	-	-	-	-	-
Portlandite	< 1	-	< 1	-	-	-	-
Srebrodolskite	-	-	-	3.7	< 1	-	-
Wuestite	-	< 1	11.7	13.2	7.3	-	-
Yoshiokaite	-	-	-	< 1	< 1	-	-
β-C_2S	12.3	-	21.2	1.3	< 1	6.7	-
γ-C_2S	-	8.3	-	-	-	-	-
Total	100.8	98.3	99.6	100.4	98.3	99.6	97.5

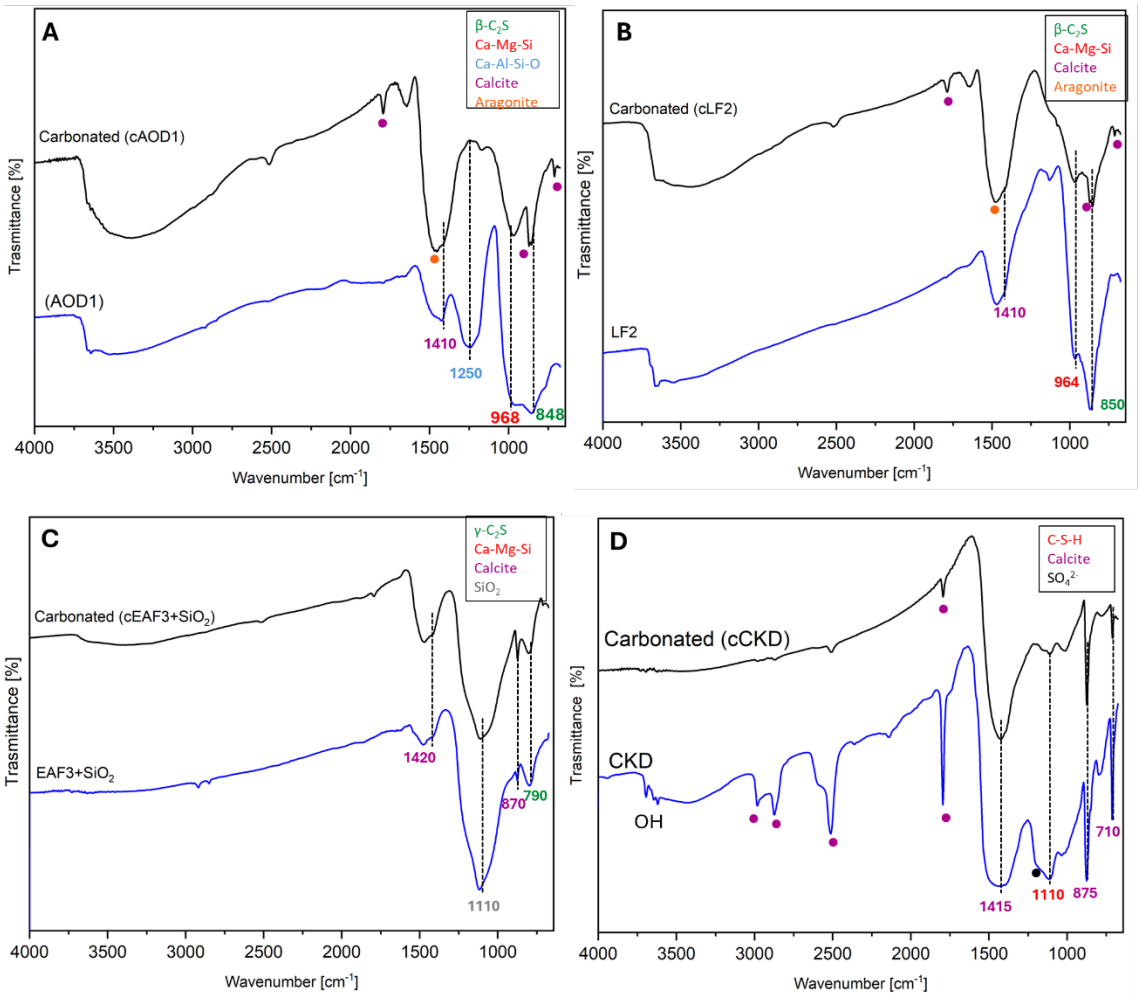

Figure A- 2. FT-IR spectra of starting materials and carbonated steel slags for AOD1 (A), LF2 (B), EAF3+SiO2 (C) and CKD (D). At 3000-3500 cm^{-1} the large band is correlated with the moisture that is adsorbed by the sample during the analysis

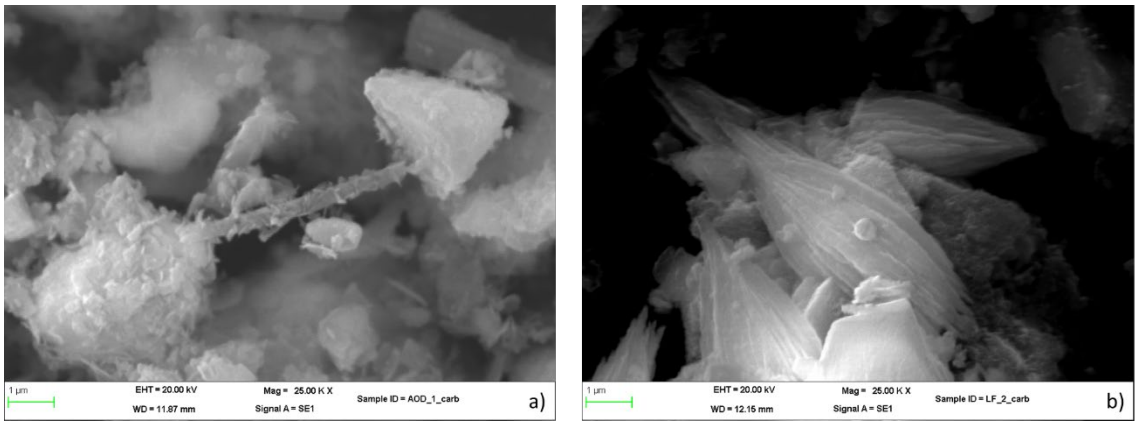

Figure A- 3. SEM images of AOD_1 carbonated (a) and LF2 carbonated highlighting the difference morphology after the carbonation process.

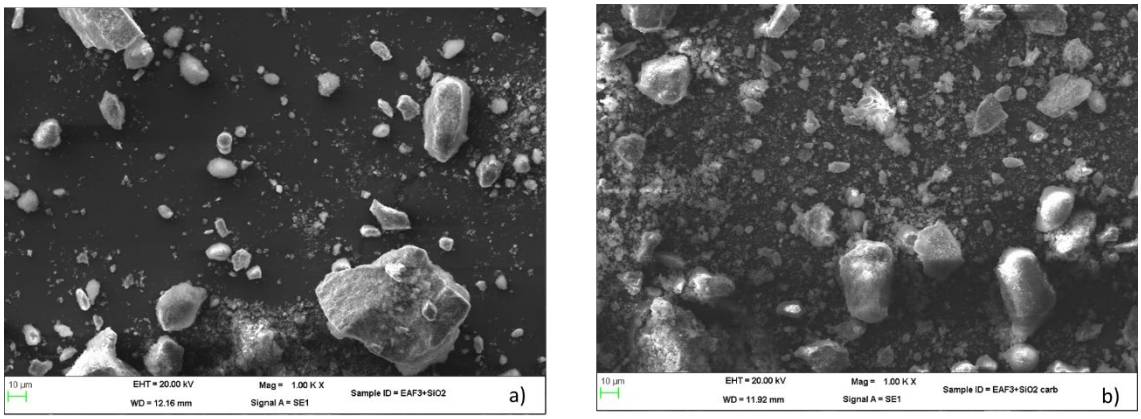

Figure A- 4. SEM images of EAF3 + SiO2 (a) and carbonated product (b) underling the changes of morphology and distribution of the particle before after the carbonation process

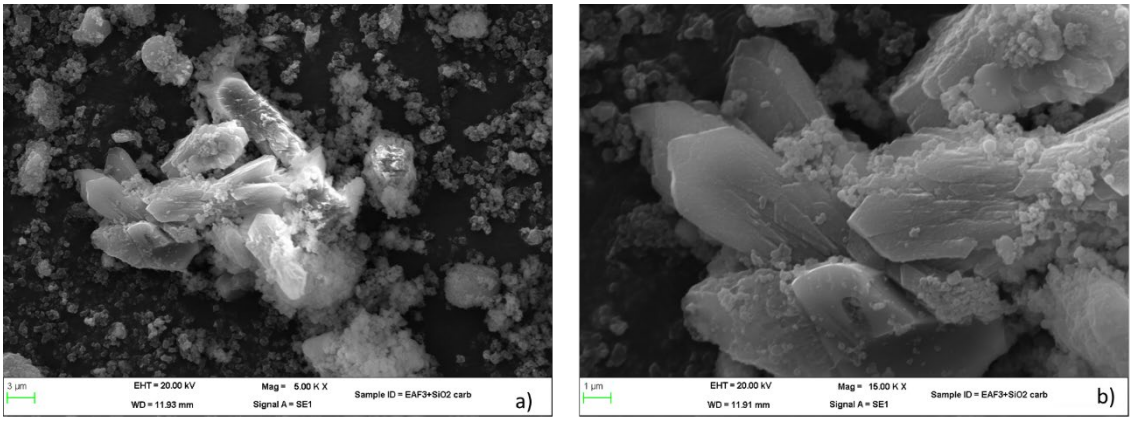

Figure A- 5. SEM images of calcite for EAF3 + SiO_2 at different extensions. The images highlights the formation of calcite crystal and the enhance of crystallinity part

7.2 High-pressure carbonation (Berghof set up)

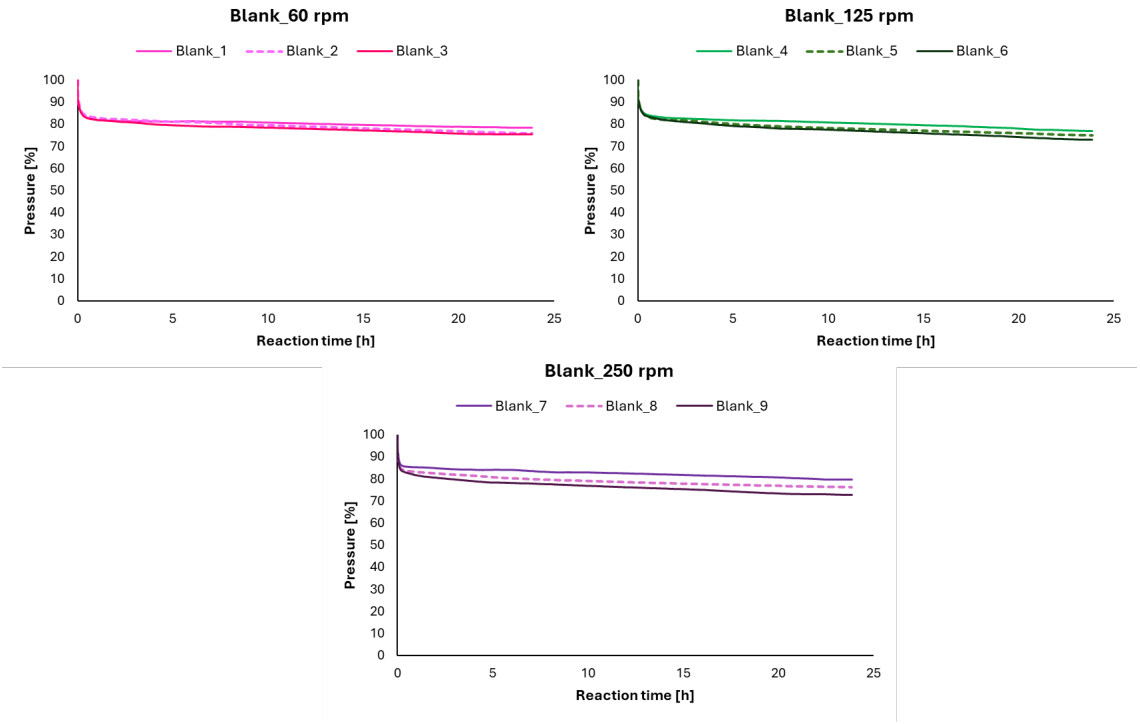

Figure A- 6. The graph illustrates the decreasing of CO_2 pressure consumption over a 24-hour process, room temperature and 15 bar. Three different stirring speed were tested 60 (pink curve), 125 (green curve) and 250 rpm (purple curve). The trend was similar in all the three repetition for each stirring value and the 80% of injected CO_2 didn't react

Table A- 2. Reaction parameters (initial and final) for the high-pressure carbonation (Berghof set up) process at 15 bar, 24 hours, including pH, initial and final pressures and temperature, three different stirring speed, final mass of the dry sample and initial injected CO_2 mass, with the parameters referring to the carbonation reaction for LF3 and LF1. The table shows the data regarding test 2 for each speed and material

		LF3_60_2	LF3_125_2	LF3_250_2	LF1_60_2	LF1_125_2	LF1_250_2
v	**[rpm]**	60	125	250	60	125	250
pH_i		12	12	12	12	12	12
p_i	**[bar]**	15.2	15.9	15.8	16.3	15.2	16.4
T_i	**[°C]**	24.0	24.6	26.5	27.8	27.9	24.9
pH_f		7	7	7	7	7	7
p_f	**[bar]**	0.56	1.42	0.53	4.63	2.62	4.21
T_f	**[°C]**	26.6	26.6	26.2	28.1	27.1	27.0
m_f	**[g]**	37.3	40.4	37.2	33.8	33.9	33.2
m CO2 injected	**[g]**	8.5	8.9	9.0	9.0	8.6	9.2

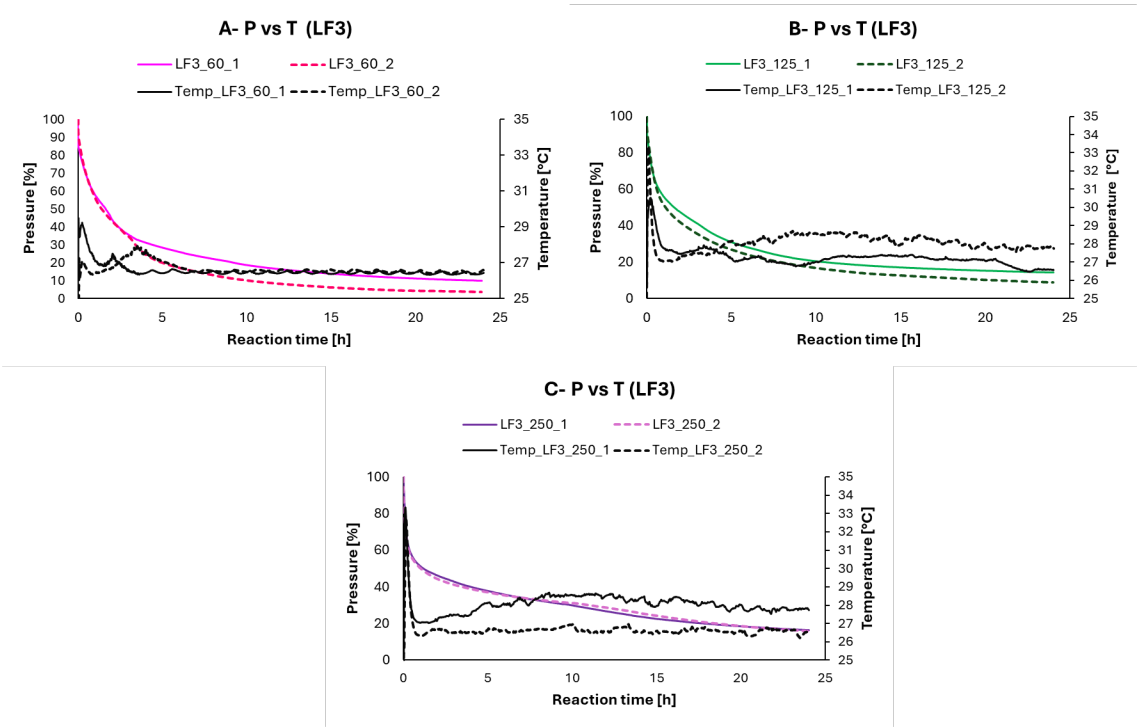

Figure A- 7 Comparison between CO_2 pressure and temperature trends for LF3 slag during the entire time of reaction at different stirring speeds: (A) 60 rpm, (B) 125 rpm, and (C) 250 rpm. In each graph, a noticeable correlation is observed between temperature peaks and sharper drops in pressure, suggesting an active phase in the reaction process. The graph of test 1 and test2 are reported: the dotted lines represent the test 2 (temperature and pressure values); whereas the continuous line represents the test 1 (pressure and temperature values). A dynamic interplay between thermal and pressure changes at varying stirring intensities is evident.

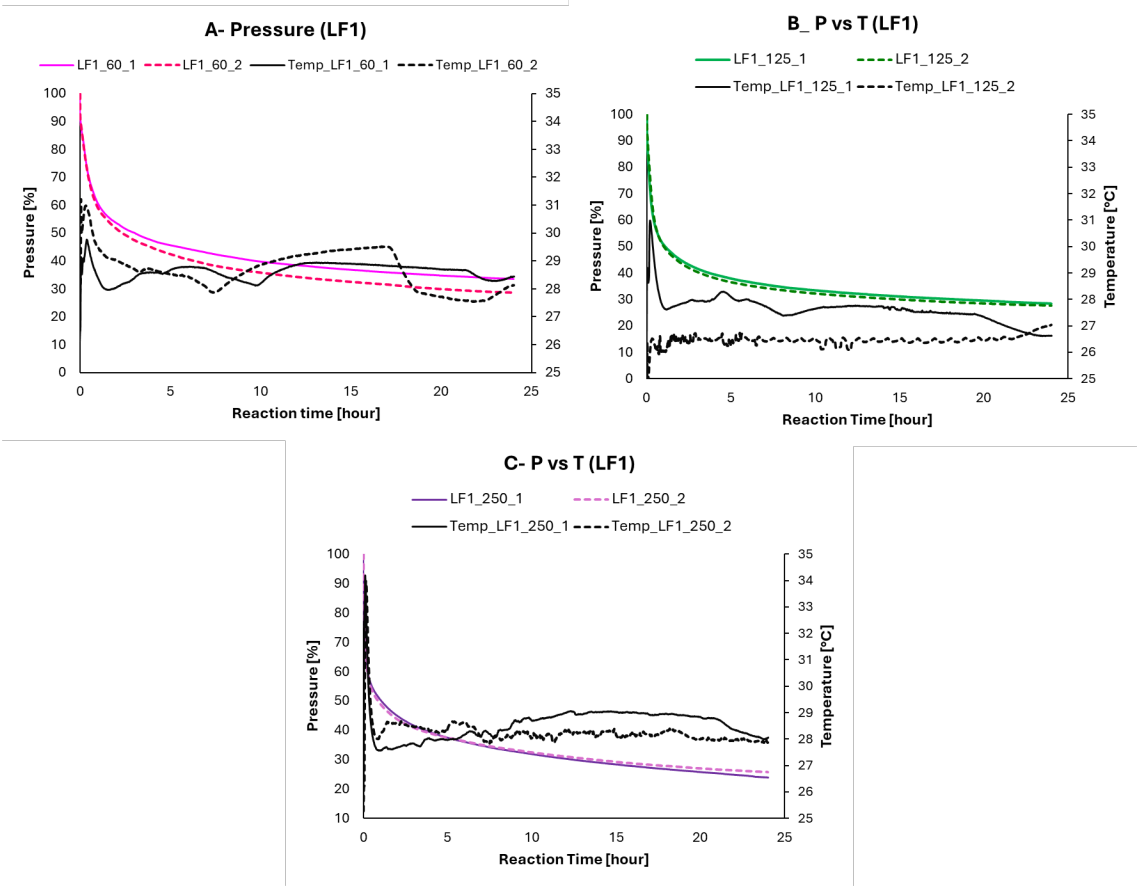

Figure A- 8 Comparison between CO_2 pressure and temperature trends for LF1 slag during the entire time of reaction at different stirring speeds: (A) 60 rpm, (B) 125 rpm, and (C) 250 rpm. In each graph, a noticeable correlation is observed between temperature peaks and sharper drops in pressure, suggesting an active phase in the reaction process. The graph of test 1 and test2 are reported: the dotted lines represent the test 2 (temperature and pressure values); whereas the continuous line represents the test 1 (pressure and temperature values). A dynamic interplay between thermal and pressure changes at varying stirring intensities is evident

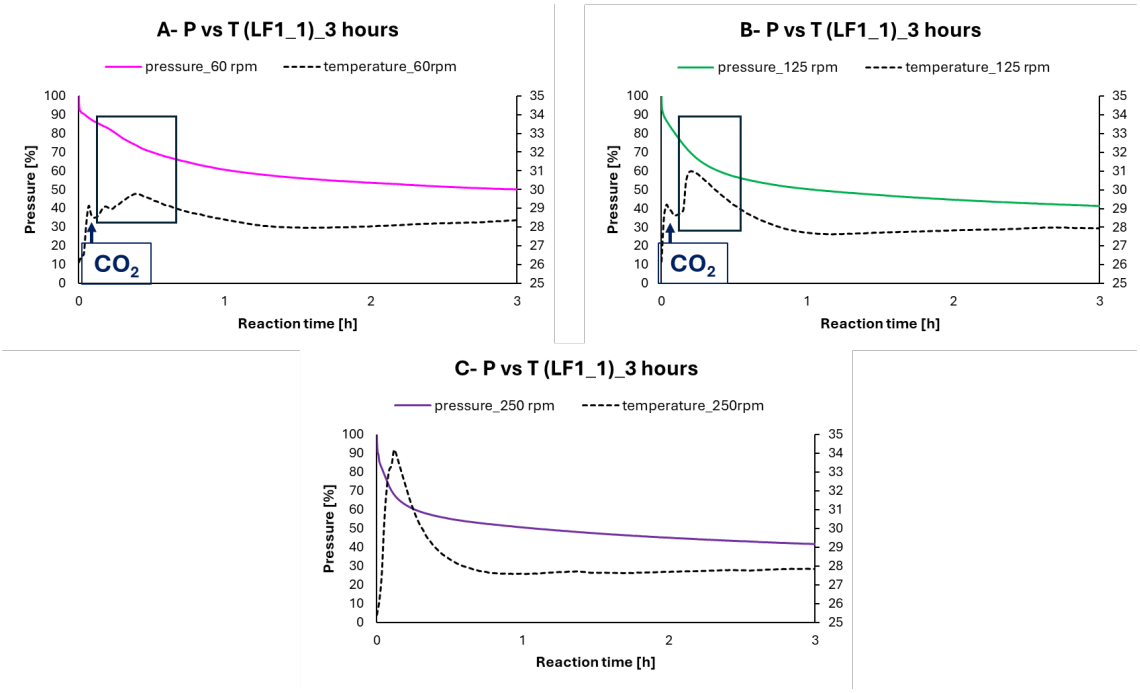

Figure A- 9. Comparison between CO_2 pressure and temperature trends for LF3 slag during the first 3 hours of reaction at different stirring speeds: (A) 60 rpm, (B) 125 rpm, and (C) 250 rpm. In each graph, a noticeable correlation is observed between temperature peaks and sharper drops in pressure, suggesting an active phase in the reaction process. Temperature is represented by dotted lines, while pressure trends are shown as continuous curves, highlighting the dynamic interplay between thermal and pressure changes at varying stirring intensities

Table A- 3. QXRD data of LF3 and LF1 samples after the carbonation process (24 h, 15 bar, room temperature and stirring speed = 60, 125 and 250 rpm). The data are the average values, and the error is the standard deviation

Samples	**LF3_60** [wt%]	**LF3_125** [wt%]	**LF3_250** [wt%]	**LF1_60** [wt%]	**LF1_125** [wt%]	**LF1_250** [wt%]
Akermanite	0.8±1.0	0.9±0.2	1.7±0.8	-	-	-
Alite	0.8±0.2	0.4±0.5	1.0±0.2	-	-	-
Aluminate	5.2±1.0	4.7±2.0	5.6±1.7	1.8±0.2	2.1±0.8	1.4±0.2
Amicite	-	-	-	0.1±0.2	0.2±0.3	
Amorphous	45.7±0.5	45.7±1.8	47.1±6.8	50.0±4.8	45.5±3.3	49.2±0.5
Andradite	0.6±0.6	1.2±0.2	0.3±0.2	-	-	-
Aragonite	13.0±3.2	14.3±5.6	6.1±2.8	0.6±0.8	1.3±0.9	1.0±1.4
Bredigite	-	-	0.5±0.7	-	0.2±0.2	0.6±0.1
Brownmillerite	1.2±0.4	1.5±0.1	1.6±0.03	-	-	-
brucite	0.7±0.01	0.2±0.2	0.4±0.3	-	-	-
Calcite	5.8±0.4	5.5±1.2	5.4±1.1	12.0±3.0	13.0±0.2	13.2±1.1
CalcitMg	3.8±1.2	3.0±0.6	3.2±0.7	2.5±0.7	3.1±0.8	2.5±1.2
Cuspidine	-	-	-	0.5±0.8	1.5±1.4	1.4±0.5
Diopside	-	-	-	0.5±0.3	1.0±0.1	0.8±0.1
Dolomite	0.6±0.2	1.5±0.7	1.9±1.1	1.4±0.6	1.6±0.6	0.9±0.2
Enstatite	-	-	-	5.5±0.0	6.1±0.2	4.9±1.0
Forsterite	1.6±0.6	0.8±0.2	0.7±0.3	11.4±1.0	11.6±0.4	11.1±1.5
Gehlenite	0.5±0.2	0.6±0.8	0.9±0.03	0.8±0.2	0.6±0.1	0.8±0.4
Hausmannite	0.2±0.03	0.1±0.1	0.5±0.5	-	-	-
hauyne	0.6±0.1	0.5±0.3	0.5±0.1	-	-	-
Hercynite	1.2±0.8	0.7±0.7	1.6±0.3	-	-	-
Hornblende (FeMg)	-	-	-	1.2±0.3	1.4±0.8	2.2±0.1
Kaolinite	1.1±0.01	0.2±0.3	0.1±0.2	-	-	-
Katoite	-	-	-	1.3±0.5	0.9±0.3	0.6±0.4
Magnetite	0.2±0.2	0.5±0.4	0.8±0.1	-	-	-
Mayenite	0.9±0.3	2.9±3.0	2.8±0.1	0.9±0.2	1.2±0.2	1.4±0.4
Monohydrocalcite	-	-	-	0.7±1.0	0.5±0.4	0.9±0.0
Monticellite	1.5±0.6	0.1±0.1	0.4±0.01	-	-	-
Mullite	-	-	-	1.4±0.3	1.4±0.8	1.3±0.03
Periclase	0.5±0.3	1.2±0.5	0.4±0.2	1.9±0.02	1.2±0.4	1.0±0.1
Quartz	-	-	-	1.3±0.3	1.4±0.2	1.6±0.5
Spinel	1.3±0.4	1.4±0.8	0.9±0.4	0.7±0.2	0.7±0.4	0.7±0.4
Vaterite	4.3±0.2	5.3±0.5	9.3±3.0	-	-	-
β-C2S	1.5±0.9	1.1±0.7	0.7±0.3	0.9±0.1	1.2±0.8	1.1±0.4
γ-Al2O3	-	-	-	-	0.1±0.1	0.1±0.1
γ-C2S	5.1±1.3	5.2±0.04	4.6±1.0	2.8±0.6	2.2±0.8	1.6±0.3
Total	99.7	100.3	100	100.4	99.8	100.2

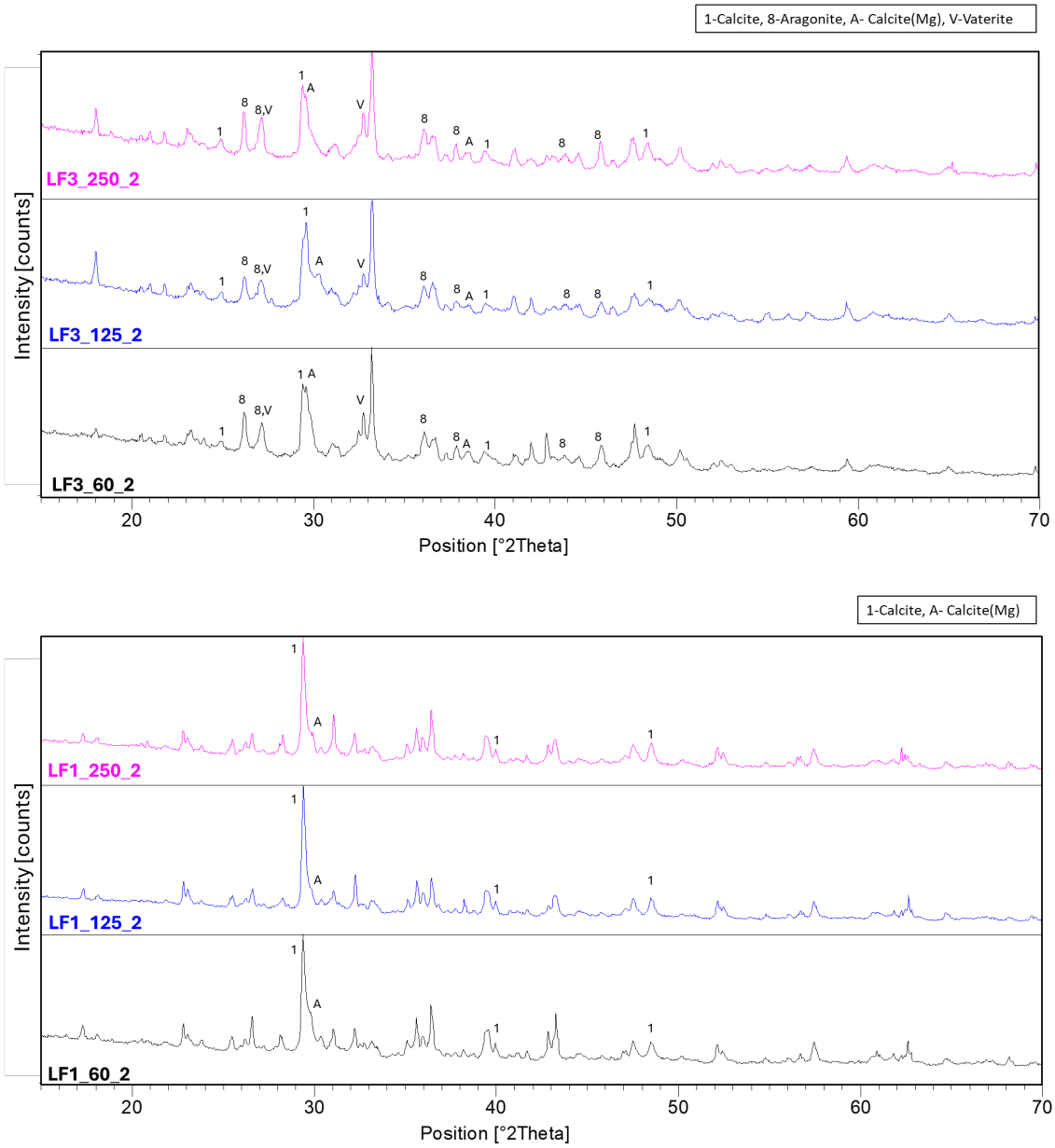

Figure A- 10. XRD pattern of test 2 for LF3 and LF1 at 3 different speed (60, 125 and 250). The formation of carbonated products as calcite (1), vaterite (V), aragonite (8) and calcite-Mg (A) are highlighted. In LF3 samples the formation of all the carbonated phases is evident; whereas in LF1 sample only calcite and calcite-Mg were the main products

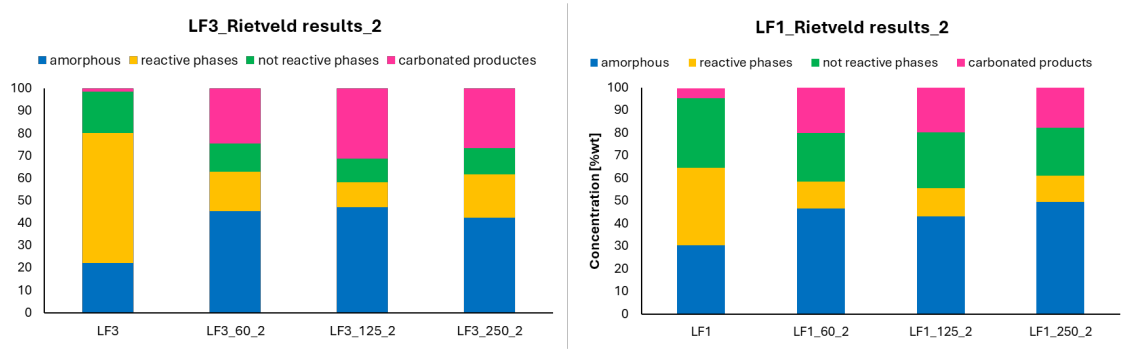

Figure A- 11. Quantitative phase analysis of untreated and carbonated slag samples (LF1 and LF3) obtained by Rietveld refinement. The 4 groups are the sum of mineralogical data obtained by QXRD refinement. The graph illustrates the changes in mineralogical composition following the carbonation process. Mineralogical composition of LF1 and LF3 before and after carbonation by Rietveld method (test 2)

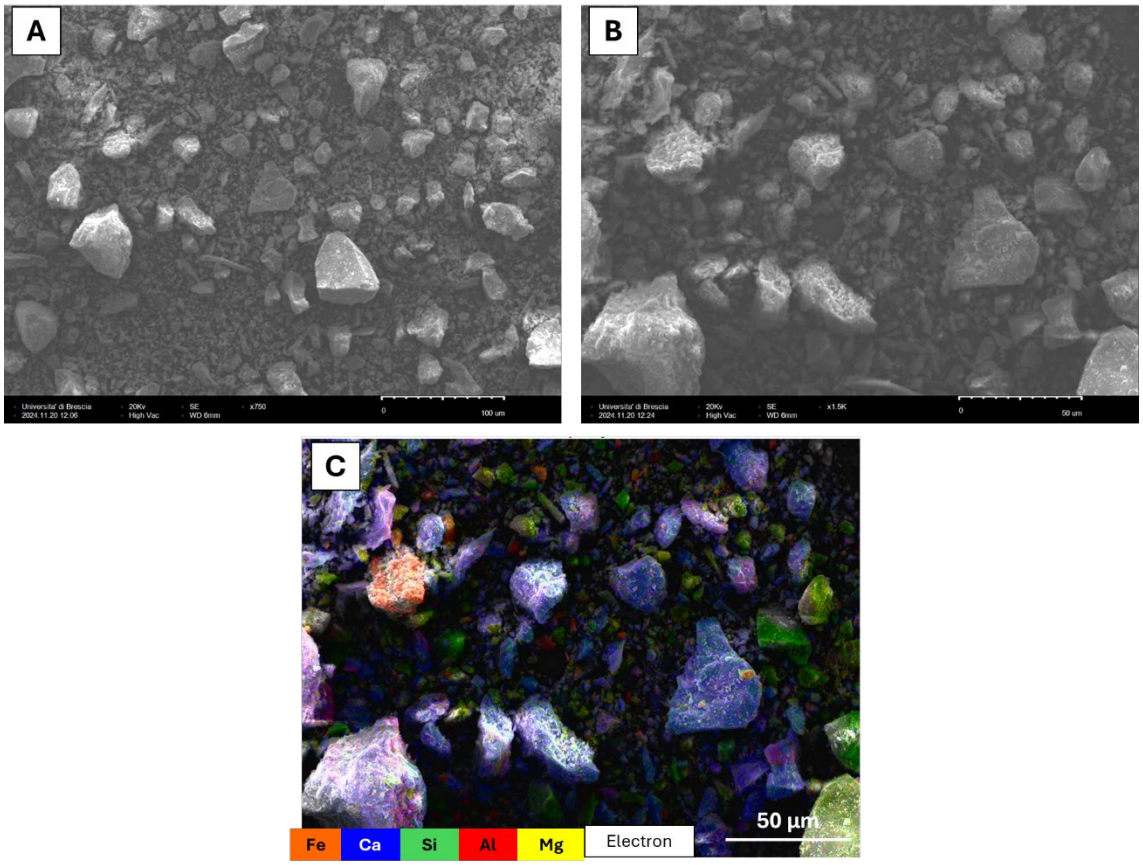

Figure A- 12. SEM images of starting material LF1 at different blows-up (A-B). Backscatter electron images of LF3 (C) plotted with the corresponding element concentration maps. In the composite maps, the saturation of each colour doesn't correspond to the concentration of the element

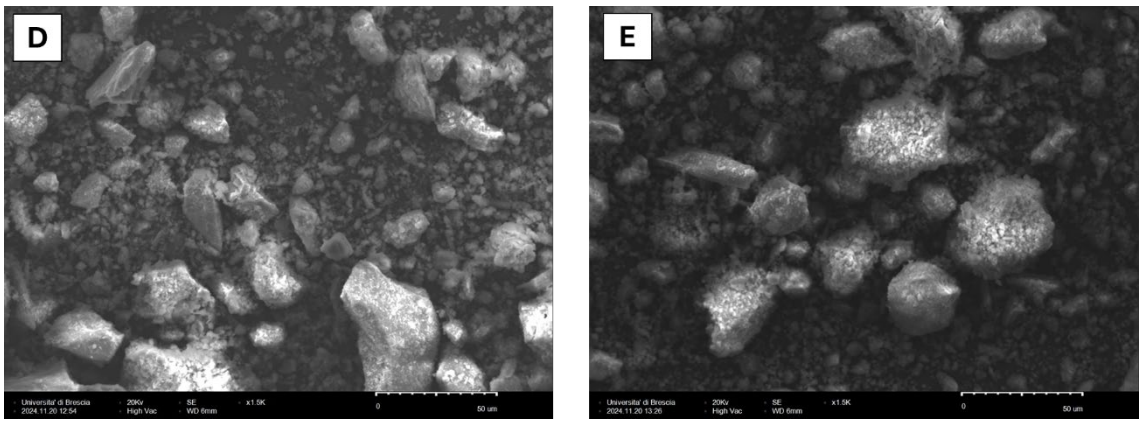

Figure A- 13. SEM images of LF1_60_1 (D) and LF1_250_1 (E). The images underline some changes in the morphology of the samples by using different stirring speed

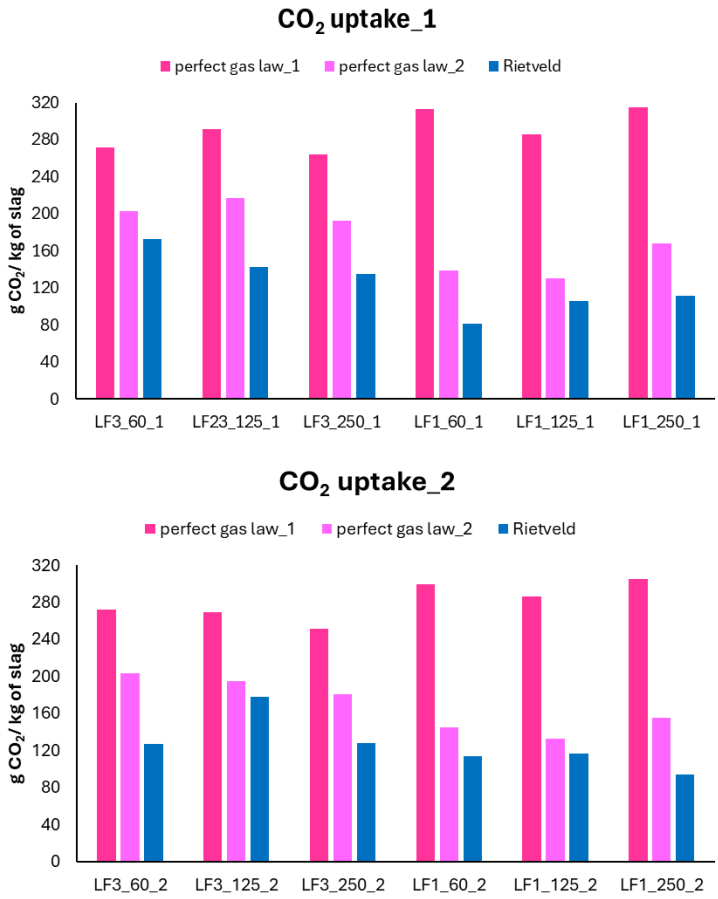

Figure A- 14. CO_2 uptake results for LF1 and LF3, using two approaches: perfect gas law and Rietveld method (test 1 and 2). The graphs underline different results by use of different calculations methods. Rietveld method let only quantify crystalline phase, consequently, the CO_2 uptake is the minor

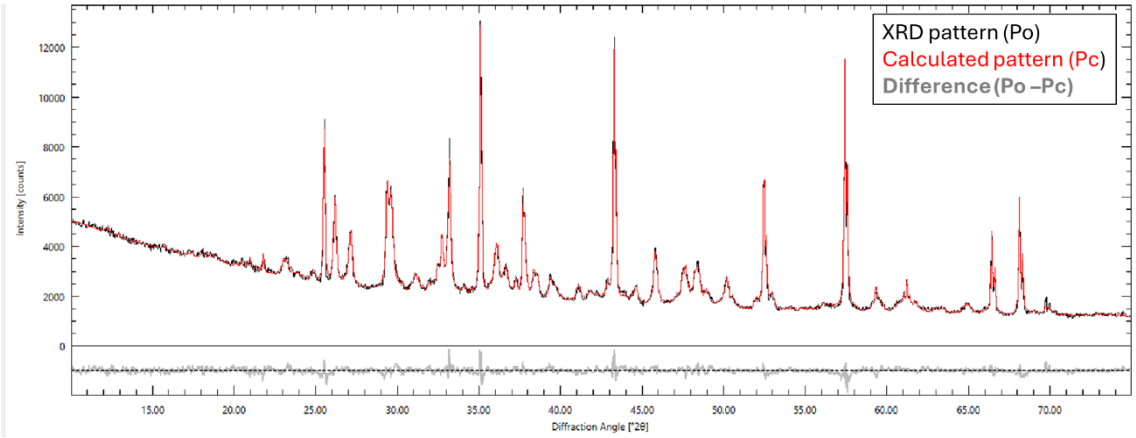

Figure A- 15. Rietveld refinement of LF3_60_1 sample. The picture shows the XRD pattern (Po) (black line), collected by the XRD instrument. The calculated pattern (Pc) (red line) is the pattern fitted by the software based on the crystalline phases inserted for the quantification. The difference line (Po – Pc) (grey line) is the subtraction between the XRD and calculated pattern. The flatter the line, the better is the fit.

7.3 Mild condition environmental carbonation

Table A- 4. Mineralogical composition by QXRD calculation using internal standard method. The table reports the data about LF1 and LF1def at different times: 0, 1 and 2 months and 1 year. The reaction was conducted at room temperature and pression and l/s = 0.7-0.9 ml/g.

Samples	**LF1**				**LF1 def**			
	0m	**1m**	**2m**	**1 year**	**0m**	**1m**	**2m**	**1 year**
	[wt%]	[wt%]	[wt%]	[wt%]	[wt%]	[wt%]	[wt%]	[wt%]
Aluminate	3.1	0.8	1.1	0.9	3.1	1.1	1.0	1.6
Amicite	1.4	1.2	0.3	0.3	0.9	1.4	0.6	0.5
Amorphous	28.4	41.5	44.1	48.9	32.8	42.0	39.2	38.3
Aragonite	-	0.8	0.7	1.5	-	0.3	0.8	1.1
Bredigite	2.7	1.0	2.0	1.3	2.6	1.4	2.8	1.9
Calcite	1.1	5.3	7.0	6.8	1.0	7.6	8.2	7.7
Cuspidine	1.4	1.6	1.7	1.0	1.2	2.3	1.8	1.8
Diopside	4.2	2.5	2.3	3.3	1.8	2.0	3.0	2.6
Dolomite	1.0	0.7	0.4	0.4	1.0	1.0	0.5	0.0
Enstatite	5.7	6.0	4.8	3.3	6.7	4.7	4.4	6.3
Forsterite	12.6	10.3	9.4	7.3	14.2	11.7	11.1	9.8
Gehlenite	2.4	2.0	1.7	1.5	1.1	2.2	3.2	2.1
Hornblende(MgFe)	4.0	3.7	2.0	2.0	1.9	2.4	2.9	2.7
Katoite	2.3	2.4	1.6	1.8	2.3	1.7	1.3	1.7
Mayenite	2.3	0.8	0.5	0.4	3.3	0.8	0.8	0.8
Mullite	1.5	1.3	1.2	0.9	1.5	1.0	1.1	1.4
Periclase	6.9	3.7	4.0	4.5	8.7	5.4	5.4	5.9
Quartz	1.2	1.9	1.7	1.2	1.9	1.3	1.7	1.9
Spinel	1.2	0.9	1.2	0.8	0.6	0.6	0.4	0.5
Vaterite	-	1.8	2.2	3.7	-	0.9	2.1	3.2
β-C_2S	6.8	2.2	4.7	2.2	5.4	2.4	2.7	3.0
γ-C_2S	9.5	7.8	5.6	6.2	8.1	6.3	5.1	5.4
Total	99.6	100.0	100.0	100.0	99.95	100.32	99.99	99.98

Table A- 5. Mineralogical composition by QXRD calculation using internal standard method. The table reports the data about LF2 and LF2def at different times: 0, 1 and 2 months and 1 year. The reaction was conducted at room temperature and pression and l/s = 0.7-0.9 mg/ml

Samples	**LF2**				**LF2 def**			
	[wt%]	[wt%]	[wt%]	[wt%]	[wt%]	[wt%]	[wt%]	[wt%]
	0m	**1m**	**2m**	**1 year**	**0m**	**1m**	**2m**	**1 year**
Alite	3.1	0.4	0.9	-	4.2	-	0.2	0.3
Aluminate	8.0	3.4	2.9	2.5	8.4	3.8	2.6	3.4
Amorphous	19.3	39.4	39.7	44.4	16.7	31.2	33.6	35.8
Aragonite	-	3.2	4.9	4.7	-	2.8	3.1	3.7
Bredigite	2.2	1.6	2.7	2.0	4.7	3.8	3.2	2.2
Calcite	1.1	8.4	8.8	9.9	1.2	7.5	6.2	6.9
Dolomite	0.5	0.1	-	0.4	1.2	0.4	0.6	0.5
Forsterite	1.1	1.6	0.9	0.9	1.9	1.8	1.3	0.9
Gehlenite	5.4	3.3	3.4	2.5	3.6	2.8	2.7	2.9
Hornblende(Mg/Fe)	3.2	4.3	3.3	3.0	2.8	3.1	3.7	2.7
Katoite	6.4	3.4	2.9	2.0	9.6	6.4	5.5	4.6
Maghemite	1.4	1.0	1.2	1.0	-	-	-	-
Mayenite	4.1	1.1	0.6	0.7	4.5	1.1	0.9	0.5
Periclase	6.2	4.4	4.2	3.7	5.6	3.7	3.7	4.0
Tobermorite	1.8	0.9	1.3	0.5	0.8	1.0	1.9	1.7
Vaterite	-	5.6	5.4	7.5	-	8.2	9.5	11.7
Wuestite	6.9	6.1	4.4	4.2	5.0	3.6	3.6	3.2
β-C_2S	19.5	7.2	7.7	5.9	18.3	11.3	11.4	6.5
γ-C_2S	9.7	4.9	5.5	4.2	11.6	7.4	6.5	6.6
Total	100.0	99.9	100.4	99.9	100.0	100.0	100.0	97.9

Table A- 6. Mineralogical composition by QXRD calculation using internal standard method. The table reports the data about AOD1(F) and AOD1(F)def at different times: 0, 1 and 2 months and 1 year. The reaction was conducted at room temperature and pression and l/s = 0.7-0.9 mg/ml

Samples	**AOD1(F)**				**AOD1 (F) def**			
	[wt%]	[wt%]	[wt%]	[wt%]	[wt%]	[wt%]	[wt%]	[wt%]
	0m	**1m**	**2m**	**1 year**	**0m**	**1m**	**2m**	**1 year**
Akermanite	0.3	0.1	0.3	0.6	1.0	0.6	0.6	0.6
Alite	1.2	-	2.6	0.2	1.2	0.6	0.6	-
Aluminate	3.3	2.0	-	2.0	3.7	2.1	1.7	1.7
Amorphous	15.0	30.0	37.4	39.0	12.4	25.1	32.5	29.1
Andradite	4.0	4.2	1.6	1.5	2.9	3.3	2.3	1.8
aragonite	-	0.3	0.2	1.5	0.0	1.4	0.3	0.9
Bredigite	18.8	14.6	13.7	15.7	26.4	21.5	20.0	18.7
Calcite	0.2	1.7	2.6	3.0	0.3	1.5	3.2	1.3
Cuspidine	11.6	8.0	7.8	6.0	12.0	8.7	10.0	9.3
Diopside	3.6	3.2	0.5	2.9	1.9	2.4	0.4	1.9
Dolomite	0.5	0.3	2.0	0.3	-	0.1	0.4	0.2
Enstatite	2.4	2.4	3.7	0.7	2.8	1.3	0.5	1.3
Gehlenite	3.6	3.2	-	3.8	3.1	3.1	2.1	3.8
Mayenite	5.2	0.5	1.0	0.5	5.7	0.4	1.0	1.0
Merwinite	5.2	3.6	4.5	2.4	3.2	4.1	4.2	3.9
Periclase	3.7	3.4	3.7	3.3	4.6	4.9	3.6	4.4
Spinel	3.2	2.6	2.8	2.2	3.4	3.0	2.6	3.0
Vaterite	-	6.3	6.7	5.3	-	2.8	3.0	6.4
Wuestite	0.6	0.5	0.5	0.3	0.5	0.2	0.4	0.2
α-C_2S	1.0	0.8	1.0	-	0.7	0.4	-	-
β-C_2S	16.1	7.8	5.2	6.7	11.6	9.6	8.0	8.4
γ-C_2S	1.1	1.7	-	2.1	2.6	3.0	1.8	2.2
Total	100.4	97.3	97.6	100.0	100.0	100.0	99.2	100.0

Table A- 7. Mineralogical composition by QXRD calculation using internal standard method. The table reports the data about AOD1(M) and AOD1(M)def at different times: 0, 1 and 2 months and 1 year. The reaction was conducted at room temperature and pression and l/s = 0.7-0.9 mg/ml

Samples	**AOD1 (M)**				**AOD1 (M) def**			
	[wt%]	[wt%]	[wt%]	[wt%]	[wt%]	[wt%]	[wt%]	[wt%]
	0m	**1m**	**2m**	**1 year**	**0m**	**1m**	**2m**	**1 year**
Akermanite	2.1	1.4	2.0	2.4	1.5	1.7	1.3	2.1
Alite	1.0	1.2	-	-	2.0	1.0	-	0.3
Aluminate	1.4	1.3	0.5	0.7	1.7	1.3	1.2	1.0
Amorphous	25.4	41.8	45.0	41.6	21.4	49.0	41.3	48.5
Andradite	2.0	1.7	0.9	1.8	2.7	1.4	1.7	2.0
Aragonite		1.1	1.5	3.0	-	1.4	2.5	3.0
Bredigite	13.1	8.2	9.4	7.3	13.4	8.8	9.9	6.0
Calcite	1.4	6.4	5.9	8.0	0.8	4.8	5.4	6.5
Cuspidine	6.3	5.2	3.5	3.2	7.7	7.5	4.1	6.5
Enstatite	5.8	3.6	2.9	3.1	4.8	2.5	2.4	1.7
Forsterite	3.6	3.6	2.4	2.1	3.6	2.0	3.9	3.3
Grossular	0.3	0.3	0.3	0.6	0.5	1.2	0.4	0.2
Katoite	2.4	4.5	3.9	4.3	3.1	3.5	3.8	2.9
Mayenite	5.1	0.9	0.7	0.8	4.9	0.9	1.0	0.5
Periclase	5.7	5.3	5.0	3.7	6.3	3.3	4.9	3.9
Portlandite	0.6	0.1	-	-	0.4	-	-	-
Quartz	0.4	0.3	0.3	1.9	0.4	0.4	0.4	0.4
Spinel	1.3	0.2	1.4	1.2	1.8	1.2	1.1	0.8
Vaterite	-	0.3	0.6	1.9	-	0.2	0.6	0.6
α-C_2S	0.4	0.4	0.4	-	1.0	5.1	-	1.0
β-C_2S	15.7	7.3	7.7	8.3	16.4	-	8.7	5.5
γ-C_2S	5.5	5.3	6.1	4.5	5.6	3.6	6.2	3.7
					1.5	1.7	1.3	2.1
Total	99.4	100.0	100.0	100.2	100.0	100.5	100.6	100.4

Table A- 8. Mineralogical composition by QXRD calculation using internal standard method. The table reports the data about EAF1 and EAF1def at different times: 0, 1 and 2 months and 1 year. The reaction was conducted at room temperature and pression and l/s = 0.7-0.9 mg/ml

Samples	**EAF1**				**EAF1 def**			
	[wt%]	[wt%]	[wt%]	[wt%]	[wt%]	[wt%]	[wt%]	[wt%]
	0m	**1m**	**2m**	**1 year**	**0m**	**1m**	**2m**	**1 year**
Amorphous	20.8	42.3	45.4	47.4	31.3	34.8	40.2	41.8
Brownmillerite	9.9	3.5	5.2	3.0	6.0	5.4	5.3	4.7
Calcite	-	0.9	1.8	2.1	-	0.9	1.4	1.8
Chromite	6.0	4.6	4.9	4.4	4.9	4.6	4.6	4.3
Gehlenite	4.6	4.2	3.8	3.5	3.7	4.5	3.6	3.3
Hausmannite	0.8	1.0	1.0	1.5	0.6	1.3	1.3	1.0
Magnetite	1.5	2.3	1.6	1.6	-	-	-	-
Mayenite	1.3	-	-	-	1.4	0.4	-	-
Merwinite	3.1	4.9	1.4	4.1	3.3	5.0	3.3	3.1
Periclase	0.8	0.9	0.8	0.6	0.7	0.6	0.9	1.7
Wuestite	28.1	21.1	19.9	19.0	24.9	23.2	22.3	22.2
β-C_2S	20.6	11.3	12.2	9.8	21.0	14.0	14.2	13.5
γ-C_2S	2.5	3.1	2.0	3.1	2.9	3.8	2.4	2.6
Total	100.0	100.0	100.0	100.0	100.7	98.5	99.5	100.0

Table A- 9. Mineralogical composition by QXRD calculation using internal standard method. The table reports the data about EAF2 and EAF2def at different times: 0, 1 and 2 months and 1 year. The reaction was conducted at room temperature and pression and l/s = 0.7-0.9 mg/ml

Samples	**EAF2**				**EAF2 def**			
	[wt%]	[wt%]	[wt%]	[wt%]	[wt%]	[wt%]	[wt%]	[wt%]
	0m	**1m**	**2m**	**1 year**	**0m**	**1m**	**2m**	**1 year**
Amorphous	39.4	35.2	36.4	41.6	34.7	35.4	44.6	41.7
Bredigite	7.1	4.5	6.0	4.8	6.7	5.0	4.3	4.2
Calcite	-	1.7	2.1	3.4	-	1.4	1.3	1.9
Chromite	3.2	3.2	3.1	2.6	3.5	4.8	4.7	2.5
Gehlenite	8.2	7.8	8.5	7.4	10.4	10.9	8.9	8.7
Magnetite	4.0	4.1	3.7	2.9	2.1	1.6	1.3	1.5
Merwinite	3.2	4.7	3.3	2.8	4.3	4.9	3.6	3.0
Wuestite	20.4	24.5	23.7	23.3	24.3	25.0	20.4	22.3
β-C_2S	13.2	9.0	8.0	9.2	13.1	12.4	10.4	12.3
γ-C_2S	2.1	3.2	2.4	2.1	1.0	0.9	0.7	2.0
Total	100.8	97.7	97.1	100.0	100.0	102.3	100.0	100.0

Table A- 10. Mineralogical composition by QXRD calculation using internal standard method. The table reports the data about BF5 and BF5def at different times: 0, 1 and 2 months and 1 year. The reaction was conducted at room temperature and pression and l/s = 0.7-0.9 mg/ml

Samples	**BF5**				**BF5 def**			
	[wt%]	[wt%]	[wt%]	[wt%]	[wt%]	[wt%]	[wt%]	[wt%]
	0m	**1m**	**2m**	**1 year**	**0m**	**1m**	**2m**	**1 year**
Alite	6.3	1.8	1.5	-	2.0	1.3	2.0	1.4
Amorphous	76.6	70.7	65.4	66.7	81.0	65.9	64.5	60.1
Aragonite	-	12.0	15.5	16.4	-	13.6	14.9	16.6
Calcite	-	4.0	3.8	3.4	-	5.4	4.6	5.7
CaO	1.2	0.2	-	-	1.8	-	-	-
Merwinite	5.7	1.8	2.6	0.5	3.0	1.8	2.2	2.2
Periclase	3.4	1.7	1.6	1.9	3.5	2.3	2.5	1.8
Portlandite	1.3	0.4	0.5	0.6	3.6	0.5	0.4	0.4
Vatertite	-	4.9	5.7	9.4	-	6.4	7.0	9.5
α-C_2S	5.6	2.5	2.9	2.4	4.0	2.9	1.9	2.2
Total	100.0	100.0	99.5	101.3	98.9	100.0	100.0	100.0

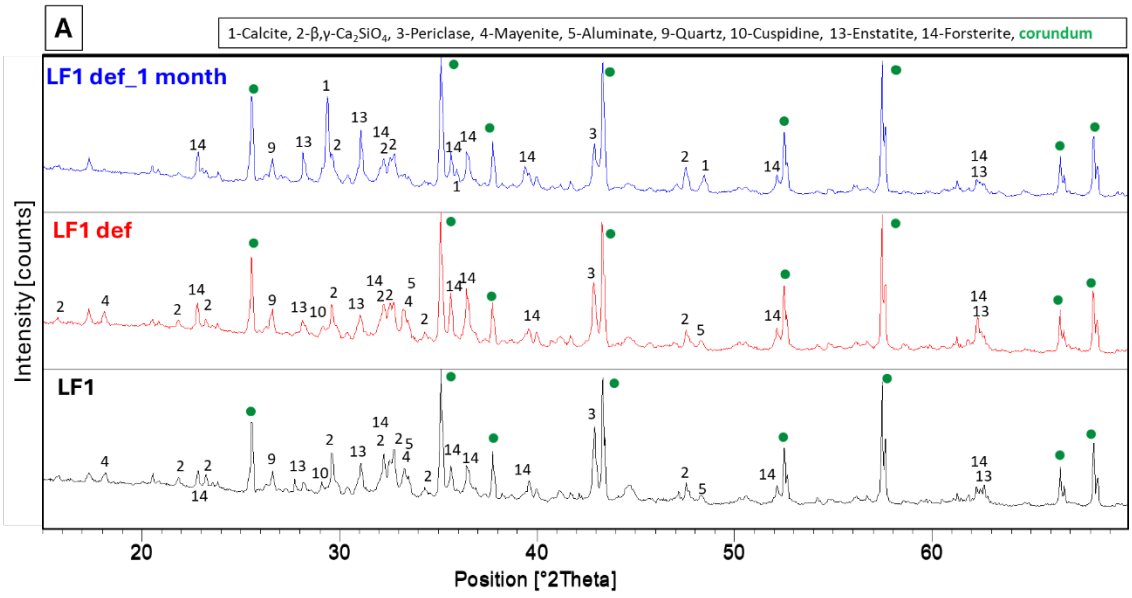

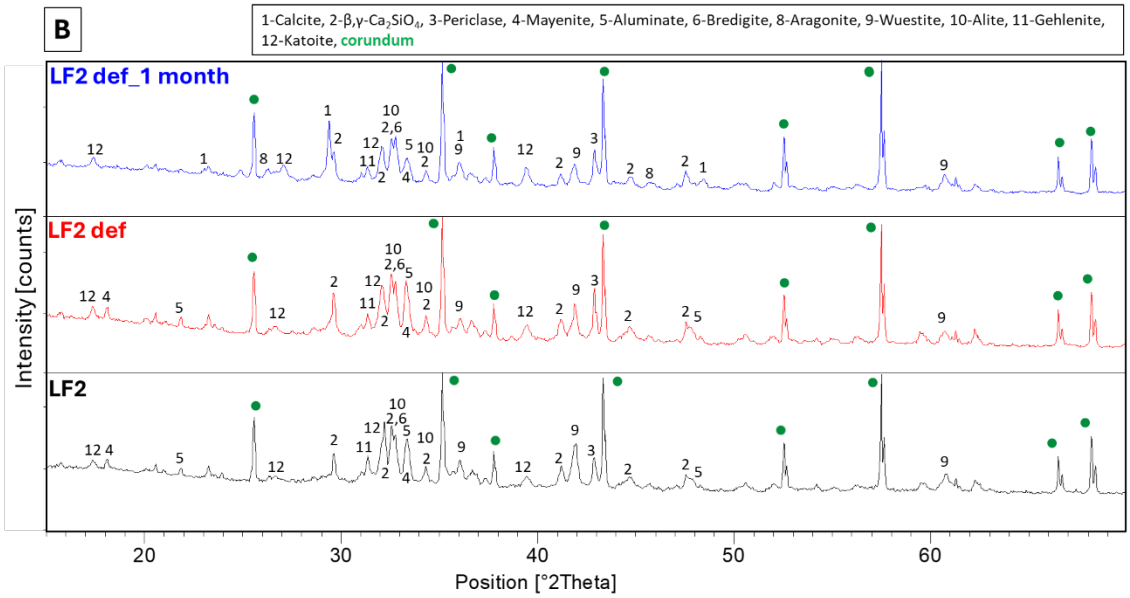
B
1-Calcite, 2-β,γ-Ca2SiO4, 3-Periclase, 4-Mayenite, 5-Aluminate, 6-Bredigite, 8-Aragonite, 9-Wuestite, 10-Alite, 11-Gehlenite, 12-Katoite, corundum
LF2 def_1 month
LF2 def
LF2
Intensity [counts]
20
30
40
50
60
Position [°2Theta]

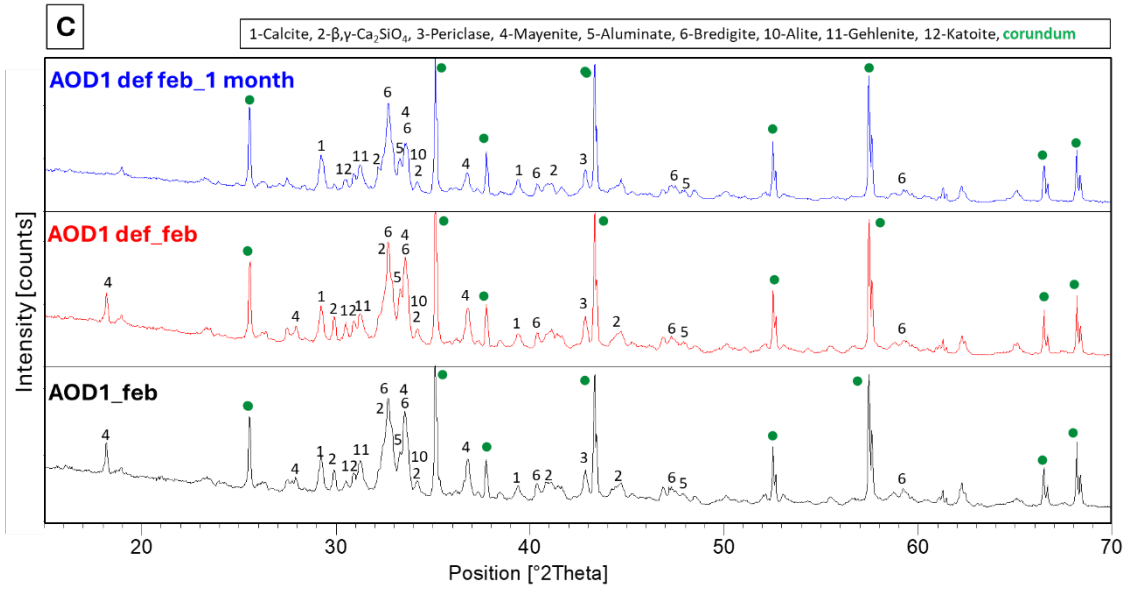
C
1-Calcite, 2-β,γ-Ca2SiO4, 3-Periclase, 4-Mayenite, 5-Aluminate, 6-Bredigite, 10-Alite, 11-Gehlenite, 12-Katoite, corundum
AOD1 def feb_1 month
AOD1 def_feb
AOD1_feb
Intensity [counts]
20
30
40
50
60
70
Position [°2Theta]

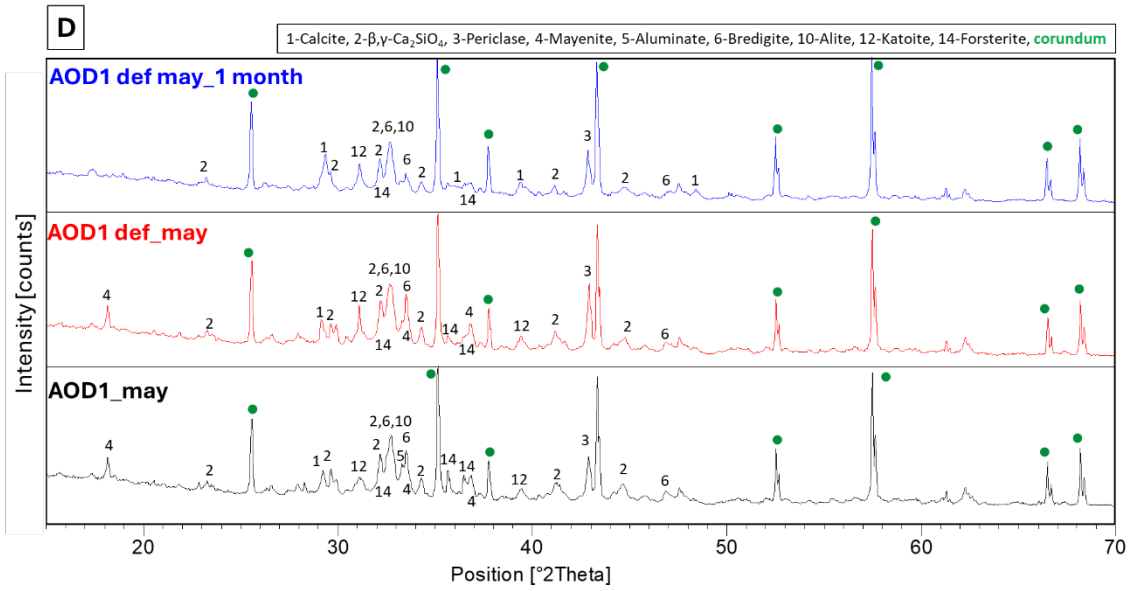
D
1-Calcite, 2-β,γ-Ca2SiO4, 3-Periclase, 4-Mayenite, 5-Aluminate, 6-Bredigite, 10-Alite, 12-Katoite, 14-Forsterite, corundum
AOD1 def may_1 month
AOD1 def_may
AOD1_may
Intensity [counts]
20
30
40
50
60
70
Position [°2Theta]

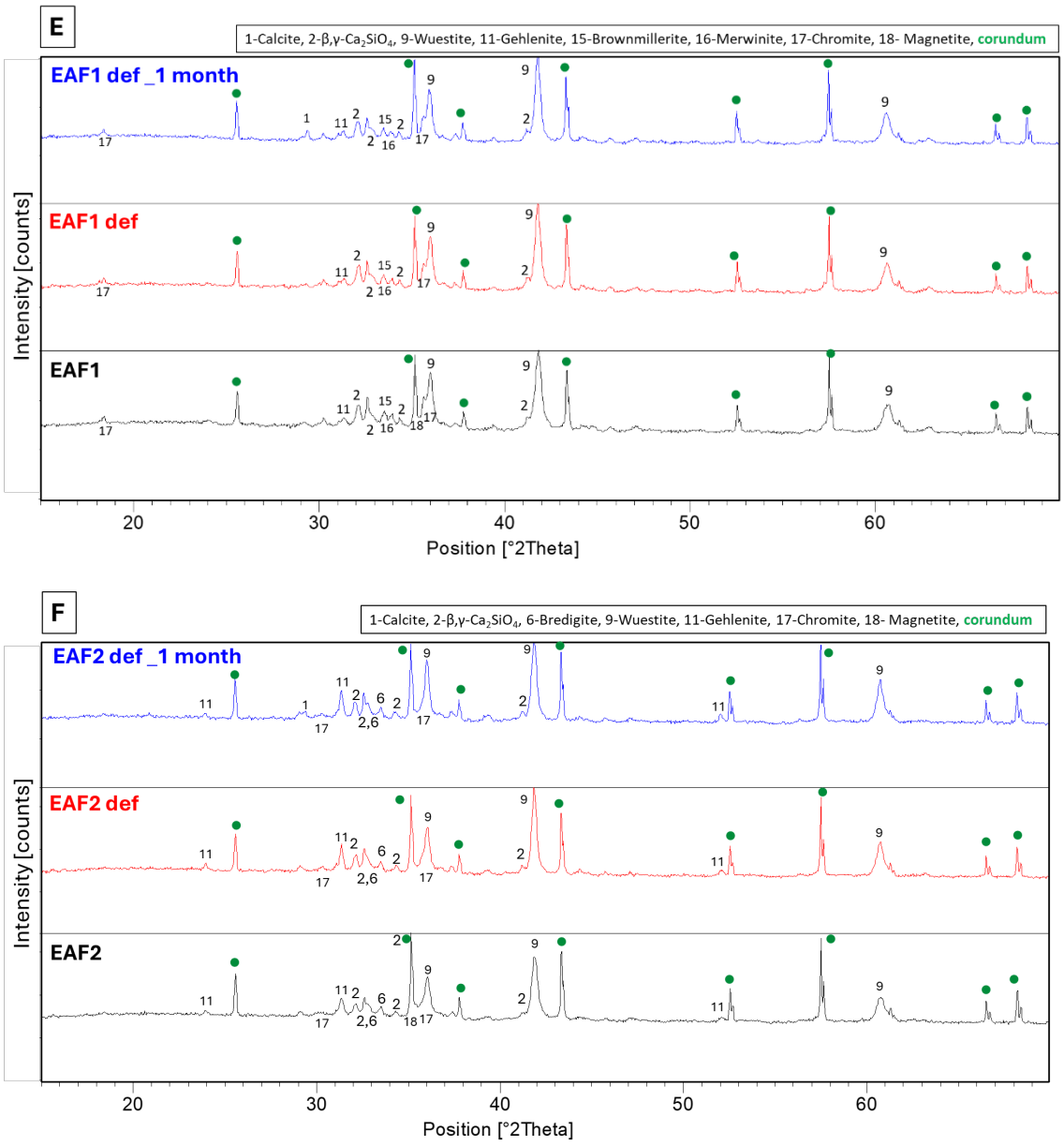

Figure A- 16. XRD pattern of starting materials and carbonated def slag after 1 month: LF1 (A), LF2 (B), AOD1-F (C), AOD1-M (D), EAF1 (E) and EAF2 (F). The corundum is used as external std and it is represented by the dot

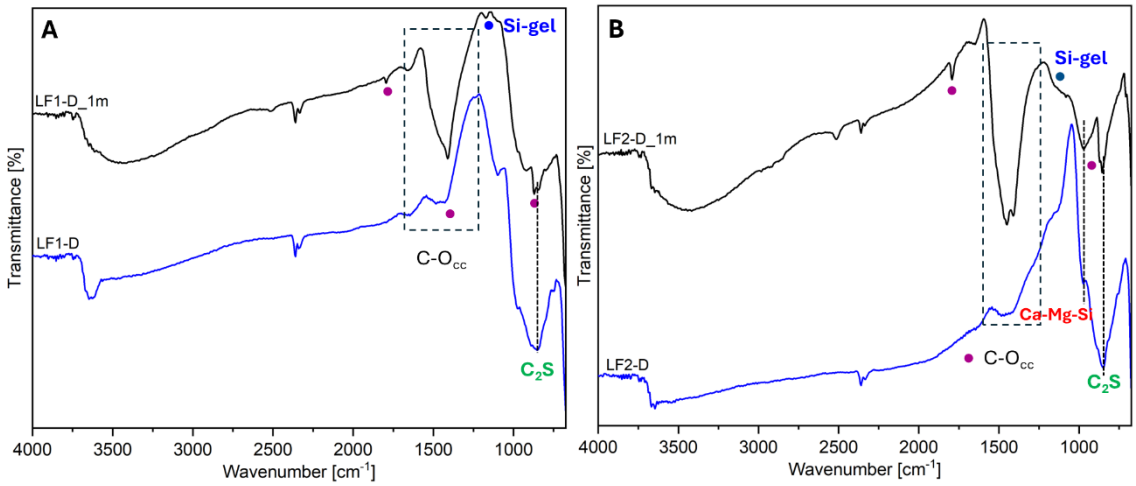

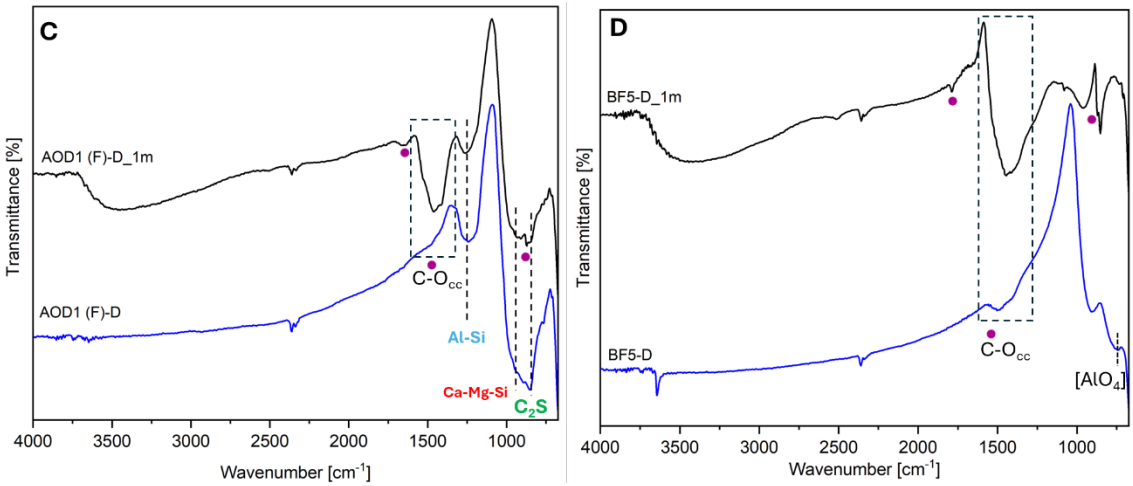

Figure A- 17. FT-IR spectra of starting materials in comparison with corresponding carbonated products. The large band is due to the moisture inside the sample

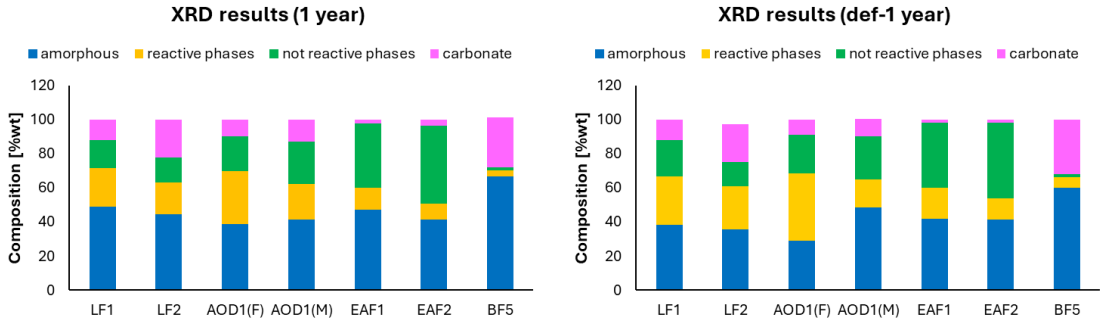

Figure A- 18. Quantitative phase analysis of carbonated slag (untreated and iron-removed) samples obtained by Rietveld refinement. The graph illustrates not main differences in mineralogical composition despite of the dry Fe removal process (exposure time = 1 year)

7.4 Enforced carbonation

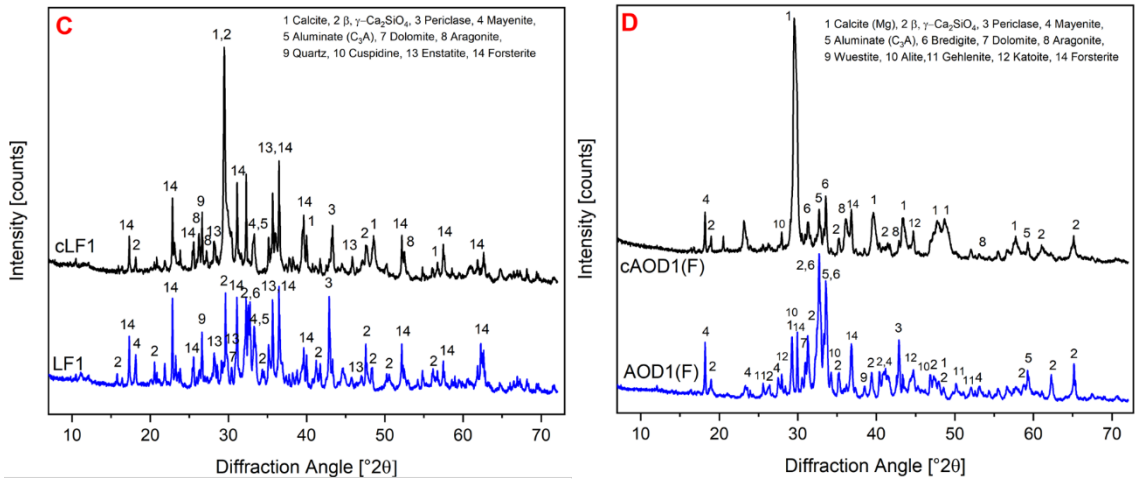

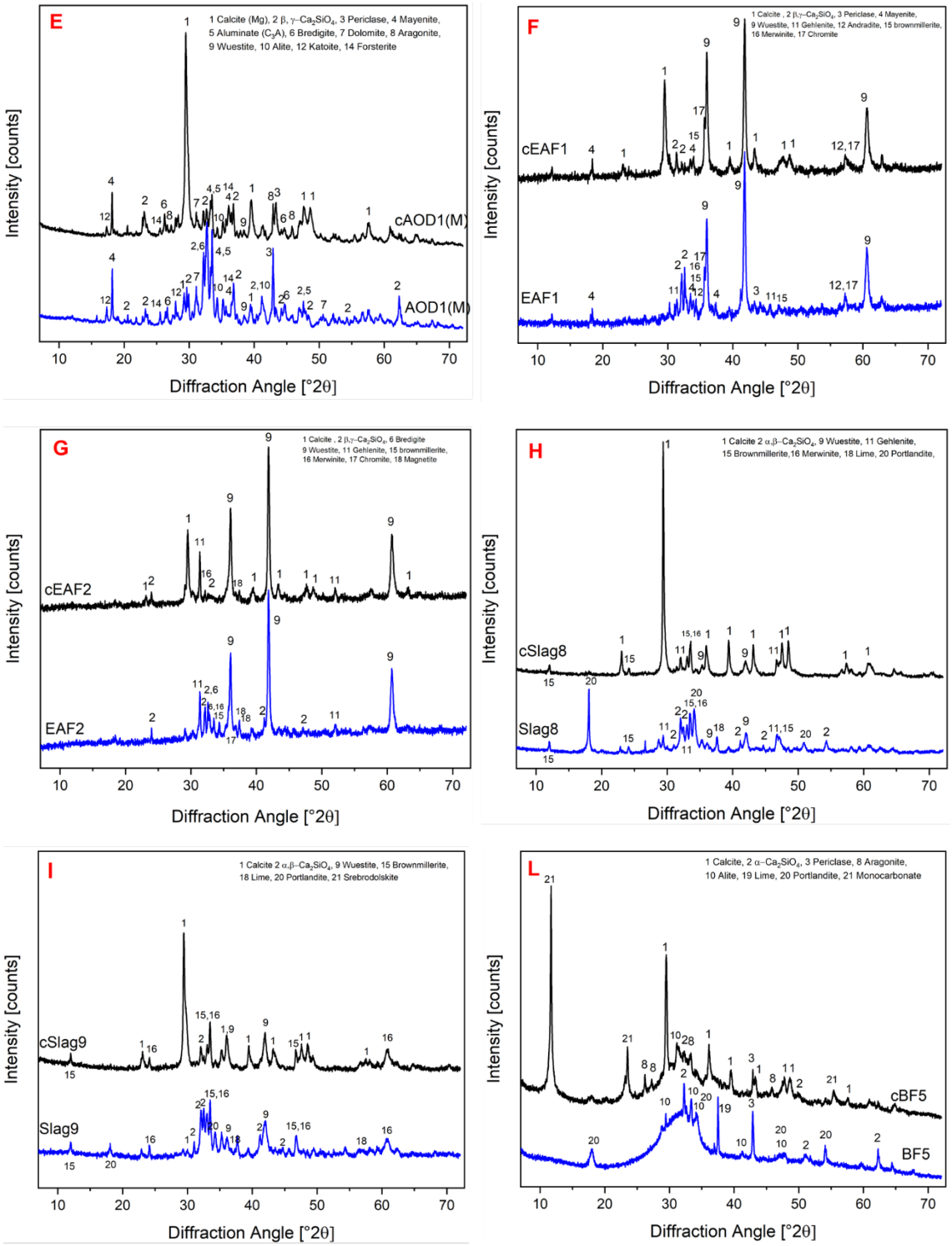

Figure A- 19. Comparison of XRD pattern of steel slags before and after carbonation, highlighting the phase transformations and mineralogical changes induced by the carbonation process. The mineralogical phases are reported in the figure, and they are numbered. The samples represent are LF1 (C), AOD1-F (D), AOD1-M (E), EAF1 (F), EAF2 (G), Slag8 (H), Slag9 (I) and BF5 (L)

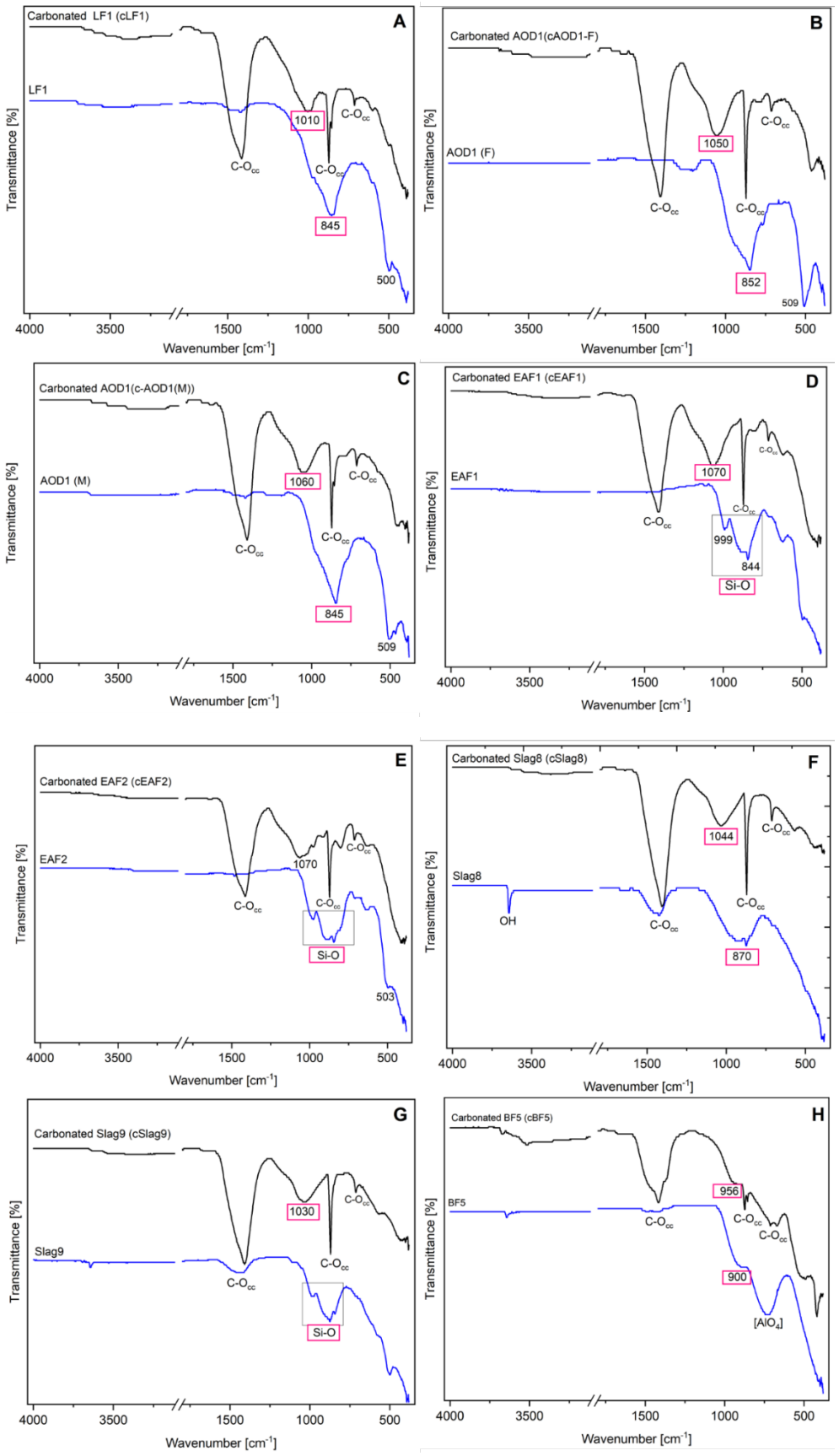

Figure A- 20. Ft-IR spectra for starting materials and relative carbonated products: LF1 (A), AOD1-F (B), AOD1-M (C), EAF1 (D), EAF2 (E), Slag8 (F), Slag9 (G) and BF5 (H), highlighting the formation of carbonate bond and silica-gel

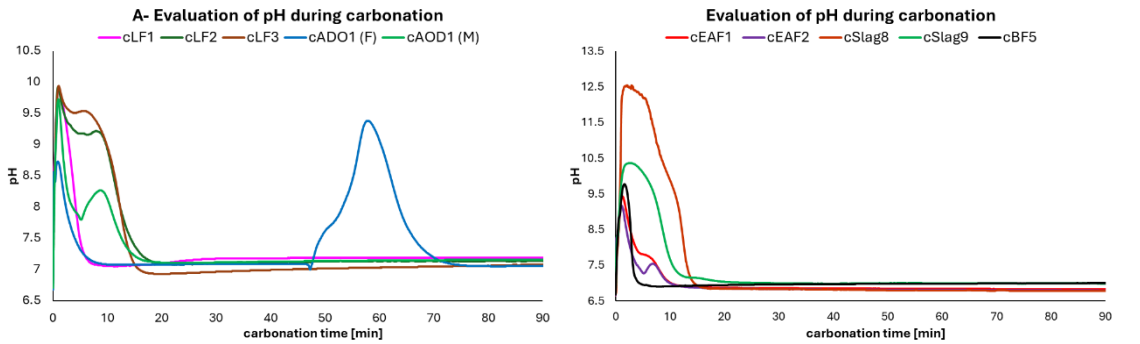

Figure A- 21. pH evolution during carbonation in the enforced carbonation process

Table A- 11. Mineralogical composition of carbonated steel slag by XRD quantification. The carbonation process was conducted at room pressure and temperature, 6 hours and 100% CO_2. The quantification method used is Rietveld by external standard. The estimated error of QXRD measurement is ± 1 % [60].

Samples	cLF1 [wt%]	cLF2 [wt%]	cLF3 [wt%]	cAOD1(F) [wt%]	cADO1M [wt%]	cEAF1 [wt%]	cEAF2 [wt%]	cSlag8 [wt%]	cSlag9 [wt%]	cBF5 [wt%]
Akermanite	-	-	1.8	0.2	1.2	-	-	1.1	-	-
Alite	-	1.5	-	0.3	-	-	-	-	-	0.3
Aluminate	1.8	7.1	11.6	-	1.3	-	-	-	-	-
Amicite	0.5	-	-	-	-	-	-	-	-	-
Amorphous	34.5	33.2	32.4	28.2	36.9	27.9	28.2	30.1	37.7	76.6
Andradite	-	-	2.2	2.1	-	-	-	-	-	-
Aragonite	4.5	4.4	1.8	0.6	4.3	-	-	-	-	2.7
Augite	-	-	-	1.1	-	-	-	-	-	-
Bredigite	-	-	-	7.9	2.0	-	-	-	-	-
Brownmillerite	-	-	1.8	-	-	4.8	-	3.1	-	-
calcite	14.3	26.8	21.8	24.2	29.4	24.5	17.9	46.4	31.2	7.7
Calcite(Mg)	-	-	-	16.8	-	-	-	-	-	-
Chromite	-	-	-	-	-	6.0	2.6	-	-	-
Corundum	2.9	-	-	1.2	1.3	-	-	-	-	-
Cuspidine	1.3	-	-	1.0	0.3	-	-	-	-	-
Diopside	1.7	-	-	1.9	-	-	-	-	-	-
Dolomite	-	9.0	3.0	0.7	1.0	-	-	0.8	-	-
Enstatite	8.9	-	-	-	5.9	-	-	-	-	-
Forsterite	15.2	2.4	0.3	-	2.3	-	-	-	-	-
Gehlenite	1.9	3.1	2.2	-	-	4.3	13.5	-	-	-
Hausmannite	-	-	0.2	-	-	0.6	-	-	-	-
Hauyne	-	-	0.5	-	-	-	-	-	-	-
Hercynite	-	-	0.2	-	-	-	-	-	-	-
Hornblende (Mg/Fe)	1.4	1.4	-	-	-	-	-	-	-	-
Kaolinite	-	-	0.3	-	-	-	-	-	-	-
Katoite	-	4.2	2.3	-	0.6	-	-	-	-	-
Magnetite	-	-	0.2	-	-	0.4	1.4	1.3	2.9	-
Mayenite	0.5	1.6	8.9	2.7	3.6	0.7	-	-	-	-
Merwinite	-	-	-	-	1.8	1.8	3.6	1.4	-	0.5
Monocarbonate	-	-	-	-	-	-	-	-	-	11.5
monohydrocalcite	0.4	-	-	1.4	0.6	-	-	-	-	-

Monticellite	-	-	0.7	-	-	-	-	-	-	-
Mullite	2.3	-	-	-	-	-	-	-	-	-
Periclase	0.4	1.0	1.2	0.5	1.4	0.4	-	-	-	0.3
Quartz	1.8	-	-	-	0.5	-	-	0.2	0.2	-
Spinel	1.2	-	-	4.6	1.6	-	-	-	-	-
Srebrodolskite	-	-	-	-	-	-	-	7.4	12.7	-
tobermorite	-	-	-	-	-	26.9	28.6	-	-	-
wuestite	-	2.3	0.8	-	-	-	-	3.8	10.7	0.1
α-C_2S	-	-	-	2.4	2.1	-	-	0.6	-	-
β-C_2S	1.7	2.0	2.8	0.8	3.4	1.6	4.3	4.7	3.1	-
γ-C_2S	1.5	-	2.7	-	-	-	-	-	-	-
Total	100.0	99.9	100.0	98.5	101.4	100.0	100.0	100.9	98.5	100.0

7.5 Cement Performance

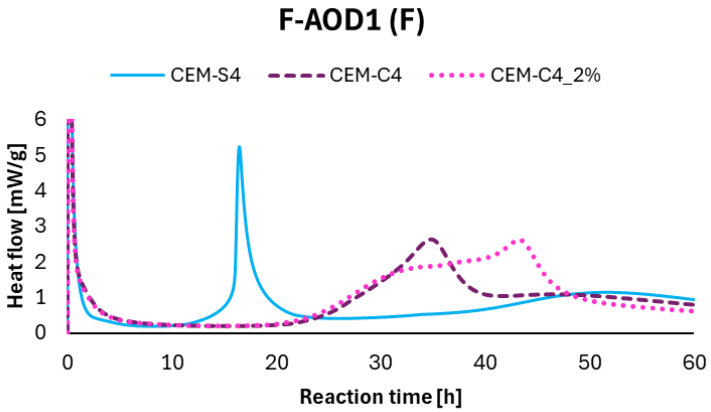

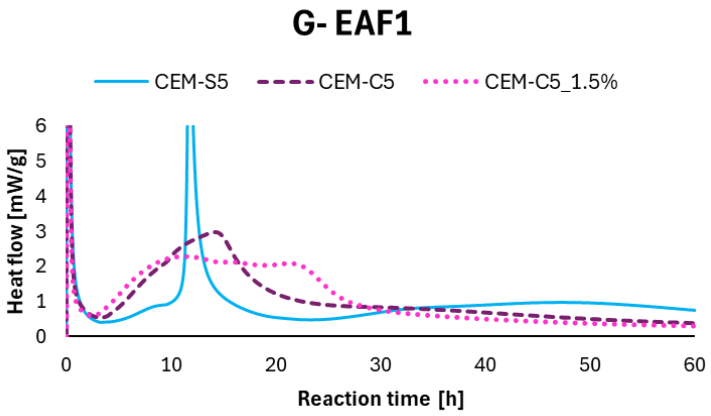

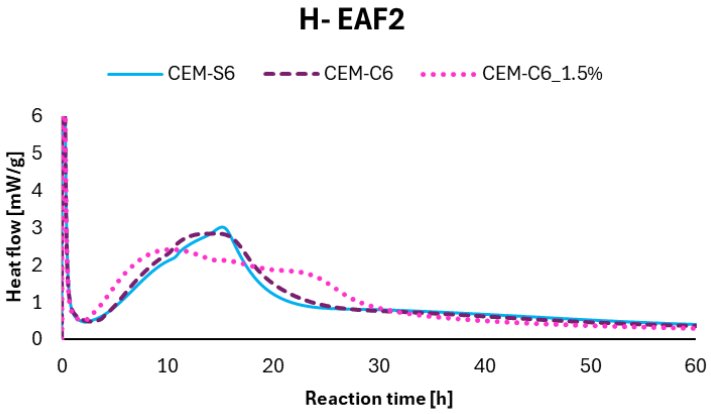

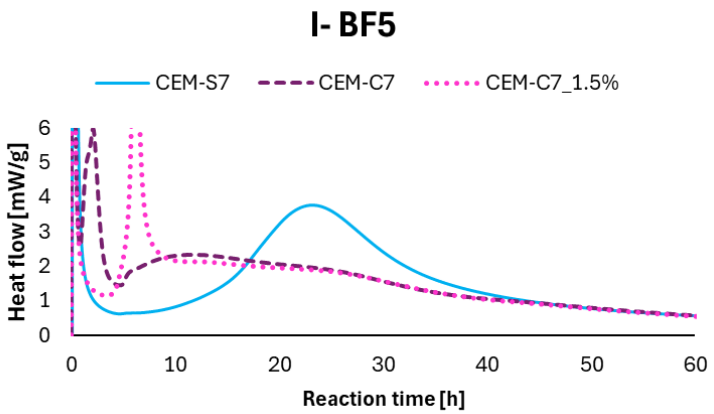

Figure A- 22. Calorimetry test results of composite cements (w/c = 0.5, 60% CEM, 40% slag/limestone and additives). The kinetic of the hydration cement reaction is compared between the reference mixes (CEM and CEM-L) and the slag mixes, underlining the necessity to optimize the composite cements by the addition of accelerators. AOD1(F), EAF1, EAF2 and BF5 mixes are reported respectively in figure F, G, H and I. In CEM-C4 2% of HH was added, in other cases 1.5% of hemihydrate (HH) was added.

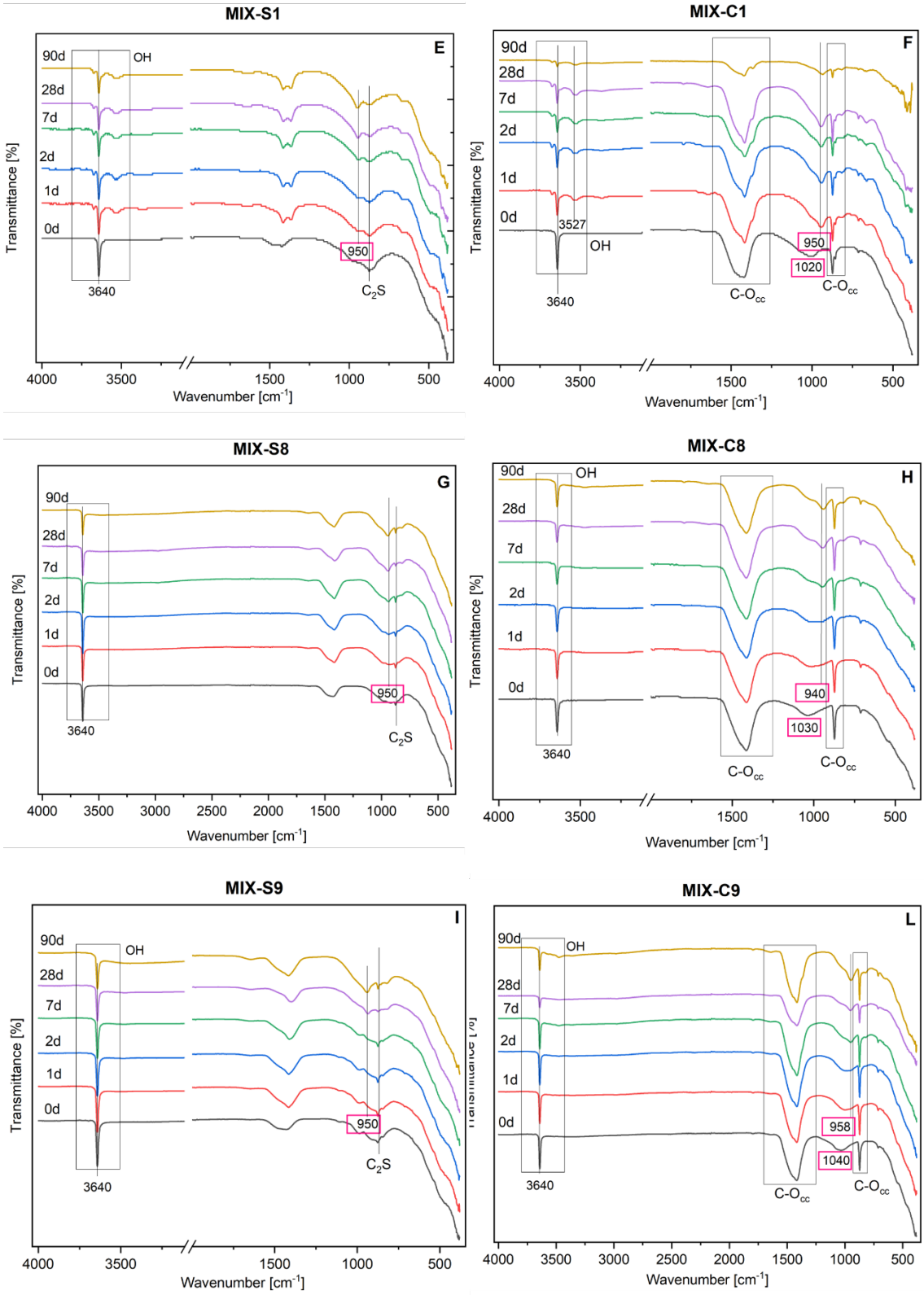

Figure A- 23. Ft-IR spectra of portlandite blends with starting materials and relative carbonated products: LF1 and cLF1 (E-F), Slag8 and cSlag8 (G-H), Slag9 and cSlag9 (I-L), underling the formation of C-S-H product especially in carbonated by-products blends from 0 and 90 days

Table A- 12. Mineralogical phases used in XRD refinement. Each phase is characterized by the chemical formula, the reference code form COD database and the by-product which is referred

Mineralogical phases	Chemical formula	Reference code	Industrial waste
Albite	$NaAlSi_3O_8$	00-009-0466	CKD
Aluminate	Ca_3Al2O_6	00-901-4359	LF1, LF2, LF3, AOD1 (F) (M)
Aragonite	$CaCO_3$	00-041-1475	AOD_1, LF_2
Bredigite	$Ca_{1.7}Mg_{0.3}SiO_4$	00-035-0260	AOD1 (M) (F), LF1, LF2, LF3, EAF1, EAF2
Brownmillerite	$Ca_2(Al,Fe)_2O_5$	00-030-0226	EAF_1, LF3, Slag8
Brucite	$Mg(OH)_2$	01-074-2220	LF_2
Calcite	$CaCO_3$	01-080-0941	All samples
Calcite monohydrate	$CaCO_3*H_2O$	01-084-0049	EAF_2+SiO_2
Cuspidine	$Ca_4Si_2O_7H_2$	00-901-4740	LF1, AOD1(M) (F)
Diopside	CaMgSi2O6	00-100-0007	LF1, AOD1 (F)
Dolomite	$CaMg(CO_3)_2$	01-075-1710	AOD_1
Forsterite	Mg_2SiO_4	00-900-0267	LF1, LF2, LF3, AOD1(M), EAF1, EAF2, Slag8
Garnet	$Ca_{1.92}Fe_{3.08}O_{12}Si_3$	01-082-1552	AOD_1
Gehlenite	$Ca_2Al_2SiO_7$	00-020-0199	AOD_1, LF_2, LF1, AOD1 (F)
Gehlenite	$Ca_2Al_2SiO_7$	00-009-0216	EAF_2, EAF_2+SiO_2
Hydrogarnet	$Ca_3Al_2(H_4O_4)_3$	01-084-1353	LF_2
Iron oxide/wuestite	$Fe_{0.974}O$	01-073-2143	LF_2, EAF_2, EAF_2+SiO_2
Lime	CaO	01-082-1690	CKD, Slag8, Slag9, BF5
α-C_2S	Ca_2SiO_4	00-033-0302	AOD1 (F), AOD1 (M), Slag8, Slag 9, BF5
β-C_2S	Ca_2SiO_4	00-029-0369	All slags except BF5
γ-C_2S	Ca_2SiO_4	00-020-0237	LF1, LF2, LF3, AOD1 (F) (M)
Maghemite	Fe_2O_3	00-025-1402	EAF_1
Magnetite	Fe_3O_4	01-079-0418	EAF_1, EAF_2, EAF_2+SiO_2
Magnetite	Fe_3O_4	01-072-2303	EAF_3+SiO_2
Mayenite	$Ca_{12}Al_{14}O_{33}$	00-009-0413	AOD1 (F) (M), LF1, LF2, LF3, EAF1, EAF2
Olivine	Ca_2SiO_4	01-080-0941	LF_2
Periclase	MgO	01-036-0678	AOD1 (F) (M), LF1, LF2, LF3, EAF1
Portlandite	$Ca(OH)_2$	00-044-1481	AOD_1, EAF_1
Quartz	SiO_2	00-046-1045	CKD
Quartz	SiO_2	01-079-19-06	LF_2
Srebrodolskite	$Ca_2Fe_2O_5$	01-074-1860	EAF_2, EAF_2+SiO_2
Wuestite	FeO	01-077-2355	EAF_1, Slag8, Slag9
Yoshiokaite	$Ca_2(Al,Si)_2O_4$	00-046-1336	EAF_2, EAF_2+SiO_2

BIBLIOGRAPHY

[1] S.-Y. Pan, E.E. Chang, P.-C. Chiang, CO2 Capture by Accelerated Carbonation of Alkaline Wastes: A Review on Its Principles and Applications, Aerosol Air Qual Res 12 (2012) 770–791. https://doi.org/10.4209/aaqr.2012.06.0149.

[2] W. Liu, L. Teng, S. Rohani, Z. Qin, B. Zhao, C.C. Xu, S. Ren, Q. Liu, B. Liang, CO2 mineral carbonation using industrial solid wastes: A review of recent developments, Chemical Engineering Journal 416 (2021) 129093. https://doi.org/10.1016/J.CEJ.2021.129093.

[3] D. Wang, J. Xiao, Z. Duan, Strategies to accelerate CO2 sequestration of cement-based materials and their application prospects, Constr Build Mater 314 (2022) 125646. https://doi.org/10.1016/j.conbuildmat.2021.125646.

[4] IEA (2024), CO2 Emissions in 2023, IEA, Paris https://www.iea.org/reports/co2-emissions-in-2023, Licence: CC BY 4.0, (n.d.). https://www.iea.org/reports/co2-emissions-in-2023 (accessed November 4, 2024).

[5] North M Styring P., Carbond Dioxide Utilization_Volume 1, 2019.

[6] S. Yadav, A. Mehra, A review on ex situ mineral carbonation, Environmental Science and Pollution Research 28 (2021) 12202–12231. https://doi.org/10.1007/s11356-020-12049-4.

[7] G. Biava, L.E. Depero, E. Bontempi, Accelerated Carbonation of Steel Slag and Their Valorisation in Cement Products: A Review, Spanish Journal of Soil Science 14 (2024). https://doi.org/10.3389/sjss.2024.12908.

[8] Pen-Chi Chiang, Shu-Yuan Pan, Carbon Dioxide Mineralization and Utilization, Springer, 2017.

[9] World Steel Association, https://worldsteel.org/data/steel-data-viewer/, (n.d.). https://worldsteel.org/data/steel-data-viewer/ (accessed November 4, 2024).

[10] A.S. Brand, E.O. Fanijo, A Review of the Influence of Steel Furnace Slag Type on the Properties of Cementitious Composites, Applied Sciences 10 (2020) 8210. https://doi.org/10.3390/app10228210.

[11] L. Li, T.-C. Ling, S.-Y. Pan, Environmental benefit assessment of steel slag utilization and carbonation: A systematic review, Science of The Total Environment 806 (2022) 150280. https://doi.org/10.1016/j.scitotenv.2021.150280.

[12] Federacciai, (n.d.). https://federacciai.it/ (accessed April 12, 2025).

[13] N.L. Ukwattage, P.G. Ranjith, X. Li, Steel-making slag for mineral sequestration of carbon dioxide by accelerated carbonation, Measurement 97 (2017) 15–22. https://doi.org/10.1016/j.measurement.2016.10.057.

[14] R. Chang, S. Kim, S. Lee, S. Choi, M. Kim, Y. Park, Calcium Carbonate Precipitation for CO2 Storage and Utilization: A Review of the Carbonate Crystallization and Polymorphism, Front Energy Res 5 (2017). https://doi.org/10.3389/fenrg.2017.00017.

[15] D.T. Tran, Y. Lee, H.S. Lee, H.-M. Yang, J.K. Singh, Effects of γ-C2S on the Properties of Ground Granulated Blast-Furnace Slag Mortar in Natural and Accelerated Carbonation Curing, Sustainability 13 (2021) 357. https://doi.org/10.3390/su13010357.

[16] Mohammed A.M.A., Sequestration of Carbon Dioxide Using Ground Granulated Blast Furnaces Slag and kaolin mixtures, Global NEST Journal (2021). https://doi.org/10.30955/gnj.003487.

[17] K. Mei, T. Gu, Y. Zheng, L. Zhang, F. Zhao, P. Gong, S. Huang, C. Zhang, X. Cheng, Effectiveness and microstructure change of alkali-activated materials during accelerated carbonation curing, Constr Build Mater 274 (2021) 122063. https://doi.org/10.1016/j.conbuildmat.2020.122063.

[18] A.M.A. Mohammed, N.Z. Mohd Yunus, M.A. Hezmi, A.S. A. Rashid, S. Horpibulsuk, Carbonated ground granulated blast furnace slag stabilising brown kaolin, Environmental Science and Pollution Research 28 (2021) 57308–57320. https://doi.org/10.1007/s11356-021-14718-4.

[19] A. Younsi, Long-term carbon dioxide sequestration by concretes with supplementary cementitious materials under indoor and outdoor exposure: Assessment as per a standardized model, Journal of Building Engineering 51 (2022) 104306. https://doi.org/10.1016/j.jobe.2022.104306.

[20] H. Li, S. Zhang, K. Wang, X. Zhang, Y. Jiang, Effect of CO2 capture on the performance of CaO-activated slag pastes and their acid resistance, Constr Build Mater 365 (2023) 130039. https://doi.org/10.1016/j.conbuildmat.2022.130039.

[21] Y. Luo, D. He, Research status and future challenge for CO2 sequestration by mineral carbonation strategy using iron and steel slag, Environmental Science and Pollution Research 28 (2021) 49383–49409. https://doi.org/10.1007/s11356-021-15254-x.

[22] Y. Zhang, L. Yu, K. Cui, H. Wang, T. Fu, Carbon capture and storage technology by steel-making slags: Recent progress and future challenges, Chemical Engineering Journal 455 (2023) 140552. https://doi.org/10.1016/j.cej.2022.140552.

[23] R. Ragipani, S. Bhattacharya, A.K. Suresh, A review on steel slag valorisation via mineral carbonation, React Chem Eng 6 (2021) 1152–1178. https://doi.org/10.1039/D1RE00035G.

[24] R. Ragipani, S. Bhattacharya, S.K. Akkihebbal, Understanding dissolution characteristics of steel slag for resource recovery, Waste Management 117 (2020) 179–187. https://doi.org/10.1016/j.wasman.2020.08.008.

[25] D. Wang, J. Chang, W.S. Ansari, The effects of carbonation and hydration on the mineralogy and microstructure of basic oxygen furnace slag products, Journal of CO2 Utilization 34 (2019) 87–98. https://doi.org/10.1016/j.jcou.2019.06.001.

[26] S. Yadav, A. Mehra, Dissolution of steel slags in aqueous media, Environmental Science and Pollution Research 24 (2017) 16305–16315. https://doi.org/10.1007/s11356-017-9036-z.

[27] S. Yadav, A. Mehra, Experimental study of dissolution of minerals and CO2 sequestration in steel slag, Waste Management 64 (2017) 348–357. https://doi.org/10.1016/j.wasman.2017.03.032.

[28] M. Quaghebeur, P. Nielsen, L. Horckmans, D. Van Mechelen, Accelerated Carbonation of Steel Slag Compacts: Development of High-Strength Construction Materials, Front Energy Res 3 (2015). https://doi.org/10.3389/fenrg.2015.00052.

[29] L. Li, Y. Jiang, S.-Y. Pan, T.-C. Ling, Comparative life cycle assessment to maximize CO2 sequestration of steel slag products, Constr Build Mater 298 (2021) 123876. https://doi.org/10.1016/j.conbuildmat.2021.123876.

[30] Y. Luo, D. He, Research status and future challenge for CO2 sequestration by mineral carbonation strategy using iron and steel slag, Environmental Science and Pollution Research 28 (2021) 49383–49409. https://doi.org/10.1007/s11356-021-15254-x.

[31] Y.-J. Wang, M.-J. Tao, J.-G. Li, Y.-N. Zeng, S. Qin, S.-H. Liu, Carbonation of EAF Stainless Steel Slag and Its Effect on Chromium Leaching Characteristics, Crystals (Basel) 11 (2021) 1498. https://doi.org/10.3390/cryst11121498.

[32] T.-L. Chen, Y.-X. Xiong, Y.-H. Chen, P.-C. Chiang, Y.-H. Chen, Performance evaluation and process simulation for synergetic removal of NOx, CO2 and PM using green alkaline solution in a high-gravity rotating packed bed, Fuel 280 (2020) 118643. https://doi.org/10.1016/j.fuel.2020.118643.

[33] Z. Tong, G. Ma, D. Zhou, G. Yang, C. Peng, The Indirect Mineral Carbonation of Electric Arc Furnace Slag Under Microwave Irradiation, Sci Rep 9 (2019) 7676. https://doi.org/10.1038/s41598-019-44162-x.

[34] N. Zod, A. Mucci, O. Bahn, R. Provençal, Y. Shao, Steel slag-bonded strand board as a carbon-negative building product, Constr Build Mater 340 (2022) 127695. https://doi.org/10.1016/j.conbuildmat.2022.127695.

[35] B. Xu, Y. Yi, Treatment of ladle furnace slag by carbonation: Carbon dioxide sequestration, heavy metal immobilization, and strength enhancement, Chemosphere 287 (2022) 132274. https://doi.org/10.1016/j.chemosphere.2021.132274.

[36] S. Zhang, Z. Ghouleh, J. Liu, Y. Shao, Converting ladle slag into high-strength cementing material by flue gas carbonation at different temperatures, Resour Conserv Recycl 174 (2021) 105819. https://doi.org/10.1016/j.resconrec.2021.105819.

[37] P.K. Araizi, C.D. Hills, A. Maries, P.J. Gunning, D.S. Wray, Enhancement of accelerated carbonation of alkaline waste residues by ultrasound, Waste Management 50 (2016) 121–129. https://doi.org/10.1016/j.wasman.2016.01.006.

[38] E.-J. Moon, Y.C. Choi, Carbon dioxide fixation via accelerated carbonation of cement-based materials: Potential for construction materials applications, Constr Build Mater 199 (2019) 676–687. https://doi.org/10.1016/j.conbuildmat.2018.12.078.

[39] B. Park, E.-J. Moon, Y.C. Choi, Investigation of microstructure and mechanical performance of carbon-capture binder using AOD stainless steel slag, Constr Build Mater 242 (2020) 118174. https://doi.org/10.1016/j.conbuildmat.2020.118174.

[40] E.-J. Moon, Y.C. Choi, Development of carbon-capture binder using stainless steel argon oxygen decarburization slag activated by carbonation, J Clean Prod 180 (2018) 642–654. https://doi.org/10.1016/j.jclepro.2018.01.189.

[41] X. Mei, Q. Zhao, Y. Min, C. Liu, H. Saxén, R. Zevenhoven, Phase transition and dissolution behavior of Ca/Mg-bearing silicates of steel slag in acidic solutions for integration with carbon sequestration, Process Safety and Environmental Protection 159 (2022) 221–231. https://doi.org/10.1016/j.psep.2021.12.062.

[42] R. Baciocchi, G. Costa, M. Di Gianfilippo, A. Polettini, R. Pomi, A. Stramazzo, Thin-film versus slurry-phase carbonation of steel slag: CO2 uptake and effects on mineralogy, J Hazard Mater 283 (2015) 302–313. https://doi.org/10.1016/J.JHAZMAT.2014.09.016.

[43] R. Baciocchi, G. Costa, A. Polettini, R. Pomi, Effects of thin-film accelerated carbonation on steel slag leaching, J Hazard Mater 286 (2015) 369–378. https://doi.org/10.1016/j.jhazmat.2014.12.059.

[44] A. Polettini, R. Pomi, A. Stramazzo, CO2 sequestration through aqueous accelerated carbonation of BOF slag: A factorial study of parameters effects, J Environ Manage 167 (2016) 185–195. https://doi.org/10.1016/j.jenvman.2015.11.042.

[45] K.S. Lackner, C.H. Wendt, D.P. Butt, E.L. Joyce, D.H. Sharp, Carbon dioxide disposal in carbonate minerals, Energy 20 (1995) 1153–1170. https://doi.org/10.1016/0360-5442(95)00071-N.

[46] Z. Chen, Z. Cang, F. Yang, J. Zhang, L. Zhang, Carbonation of steelmaking slag presents an opportunity for carbon neutral: A review, Journal of CO2 Utilization 54 (2021) 101738. https://doi.org/10.1016/j.jcou.2021.101738.

[47] T.D. Rushendra Revathy, K. Palanivelu, A. Ramachandran, Direct mineral carbonation of steelmaking slag for CO2 sequestration at room temperature, Environmental Science and Pollution Research 23 (2016) 7349–7359. https://doi.org/10.1007/s11356-015-5893-5.

[48] F.W.K. Khudhur, J.M. MacDonald, A. Macente, L. Daly, The utilization of alkaline wastes in passive carbon capture and sequestration: Promises, challenges and environmental aspects, Science of The Total Environment 823 (2022) 153553. https://doi.org/10.1016/j.scitotenv.2022.153553.

[49] X. Huang, J. Zhang, L. Zhang, Accelerated carbonation of steel slag: A review of methods, mechanisms and influencing factors, Constr Build Mater 411 (2024) 134603. https://doi.org/10.1016/j.conbuildmat.2023.134603.

[50] J. Wang, M. Zhong, P. Wu, S. Wen, L. Huang, P. Ning, A Review of the Application of Steel Slag in CO2 Fixation, ChemBioEng Reviews 8 (2021) 189–199. https://doi.org/10.1002/cben.202000021.

[51] M. Spanka, T. Mansfeldt, R. Bialucha, Influence of Natural and Accelerated Carbonation of Steel Slags on Their Leaching Behavior, Steel Res Int 87 (2016) 798–810. https://doi.org/10.1002/srin.201500370.

[52] M.-S. Kim, S.-R. Sim, D.-W. Ryu, Supercritical CO2 Curing of Resource-Recycling Secondary Cement Products Containing Concrete Sludge Waste as Main Materials, Materials 15 (2022) 4581. https://doi.org/10.3390/ma15134581.

[53] S.-Y. Pan, Y.-H. Chen, L.-S. Fan, H. Kim, X. Gao, T.-C. Ling, P.-C. Chiang, S.-L. Pei, G. Gu, CO2 mineralization and utilization by alkaline solid wastes for potential carbon reduction, Nat Sustain 3 (2020) 399–405. https://doi.org/10.1038/s41893-020-0486-9.

[54] L. Chen, H. Wang, K. Zheng, J. Zhou, F. He, Q. Yuan, The mechanism of basic oxygen furnace steel slag retarding early-age hydration of Portland cement and mitigating approach towards higher utilization rate, J Clean Prod 362 (2022) 132493. https://doi.org/10.1016/J.JCLEPRO.2022.132493.

[55] S. Kim, J. Kim, D. Jeon, J. Yang, J. Moon, Enhanced mechanical property of steel slag through glycine-assisted hydration and carbonation curing, Cem Concr Compos 149 (2024) 105532. https://doi.org/10.1016/J.CEMCONCOMP.2024.105532.

[56] R. Hu, J. Xie, S. Wu, C. Yang, D. Yang, Study of Toxicity Assessment of Heavy Metals from Steel Slag and Its Asphalt Mixture, Materials 13 (2020) 2768. https://doi.org/10.3390/ma13122768.

[57] Q. Song, M.-Z. Guo, L. Wang, T.-C. Ling, Use of steel slag as sustainable construction materials: A review of accelerated carbonation treatment, Resour Conserv Recycl 173 (2021) 105740. https://doi.org/10.1016/j.resconrec.2021.105740.

[58] Y. Fang, J. Shan, Q. Wang, M. Zhao, X. Sun, Semi-dry and aqueous carbonation of steel slag: Characteristics and properties of steel slag as supplementary cementitious materials, Constr Build Mater 425 (2024) 135981. https://doi.org/10.1016/J.CONBUILDMAT.2024.135981.

[59] M. Zajac, I. Maruyama, A. Iizuka, J. Skibsted, Enforced carbonation of cementitious materials, Cem Concr Res 174 (2023) 107285. https://doi.org/10.1016/j.cemconres.2023.107285.

[60] M. Cisiński, G. Biava, F. Winnefeld, Ł. Sadowski, M. Ben Haha, M. Zajac, Carbonated calcium silicates as pozzolanic supplementary cementitious materials, Constr Build Mater 443 (2024) 137764. https://doi.org/10.1016/J.CONBUILDMAT.2024.137764.

[61] M. Zajac, J. Song, P. Ullrich, J. Skocek, M. Ben Haha, J. Skibsted, High early pozzolanic reactivity of alumina-silica gel: A study of the hydration of composite cements with carbonated recycled concrete paste, Cem Concr Res 175 (2024) 107345. https://doi.org/10.1016/J.CEMCONRES.2023.107345.

[62] P. Liu, J. Zhong, M. Zhang, L. Mo, M. Deng, Effect of CO2 treatment on the microstructure and properties of steel slag supplementary cementitous materials, Constr Build Mater 309 (2021) 125171. https://doi.org/10.1016/j.conbuildmat.2021.125171.

[63] K.-W. Chen, S.-Y. Pan, C.-T. Chen, Y.-H. Chen, P.-C. Chiang, High-gravity carbonation of basic oxygen furnace slag for CO2 fixation and utilization in blended cement, J Clean Prod 124 (2016) 350–360. https://doi.org/10.1016/j.jclepro.2016.02.072.

[64] Y. Wang, M. Tao, J. Li, J. Zhang, S. Qin, S. Liu, L. Peng, X. Zhang, X. Zhang, Y. Zeng, A review of use of metallurgical slag for its carbonation products: processes, crystallization behavior, and application status, Journal of Iron and Steel Research International 30 (2023) 2341–2365. https://doi.org/10.1007/s42243-023-01108-y.

[65] M. Zajac, J. Skibsted, J. Skocek, P. Durdzinski, F. Bullerjahn, M. Ben Haha, Phase assemblage and microstructure of cement paste subjected to enforced, wet carbonation, Cem Concr Res 130 (2020) 105990. https://doi.org/10.1016/j.cemconres.2020.105990.

[66] G. Biava, A. Zacco, A. Zanoletti, G.P. Sorrentino, C. Capone, A. Principallo, L.E. Depero, E. Bontempi, Accelerated Direct Carbonation of Steel Slag and Cement Kiln Dust: An Industrial Symbiosis Strategy Applied in the Bergamo–Brescia Area, Materials 16 (2023) 4055. https://doi.org/10.3390/ma16114055.

[67] G. Villain, M. Thiery, G. Platret, Measurement methods of carbonation profiles in concrete: Thermogravimetry, chemical analysis and gammadensimetry, Cem Concr Res 37 (2007) 1182–1192. https://doi.org/10.1016/J.CEMCONRES.2007.04.015.

[68] C.C. Turvey, S.A. Wilson, J.L. Hamilton, G. Southam, Field-based accounting of CO_2 sequestration in ultramafic mine wastes using portable X-ray diffraction, American Mineralogist 102 (2017) 1302–1310. https://doi.org/10.2138/am-2017-5953.

[69] N.T. Abdel-Ghani, H.A. El-Sayed, A.A. El-Habak, Utilization of by-pass cement kiln dust and air-cooled blast-furnace steel slag in the production of some “green” cement products, HBRC Journal 14 (2018) 408–414. https://doi.org/10.1016/j.hbrcj.2017.11.001.

[70] D. Sharma, S. Goyal, Accelerated carbonation curing of cement mortars containing cement kiln dust: An effective way of CO2 sequestration and carbon footprint reduction, J Clean Prod 192 (2018) 844–854. https://doi.org/10.1016/j.jclepro.2018.05.027.

[71] Y. Jiang, T.-C. Ling, C. Shi, S.-Y. Pan, Characteristics of steel slags and their use in cement and concrete—A review, Resour Conserv Recycl 136 (2018) 187–197. https://doi.org/10.1016/j.resconrec.2018.04.023.

[72] A. Polettini, R. Pomi, A. Stramazzo, Carbon sequestration through accelerated carbonation of BOF slag: Influence of particle size characteristics, Chemical Engineering Journal 298 (2016) 26–35. https://doi.org/10.1016/j.cej.2016.04.015.

[73] P. Das, S. Upadhyay, S. Dubey, K.K. Singh, Waste to wealth: Recovery of value-added products from steel slag, J Environ Chem Eng 9 (2021) 105640. https://doi.org/10.1016/j.jece.2021.105640.

[74] D. Satish Kumar, R. Sah, S. Sanyal, G. Prasad, Measurement of metallic iron in steel making slags, Measurement 131 (2019) 156–161. https://doi.org/10.1016/J.MEASUREMENT.2018.08.066.

[75] H. Alanyali, M. Çöl, M. Yilmaz, Ş. Karagöz, Application of magnetic separation to steelmaking slags for reclamation, Waste Management 26 (2006) 1133–1139. https://doi.org/10.1016/J.WASMAN.2006.01.017.

[76] Y. pei Lan, Q. cai Liu, F. Meng, D. liang Niu, H. Zhao, Optimization of magnetic separation process for iron recovery from steel slag, Journal of Iron and Steel Research, International 24 (2017) 165–170. https://doi.org/10.1016/S1006-706X(17)30023-7.

[77] N. Doebelin, R. Kleeberg, Profex: a graphical user interface for the Rietveld refinement program BGMN, J Appl Crystallogr 48 (2015) 1573–1580. https://doi.org/10.1107/S1600576715014685.

[78] A. Assi, S. Federici, F. Bilo, A. Zacco, L.E. Depero, E. Bontempi, Increased Sustainability of Carbon Dioxide Mineral Sequestration by a Technology Involving Fly Ash Stabilization, Materials 12 (2019) 2714. https://doi.org/10.3390/ma12172714.

[79] Profex, (n.d.). http://www.bgmn.de/variables.html#B1 (accessed April 25, 2025).

[80] D. Jansen, F. Goetz-Neunhoeffer, C. Stabler, J. Neubauer, A remastered external standard method applied to the quantification of early OPC hydration, Cem Concr Res 41 (2011) 602–608. https://doi.org/10.1016/j.cemconres.2011.03.004.

[81] B.H. O'Connor, M.D. Raven, Application of the Rietveld Refinement Procedure in Assaying Powdered Mixtures, Powder Diffr 3 (1988) 2–6. https://doi.org/10.1017/S0885715600013026.

[82] NIST, (n.d.). https://physics.nist.gov/PhysRefData/XrayMassCoef/tab3.html (accessed March 15, 2025).

[83] D.N. Huntzinger, J.S. Gierke, S.K. Kawatra, T.C. Eisele, L.L. Sutter, Carbon Dioxide Sequestration in Cement Kiln Dust through Mineral Carbonation, Environ Sci Technol 43 (2009) 1986–1992. https://doi.org/10.1021/es802910z.

[84] D.N. Huntzinger, J.S. Gierke, L.L. Sutter, S.K. Kawatra, T.C. Eisele, Mineral carbonation for carbon sequestration in cement kiln dust from waste piles, J Hazard Mater 168 (2009) 31–37. https://doi.org/10.1016/j.jhazmat.2009.01.122.

[85] Federacciai, La valorizzazione degli aggregati di origine siderurgica, 2012.

[86] H. Alanyalı, M. Çöl, M. Yılmaz, Ş. Karagöz, Application of magnetic separation to steelmaking slags for reclamation, Waste Management 26 (2006) 1133–1139. https://doi.org/10.1016/j.wasman.2006.01.017.

[87] M. Abdelzaher, A. Hamouda, I. El-Kattan, A. Baher, Laboratory Study for Accelerating the CKD Mineral Carbonation, Egypt J Chem 0 (2021) 0–0. https://doi.org/10.21608/ejchem.2021.93980.4425.

[88] L.B. Capeletti, J.H. Zimnoch, Fourier Transform Infrared and Raman Characterization of Silica-Based Materials, in: Applications of Molecular Spectroscopy to Current Research in the Chemical and Biological Sciences, InTech, 2016. https://doi.org/10.5772/64477.

[89] R. Baciocchi, G. Costa, A. Polettini, R. Pomi, Influence of particle size on the carbonation of stainless steel slag for CO2 storage, Energy Procedia 1 (2009) 4859–4866. https://doi.org/https://doi.org/10.1016/j.egypro.2009.02.314.

[90] B. Xu, Y. Yi, Soft clay stabilization using ladle slag-ground granulated blastfurnace slag blend, Appl Clay Sci 178 (2019) 105136. https://doi.org/10.1016/J.CLAY.2019.105136.

[91] J.-H. Jang, B.A. Dempsey, W.D. Burgos, Solubility of Hematite Revisited: Effects of Hydration, Environ Sci Technol 41 (2007) 7303–7308. https://doi.org/10.1021/es070535t.

[92] R. Baciocchi, G. Costa, D. Zingaretti, M. Cazzotti, M. Werner, A. Polettini, R. Pomi, M. Falasca, Studio sulle potenzialità della carbonatazione di minerali e residui industriali per lo stoccaggio di anidride carbonica prodotta da impianti di piccola/media taglia, 2010.

[93] M. Bodor, R.M. Santos, L. Kriskova, J. Elsen, M. Vlad, T. Van Gerven, Susceptibility of mineral phases of steel slags towards carbonation: mineralogical, morphological and chemical assessment, European Journal of Mineralogy 25 (2013) 533–549. https://doi.org/10.1127/0935-1221/2013/0025-2300.

[94] G.B. Alexander, W.M. Heston, R.K. Iler, The Solubility of Amorphous Silica in Water, J Phys Chem 58 (1954) 453–455. https://doi.org/10.1021/j150516a002.

[95] P. Yu, R.J. Kirkpatrick, B. Poe, P.F. McMillan, X. Cong, Structure of Calcium Silicate Hydrate (C-S-H): Near-, Mid-, and Far-Infrared Spectroscopy, Journal of the American Ceramic Society 82 (2004) 742–748. https://doi.org/10.1111/j.1151-2916.1999.tb01826.x.

[96] D. Medas, G. Cappai, G. De Giudici, M. Piredda, S. Podda, Accelerated carbonation by cement kiln dust in aqueous slurries: chemical and mineralogical investigation, Greenhouse Gases: Science and Technology 7 (2017) 692–705. https://doi.org/10.1002/ghg.1681.

[97] X. Wang, X. Lu, C.C. Turvey, G.M. Dipple, W. Ni, Evaluation of the carbon sequestration potential of steel slag in China based on theoretical and experimental labile Ca, Resour Conserv Recycl 186 (2022) 106590. https://doi.org/10.1016/j.resconrec.2022.106590.

[98] D. Bonenfant, L. Kharoune, S. Sauve´, R. Hausler, P. Niquette, M. Mimeault, M. Kharoune, CO2 Sequestration Potential of Steel Slags at Ambient Pressure and Temperature, Ind Eng Chem Res 47 (2008) 7610–7616. https://doi.org/10.1021/ie701721j.

[99] P.J. Gunning, C.D. Hills, P.J. Carey, Accelerated carbonation treatment of industrial wastes, Waste Management 30 (2010) 1081–1090. https://doi.org/10.1016/j.wasman.2010.01.005.

[100] J.I. Pedraza, L.A. Suarez, L.A. Martinez, N.Y. Rojas, J.I. Tobon, J.H. Ramirez, H.R. Zea, A.A. Caceres, Carbon capture and utilization by mineral carbonation with CKD in aqueous phase: Experimental stage and characterization of carbonated products, in: Proceedings of the 7th International Workshop, Advances in Cleaner Production, Academic Work, Barranquilla, Colombia, 2018: pp. 21–22.

[101] Z. Pan, L. Chen, C. Cao, F. Zhang, H. Zhang, Y. Guo, Optimizing carbonation reaction parameters of calcium carbide slag in acidic/alkaline environment enhancing CO2 mineralization efficiency, Chemical Engineering Journal 498 (2024) 155587. https://doi.org/10.1016/J.CEJ.2024.155587.

[102] Z. Wang, L. Cui, Y. Liu, J. Hou, H. Li, L. Zou, F. Zhu, High-efficiency CO2 sequestration through direct aqueous carbonation of carbide slag: determination of carbonation reaction and optimization of operation parameters, Front Environ Sci Eng 18 (2024) 12. https://doi.org/10.1007/s11783-024-1772-y.

[103] S. Srivastava, M. Cerutti, H. Nguyen, V. Carvelli, P. Kinnunen, M. Illikainen, Carbonated steel slags as supplementary cementitious materials: Reaction kinetics and phase evolution, Cem Concr Compos 142 (2023) 105213. https://doi.org/10.1016/j.cemconcomp.2023.105213.

[104] M. Zajac, J. Skocek, Ł. Gołek, J. Deja, Supplementary cementitious materials based on recycled concrete paste, J Clean Prod 387 (2023) 135743. https://doi.org/10.1016/j.jclepro.2022.135743.

[105] D. Wang, J. Chang, W.S. Ansari, The effects of carbonation and hydration on the mineralogy and microstructure of basic oxygen furnace slag products, Journal of CO2 Utilization 34 (2019) 87–98. https://doi.org/10.1016/j.jcou.2019.06.001.

[106] H. Wang, X. Gu, J. Liu, Z. Zhu, S. Wang, X. Xu, M.L. Nehdi, Synergistic effects of steel slag and lithium slag in carbonation-cured cement pastes: Carbonation degree, strength and

microstructure, Journal of Building Engineering 85 (2024) 108706. https://doi.org/10.1016/J.JOBE.2024.108706.

[107] Y. Göçtü, Y. Tufan, B. Ercan, Synthesis, characterization, and biological properties of calcium and zinc based ion incorporated amorphous carbonate nanoparticles, Ceram Int 51 (2025) 43–53. https://doi.org/10.1016/J.CERAMINT.2024.10.292.

[108] T.Q. Tran, R. Cook, O. Ipindola, E.O. Fanijo, A. Newman, P.E. Stutzman, A.S. Brand, Measuring mineralized carbon in carbonate minerals and cementitious materials by an acid digestion-titration method, Cem Concr Res 191 (2025) 107829. https://doi.org/10.1016/J.CEMCONRES.2025.107829.

[109] P. Liu, M. Zhang, L. Mo, J. Zhong, M. Xu, M. Deng, Probe into carbonation mechanism of steel slag via FIB-TEM: The roles of various mineral phases, Cem Concr Res 162 (2022) 106991. https://doi.org/10.1016/j.cemconres.2022.106991.

[110] Z. Liu, P. Van den Heede, C. Zhang, X. Shi, L. Wang, J. Li, Y. Yao, B. Lothenbach, N. De Belie, Carbonation of blast furnace slag concrete at different CO2 concentrations: Carbonation rate, phase assemblage, microstructure and thermodynamic modelling, Cem Concr Res 169 (2023) 107161. https://doi.org/10.1016/j.cemconres.2023.107161.

[111] L. Zhang, J. Cui, Z. Chen, X. Jing, Y. Liu, B. He, D. Cang, Recycling of carbonated steel slag in building materials: Recycling pathways and recent advances, Journal of Building Engineering 104 (2025) 112285. https://doi.org/10.1016/J.JOBE.2025.112285.

[112] M. Salman, Ö. Cizer, Y. Pontikes, R.M. Santos, R. Snellings, L. Vandewalle, B. Blanpain, K. Van Balen, Effect of accelerated carbonation on AOD stainless steel slag for its valorisation as a CO2-sequestering construction material, Chemical Engineering Journal 246 (2014) 39–52. https://doi.org/10.1016/j.cej.2014.02.051.

[113] L. Kriskova, Y. Pontikes, Ö. Cizer, G. Mertens, W. Veulemans, D. Geysen, P.T. Jones, L. Vandewalle, K. Van Balen, B. Blanpain, Effect of mechanical activation on the hydraulic properties of stainless steel slags, Cem Concr Res 42 (2012) 778–788. https://doi.org/10.1016/j.cemconres.2012.02.016.

[114] S. Yasipourtehrani, V. Strezov, S. Bliznyukov, T. Evans, Investigation of thermal properties of blast furnace slag to improve process energy efficiency, J Clean Prod 149 (2017) 137–145. https://doi.org/10.1016/j.jclepro.2017.02.052.

[115] K.L. Scrivener, P. Juilland, P.J.M. Monteiro, Advances in understanding hydration of Portland cement, Cem Concr Res 78 (2015) 38–56. https://doi.org/10.1016/J.CEMCONRES.2015.05.025.

[116] P. Liu, L. Mo, Z. Zhang, Effects of carbonation degree on the hydration reactivity of steel slag in cement-based materials, Constr Build Mater 370 (2023) 130653. https://doi.org/10.1016/j.conbuildmat.2023.130653.

[117] X. Huang, J. Zhang, L. Zhang, Accelerated carbonation of steel slag: A review of methods, mechanisms and influencing factors, Constr Build Mater 411 (2024) 134603. https://doi.org/10.1016/J.CONBUILDMAT.2023.134603.

[118] M. Zajac, J. Skocek, P. Durdzinski, F. Bullerjahn, J. Skibsted, M. Ben Haha, Effect of carbonated cement paste on composite cement hydration and performance, Cem Concr Res 134 (2020) 106090. https://doi.org/10.1016/j.cemconres.2020.106090.

[119] M. Zajac, J. Song, P. Ullrich, J. Skocek, M. Ben Haha, J. Skibsted, High early pozzolanic reactivity of alumina-silica gel: A study of the hydration of composite cements with carbonated recycled concrete paste, Cem Concr Res 175 (2024) 107345. https://doi.org/10.1016/j.cemconres.2023.107345.

[120] S.K. Singh, Jyoti, P. Vashistha, Development of newer composite cement through mechano-chemical activation of steel slag, Constr Build Mater 268 (2021) 121147. https://doi.org/10.1016/J.CONBUILDMAT.2020.121147.

[121] X. Wang, W. Ni, J. Li, S. Zhang, K. Li, Study on Mineral Compositions of Direct Carbonated Steel Slag by QXRD, TG, FTIR, and XPS, Energies (Basel) 14 (2021) 4489. https://doi.org/10.3390/en14154489.

[122] H. Na, Y. Wang, X. Zhang, J. Li, Y. Zeng, P. Liu, Hydration Activity and Carbonation Characteristics of Dicalcium Silicate in Steel Slag: A Review, Metals (Basel) 11 (2021) 1580. https://doi.org/10.3390/met11101580.

[123] B. Lothenbach, K. Scrivener, R.D. Hooton, Supplementary cementitious materials, Cem Concr Res 41 (2011) 1244–1256. https://doi.org/10.1016/J.CEMCONRES.2010.12.001.

[124] B. Lothenbach, G. Le Saout, E. Gallucci, K. Scrivener, Influence of limestone on the hydration of Portland cements, Cem Concr Res 38 (2008) 848–860. https://doi.org/10.1016/j.cemconres.2008.01.002.

[125] T. Matschei, B. Lothenbach, F.P. Glasser, The role of calcium carbonate in cement hydration, Cem Concr Res 37 (2007) 551–558. https://doi.org/10.1016/j.cemconres.2006.10.013.

[126] F. Georget, B. Lothenbach, W. Wilson, F. Zunino, K.L. Scrivener, Stability of hemicarbonate under cement paste-like conditions, Cem Concr Res 153 (2022) 106692. https://doi.org/10.1016/J.CEMCONRES.2021.106692.

[127] T. Matschei, B. Lothenbach, F.P. Glasser, The role of calcium carbonate in cement hydration, Cem Concr Res 37 (2007) 551–558. https://doi.org/10.1016/J.CEMCONRES.2006.10.013.

[128] D. He, L. Yang, J. Guo, Effect of Carbonation Degree on Mineral Composition, Microstructure, and Cementitious Properties of BOF Slag, Journal of Sustainable Metallurgy 10 (2024) 2267–2281. https://doi.org/10.1007/s40831-024-00881-8.

[129] Y. Fang, J. Shan, Q. Wang, M. Zhao, X. Sun, Semi-dry and aqueous carbonation of steel slag: Characteristics and properties of steel slag as supplementary cementitious materials, Constr Build Mater 425 (2024) 135981. https://doi.org/10.1016/J.CONBUILDMAT.2024.135981.

RINGRAZIAMENTI

Ringrazio il gruppo Chem4tech per avermi accolto, aiutato in questo percorso sia a livello professionale che umano. Ringrazio i miei colleghi dottorandi che hanno condiviso con me questa sfida.

Un grazie particolare è rivolto ad Italcementi per aver creduto in questo progetto, per il loro sostengo sia economico sia lavorativo avendo messo a disposizione spazi, strumenti e collaboratori. Grazie a Claudia e Antonio, i miei tutor aziendali, per aver mostrato interesse nella ricerca e disponibilità nel confronto, grazie a Richi, Faco, Melo, Fede, Scapati, Giorgio, Mattia, Francesco, Chiara e Nicoletta per avermi aiutato nella parte sperimentale del progetto.

Un grazie anche a Heidelberg Materials, Germania, per avermi ospitato nella loro struttura e avermi dato la possibilità di migliorarmi come ricercatore e di usare la strumentazione. Un grazie speciale è rivolto a Maciej per essere stato un mentore e per aver condiviso con me le sue conoscenze sul cemento e la sua reattività. Grazie a Mohsen per la sua ospitalità e guida. Grazie a Martina ed Aysha perché mi hanno fatto sentire a casa nonostante i 600 km di distanza, e ad Hania per essere stata un'ottima collega di ufficio.

Un grazie è doveroso anche per le acciaierie che hanno creduto nel progetto e hanno fornito il materiale senza il quale sarebbe stato impossibile svolgere il dottorato.

Questo traguardo lo dedico a me stessa perché sono stati 3 anni di alti e bassi di un percorso impegnativo. Nonostante le difficoltà che fanno parte del percorso di crescita, ho affrontato ogni problema con la giusta maturità e ho raggiunto questo traguardo straordinario aggiungendo nuove esperienze e abilità nel mio bagaglio personale.

Un grazie va alla mia famiglia che mi ha sempre supportato e sopportato nelle mie scelte lavorative e di vita. Abbiamo sempre affrontato le difficoltà insieme e questo ci ha reso più forti che mai.

Grazie alle mie amiche, "le Cobratz", Laura, Ele, Lucre, Marti e Silvia, e grazie a Michela per esserci sempre state e aver condiviso momenti indimenticabili.

Ultimo ma non per importanza, un grazie a Lorenzo che è stata la mia spalla e il mio pilastro.